energies

Article

Numerical Investigation of the Geometrical Effect on Flow-Induced Vibration Performance of Pivoted Bodies

Hamid Arionfard [1,*] and Sina Mohammadi [2]

[1] Centre for Industrial Mechanics, Southern Denmark University, 6400 Sonderborg, Denmark
[2] Schmid College of Science and Technology, Chapman University, Orange, CA 92866, USA; smohammadi@chapman.edu
* Correspondence: arionfard@sdu.dk; Tel.: +45-655-08287

Abstract: In this study, the Flow-Induced Vibration (FIV) of pivoted cylinders (at a distance) is numerically investigated as a potential source of energy harvesting. In particular, we investigate the effect of pivot point placement, arm length, and natural frequency on the FIV performance of six different cross sections in the Reynolds number of around 1000. All sections have similar mass, area, and moment of inertia to eliminate non-geometrical effects on the performance. Classical studies show that the synchronization phenomenon (lock-in) occurs when the vortex formation frequency is close enough to the body's natural frequency. Due to the configuration of the cylinder in this research (pivoted eccentrically), the natural frequency is also a function of the flow velocity as well as the geometrical specifications of the system. The simulation is done for the arm lengths between −3D and +3D for all cross sections. Results show that maximum output power is principally influenced more by the pivot location than the arm length. Although the box cross section has a higher amplitude of vibration, the circular cross section has the highest efficiency followed by the egg shape.

Keywords: VIV; FIV; renewable energy; pivoted cylinder; cross section; geometry

Citation: Arionfard, H.; Mohammadi, S. Numerical Investigation of the Geometrical Effect on Flow-Induced Vibration Performance of Pivoted Bodies. *Energies* **2021**, *14*, 1128. https://doi.org/10.3390/en14041128

Academic Editor: Adam Adamkowski

Received: 16 January 2021
Accepted: 16 February 2021
Published: 20 February 2021

1. Introduction

In recent years, the development of flow-induced vibrations (FIV) energy harvesters has increased rapidly to offer a new source of energy. Due to the large strains and geometric deformations during FIV, they have traditionally been classified as a destructive phenomenon. One of the well-known examples of flutter-induced destruction is the Tacoma Narrows Bridge collapse in 1940, where torsional flutter at sufficiently large amplitudes caused catastrophic failure of the entire bridge. However, common and accessible FIV could be considered as a way to extract energy. Bernitsas et al. [1] have developed a device that uses the vortex induced vibration (VIV) phenomenon to generate electricity. Contrary to the VIV phenomenon, where significant oscillations develop in a small range of flow velocities and with limited oscillation amplitudes, other aeroelastic instabilities like flutter occur for an infinite range of flow velocities and without a self-limited response beyond the critical flow velocity which makes the flutter more promising for generating energy.

For instance, Hobbs and Hu [2] tested micro-watt energy harvesters inspired by tree trunks swaying in the wind. Their converter consists of four pivoted cylinders which affixed to the ground via a piezoelectric transducer. Yoshitake et al. [3] generated minuscule amounts of energy, using a device composed of Hula-Hoops and an electro magnetic transducer mechanism, in air flow. To study the aerodynamic efficiency of a drag assisted energy-harvesting device, Sung et al. [4] investigated the effects of the cylinder cross-sectional shape on the VIV. Their numerical simulations have demonstrated that an elliptical cylinder undergoes much larger displacements than a circular one. Nevertheless, their research mainly focuses on improving maximum displacement or amplitude rather than the angular velocity of the vibration.

In an attempt to study the performance of FIV, Arionfard and Nishi [5] carried out an experiment on a pivoted cylinder instead of a transitionally moving one. Being assisted by the drag force, the pivoting cylinder showed an increase in performance comparing to transitional VIV of a cylinder. As a result, different configurations with one and two cylinders were considered in the following researches to increase the performance by utilizing different mechanisms of vibrations [6–8]. However, an important way to improve the FIV performance is through the geometry of the bluff body and enhancement of the geometrical parameters is necessary in order to increase energy extraction performance. For several years great effort has been devoted to the study the effect of cross sections on FIV. However, common cross sections in aviation and civil engineering has attracted much more attention; Airfoil flutter [9], galloping of square, triangular, and semicircular sections [10], rectangular and D-sections[11,12] are some examples. However, to the author's best knowledge, very few publications are available in the literature that discuss the role of the geometrical parameters of the bluff body on the performance of the vibration. This paper reports geometrical effects on FIV performance of pivoted cylinders. Six cross section shapes are compared in which the circular cylinder is checked with our experimental data for validating the numerical simulation.

The present paper is organized as follows. The case is described in Section 2 followed by details of the numerical method, domains, and boundary conditions. Verification and validations is reported in Section 4, and the results are presented in in Section 5. We make conclusive remarks in Section 6.

2. Case Description

The cases considered in this study are based on water channel tests performed by Arionfard and Nishi [5]. The channel length is 1 meter with a test section's dimension of 30 cm wide by 30 cm deep. For the numerical simulation, the submerged bluff body is defined as a cylindrical solid sub-domain which is pivoted at a specific distance l, enabling rotation around the Z-axis, where X is the streamwise coordinate and Y is the cross-stream coordinate. The variation of the arm length l is considered by using twelve different values from -3D to +3D, where D is the diameter of the cylinder, negative values of l represent a pivot on the downstream of the cylinder (like Figure 1) and positive values represent a pivot point on the upstream side of the cylinder. A torsional spring is defined at the pivot point shown in Figure 1 and provides a restoring moment during oscillation.

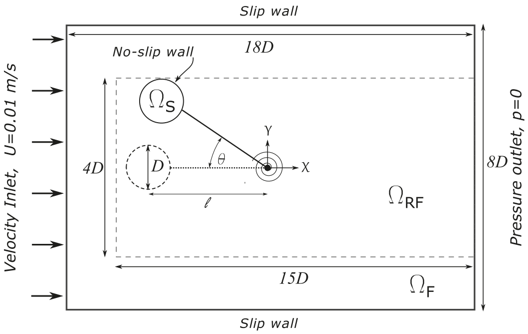

Figure 1. Schematic diagram of a typical computational domain and boundaries. Here, the pivot point is located at the downstream of the cylinder. The solid sub-domain is Ω_S, the fluid sub-domain is Ω_F, and Ω_{RF} is the refined part of the fluid sub-domain. The arm length l is the distance between the center of the bluff body and the pivot point

Six cross section shapes are chosen in this study as solid sub-domains. The area of all cross sections are equal and the height of sections (D) is as similar as possible to keep the

Reynolds number within the same range in all simulations. More details of the geometrical parameters of each cross-section is shown in Figure 2 and described in Table 1.

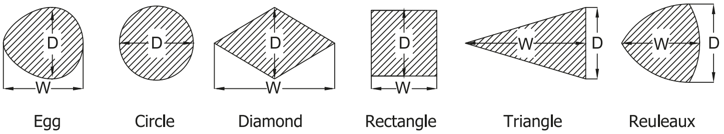

Figure 2. Geometry of the bluff bodies. Dimensions are given in Table 1.

In all simulations, Reynolds number is calculated based on the uniform inlet velocity (0.01 m/s) and the vertical height of the cross section (D ≈ 10 cm).

Table 1. Geometric parameters of the cross sections.

Section	W (cm)	D (cm)	Area (cm^2)	Aspect Ratio	CG (cm)
CIR	10.36	10.36	84.35	1	5.18
BOX	9.18	9.18	84.35	1	4.59
DIA	16.87	10.00	84.35	1.68	8.43
TRI	16.87	10.00	84.35	1.68	11.25
REU	10.94	10.94	84.35	1	6.32
EGG	11.19	10.00	84.35	1.12	5.94

3. Numerical Method

3.1. Governing Equations

The unsteady flow field around the cylinder is numerically simulated by employing 3D Unsteady Reynolds-Averaged Navier–Stokes equations (URANS) in Cartesian coordinates. Although the average Reynolds number in this study is low (≈1000), the local Reynolds number increases in near wall boundaries. Therefore, a turbulent model is necessary to model the behavior of the vortexes on the wake side. There are many turbulence models available and the choice of model depends on many factors such as the physics of the problem, the accuracy required and the computational power available. The K-Omega-SST model is used in this study because it is favored for predicting the formation of the vortices and flow separation [13,14]. By applying Reynolds decomposition and taking the time-average of continuity and momentum equations yields the URANS equations for incompressible flows [15].

The equation of motion for a rigid body in the polar coordinate with linear torsional spring and damper is expressed as

$$I_t\,\ddot{\theta} + C_t\,\dot{\theta} + K\,\theta = M_{hf} \tag{1}$$

where the dot symbol stands for differentiation with respect to time t, I_t is the moment of inertia of the moving cylinder and C_t is the total damping coefficient consist of the structural damping and equivalent generator damping. K represents the torsional stiffness of the spring and θ is the rotational displacement. M_{hf} is the hydrodynamic angular momentum applied on the cylinder about the CG (center of gravity) of the cylinder given by

$$M_{hf} = F_p r_p + F_v r_v \tag{2}$$

where F_p and F_v are normal pressure and tangential viscous contributions. r_p and r_v are corresponding arm lengths from the center of the oscillating body (CG) to the center of rotation defined as

$$\begin{aligned} F_p &= \sum_i \rho_i s_{f,i}(p_i - p_{ref}) \\ F_v &= \sum_i s_{f,i}(\mu R_{DEV}) \end{aligned} \tag{3}$$

where ρ is the density, $s_{f,i}$ the face area vector, p the pressure, μ the dynamic viscosity, and R_{DEV} the deviatoric stress tensor. The hydrodynamic force coefficients are calculated by using the built-in (forcecoeffs) function in OpenFoam given by

$$\begin{aligned} C_l &= \frac{liftForce}{p_{Dyn}} \\ C_d &= \frac{dragForce}{p_{Dyn}} \\ C_m &= \frac{M_{hf}}{p_{Dyn} l} \end{aligned} \tag{4}$$

where $p_{Dyn} = \frac{1}{2}\rho A U^2$, A is the cross section area (84.35 cm^2), l is the arm length, and lift and drag forces are calculated from the vertical and horizontal components of F_p and F_v given by Equation (3). The structural parameters used in this study are described in Table 2 (solid domain).

Equation (1) and URANS equations are strongly coupled with the following steps: First, based on initial and boundary conditions the pressure distribution is calculated. Second, the forces on the cylinder surface corresponding to the pressure are calculated. Third, the equation of motion is solved based on the acquired forces and the displacements are calculated, and finally the domain is re-meshed according to the new position of the cylinder. The algorithm used by solvers is discussed in more details in the following.

Table 2. Initial conditions for solid and fluid domain.

Solid Domain		Fluid Domain	
Angular displacement (Rad)	0.0	Inlet velocity (m/s)	0.01
Angular velocity (Rad/s)	0.0	Outlet pressure (Pa)	0.0
I_t (m^4)	0.056	κ (m^2/s^2)	0.00135
C_t (Nm.s/Rad)	0.1	ω (1/s)	33.4
K (Nm/Rad)	0.1	Max Courant number	1
Mass (Kg)	0.125	Pressure, velocity, κ and ω error tolerances	1×10^{-7}
Cell displacement error tolerance	1×10^{-5}		
Step size (s) 1×10^{-5} *			

* Automatically adjusted during the simulation base on the Courant number.

3.2. CFD Solver

The finite-volume-based open-source computational fluid dynamics library OpenFOAM is used to perform the numerical simulation of the flow field around the cylinder and solving the equation of motion. The governing equations were integrated over each control volume and the discrete values of the relevant quantities were determined at the center of the control volume. The diffusion term in the governing equations is discretized using second order central differencing scheme and for advection term, a second-order upwind scheme is utilized. To obtain a good resolution in time, time integration is performed by a second-order implicit scheme. Due to the unsteady nature of FIV, a PimpleDyMFoam solver is used, which is a transient solver for turbulent incompressible flow on a moving mesh utilizing the PIMPLE (merged PISO-SIMPLE) algorithm. This solver is a modification of the pimpleFoam solver that supports meshes of class dynamicFvMesh. This class is a base class for meshes that can move and/or change topology. The built-in sixDoFRigidBodyMotion solver is utilized in the present study to model the rigid-body motion of the cylinder. One advantage of the sixDoFRigidBodyMotion is that the zone of dynamic mesh can be controlled with input parameters innerDistance and outerDistance, thus it is possible to fix the mesh near the cylinder wall. The fixed mesh moving with the cylinder ensures the large dynamical motion and computational accuracy of the flow near the cylinder wall. Otherwise, the finer mesh near the cylinder is vulnerable to be seriously distorted during the motion of the rigid body if the mesh near the cylinder wall is allowed to deform. Moreover, the fixed zone guarantees the accuracy of the outside boundary condition during the simulation.

3.3. Domain and Boundary Conditions

The mesh generation is performed by using the blockMesh and snappyHexMesh applications within the OpenFOAM package. A base hexahedral mesh is generated using blockMesh as a computational domain and the cylinder is snapped off the base mesh by using snappyHexMesh applications. Then, the remaining mesh is extruded to generate a 3D mesh.

The boundary condition on the cylinder is set to be a moving-wall, with no flux normal to the wall. The inlet boundary is defined as a velocity inlet with a uniform velocity of 0.01 m/s and zero pressure gradient was employed for the outlet. The top and bottom conditions defined as slip boundary while a no-slip condition is applied on the surfaces of the cylinder. The front and back walls are set to empty condition to simplify the simulation.

The initial conditions for the turbulence model were calculated from the inlet velocity and turbulence intensity at the inlet of the actual water channel, which was estimated by using PIV method. A summary of initial conditions is shown in Table 2.

4. Grid Independency and Validation

To reduce the computational cost and prevent mesh dependency, a preliminary study on necessary but sufficient resolution and domain size is done. To determine the domain size, six cases with different lengths and widths are simulated based on the CIR-3D conditions (CIR shape pivoted on the downstream with $l = -3D$). Then, the smallest size at which no further change is seen was selected. Similarly, the resolution of the background mesh (without refinement) is increased until the result did not change with increasing the mesh resolution. The most computationally efficient case is chosen based on the variation of C_l, C_d, and C_m. According to the results of the domain size and resolution study shown in Figures 3 and 4, a refined domain size of 4D by 30D, with a resolution of 7680 elements and total domain size of 8D by 18D is chosen which leads to a blockage ratio of 0.125. Being aware of the limitations of this numerical study, we anticipate that the blockage potentially effects the sections in a similar way allowing comparison based on the difference in motion and hydrodynamic forces. An example of the mesh is shown in Figure 5.

The numerical model used in this study has been validated against our previous experimental results of a pivoted circular cylinder described in [5,6]. In the actual experiment, the cylinder is pivoted at a distance by using a connector arm and the Reynolds number is in the range of $2880 \leq Re \leq 22{,}300$. A force moment sensor is used to measure the forces on the main shaft (at the pivot point) and then the measured forces and moments are used to calculate the hydrodynamic forces on the cylinder after dynamic and static tare. As the hydrodynamic forces are oscillating during the vibration, the corresponding amplitude to the peak frequency in the frequency domain is selected for evaluation after performing a Fast Fourier Transform (FFT). The numerical results are compared to the experiments done in the lowest Reynolds number in the experiment ($Re = 2880$). The numerical results are in good agreement with the experimental data according to Figure 6. Note that the experimental results are more accurate for $Arm\ length \approx 0$ because for the smaller arm lengths the cylinder is more stationary and there is less turbulence induced noise on the cylinder as a result.

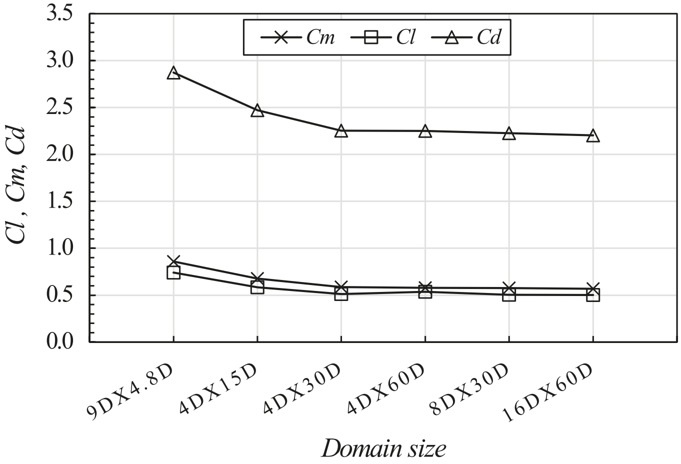

Figure 3. The variation of hydrodynamic coefficients with the domain size.

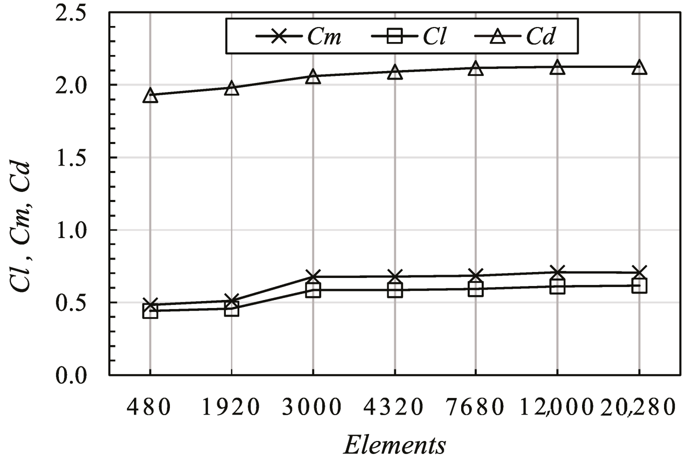

Figure 4. The variation of hydrodynamic coefficients with the mesh size.

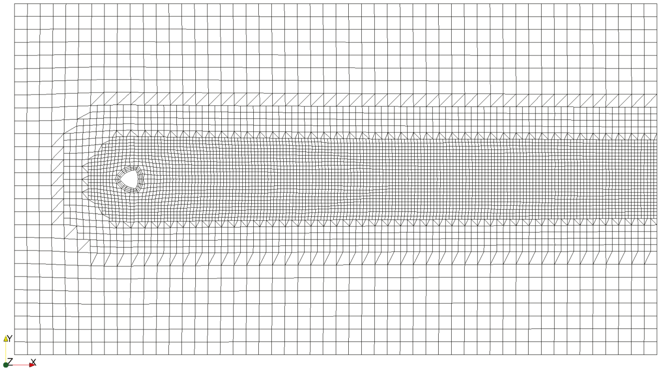

Figure 5. An example of the mesh with reuleaux shape snapped off of the grid.

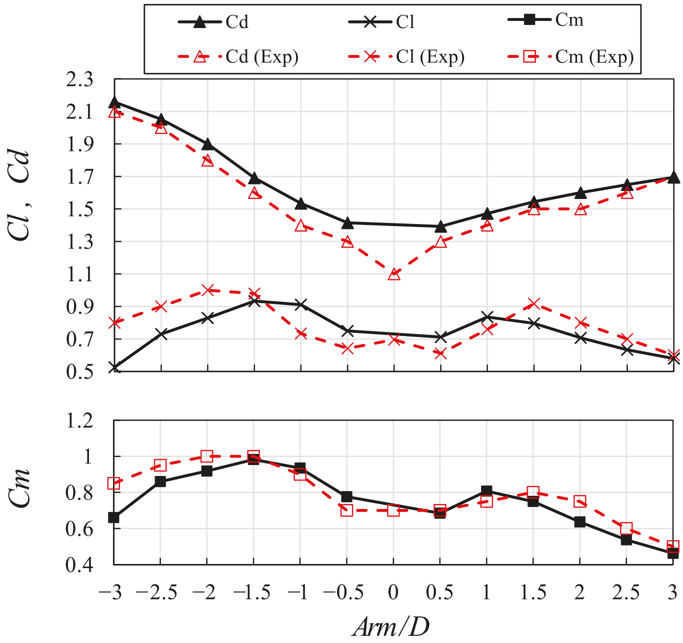

Figure 6. Comparison between the numerical results and experiment.

5. Results and Discussion

For simplicity, a Cartesian coordinate system is used for the discussion of results. The origin is the pivot point, and the X, Y, and Z axes are defined in the streamwise, transverse, and vertical direction, respectively. Figure 7 shows the maximum calculated power and the average amplitude of oscillation for each cross section including the corresponding arm ratio. The power spectrum density (PSD) of the angular velocity (which is widely being used for measuring the performance of random vibration converters) is used to calculate the power. The cumulative spectral power (CSP) of the PSD is then calculated by integrating over all frequencies base on the Parseval's theorem and used to estimate the dissipated power [16,17]

$$CSP = P = \frac{I_t}{Q}\int_0^\infty (PSD)df \tag{5}$$

where $Q = \sqrt{KI_t}/C_t$ is the quality factor and the PSD is calculated by using the fast Fourier transform of the angular velocity:

$$PSD = |FFT(\dot{\theta}(t))|^2 \tag{6}$$

where $\dot{\theta}(t)$ is the angular velocity of the vibration. By comparing the two charts, it is clear that the amplitude is not a proper performance metric even though it's been reported in many studies. For example, the highest power is achieved for the circular cross section while the box cross section oscillated with higher amplitude.

According to the results, the angular velocity is lower near the ends of oscillation for the non-circular cross sections when pivoted on the downstream. There are two possible reasons for lower angular velocity in a cross section: First is the higher drag force in a higher angle of attacks in non-circular cross sections [18]. Higher drag force changes the stiffness nonlinearly and shifts the natural frequency f_v out of the lock-in range based on the following equation derived from the equation of motion:

$$f_N = \frac{1}{2\pi}\sqrt{\frac{K \pm l\,A_{D0}U^2}{I_t}} \tag{7}$$

where $+l$ and $-l$ correspond to the location of the pivot point on the upstream side or downstream side, respectively. $A_{D0} = \frac{1}{2}\rho DH_w C_D U^2$ and DH_w is the projected area of the cross section. For higher arm length, this increase in drag completely suppresses the vibration. The second reason is the lower spanwise correlation length. The first reason is discussed as vibration mechanism followed by a discussion over vorticity dynamic to understand the behavior of fluid around each section and its effect on correlation length.

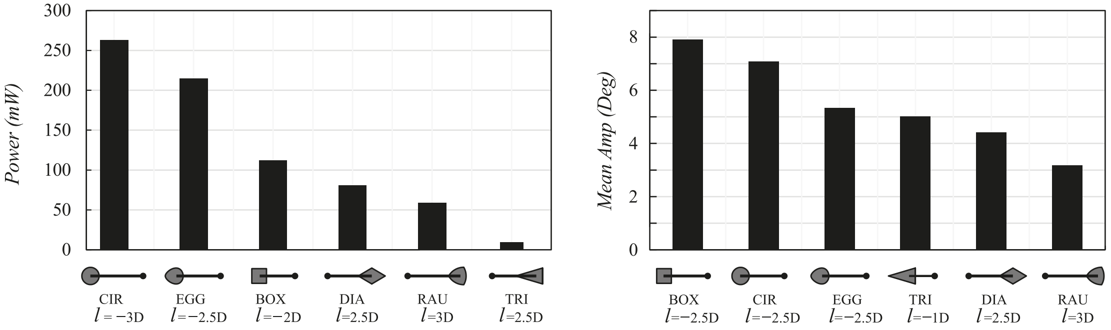

(*a*) (*b*)

Figure 7. The maximum power output (**a**) and the mean amplitude (**b**) for each cross section.

5.1. Vibration Analysis

According to Figure 7, only the CIR and EGG cross sections produce reasonable power followed by BOX with a large difference (of around 50% lower power). The drag, lift, and moment ratio versus arm ratio are shown in Figure 8 for all sections along with the calculated power on a separate axis. These three sections show more power while the pivot is on the downstream side of the section as shown in Figure 8. However, the power is nearly zero for a BOX section pivoted on the upstream side ($l > 0$) regardless of the length of the arm. The opposite behavior is observed for DIA section: the power is nearly zero for a DIA section pivoted on the downstream side ($l < 0$) regardless of the length of the arm. The two remaining sections (RAU, TRI) show the lowest power with almost no effect of the arm length and the pivot location. The difference between the BOX and the rest of the sections is more clear by analyzing the vibration response shown in Figure 9. The vibration frequency (f_v) is far away from the natural frequency while the pivot is at the downstream of the section but it gradually goes up and close to the natural frequency. Even though aeroelastic instability is expected to be responsible for oscillation in this kind of cross section, the lock-in phenomena seem to improve the oscillation for sections with round edges. A similar change is seen for the Strouhal number St ($= f_s D/U$), where $= f_s$ is the predominant vortex shedding frequency), as shown in Figure 9. The Strouhal number is very low for the BOX section while pivoted on the downstream. It eventually increases by the arm length and converges to 0.13 but for the rest of the sections, the Strouhal number is close to 0.2 which is considered in the lock-in range.

The maximum power depends largely on the natural frequency of the system which is a function of the pivot location and spring stiffness in our setup. Arionfard and Nishi [5] found that for a circular cross section the drag force assists the motion by reducing the natural frequency when the pivot is located at the downstream side of the cylinder ($l < 0$)

based on Equation (7). As the moment of inertia (I_t), flow velocity (U), spring stiffness (K), and the projected area of the sections are constant, $l\,A_{D0} \propto l\,C_D$ is responsible for changes in the natural frequency.

Note that the mathematical analysis provided in [5] is only valid for round shapes where the drag and lift coefficients are not a function of the angle of attack. This is with agreement with the results shown in Figure 8: The calculated power changes with $l\,C_D$ for CIR, EGG, and RAU shape while the calculated power for BOX, DIA, and TRI shapes shows less dependency to the drag coefficient or arm length.

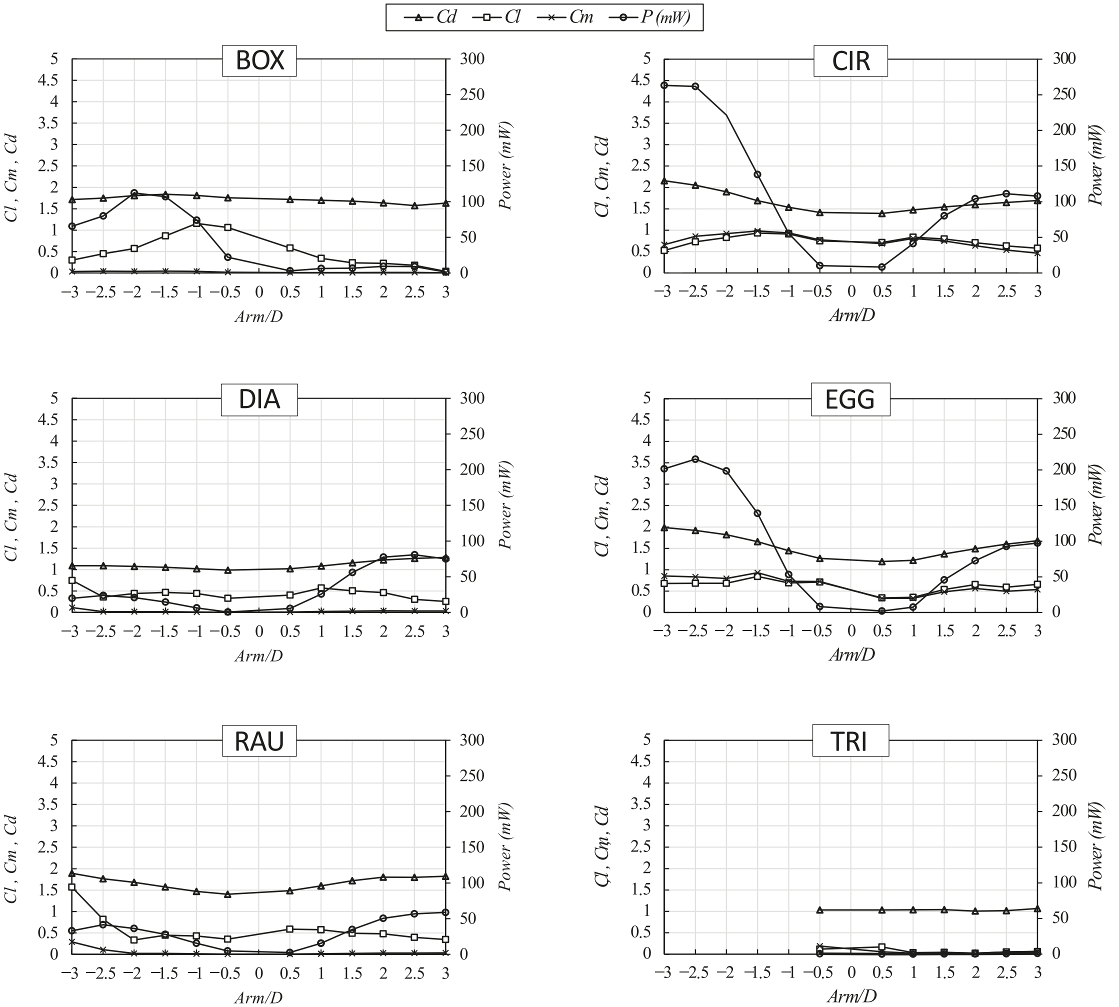

Figure 8. The calculated drag, lift, and moment ratios versus arm ratio for each cross-section. The calculated power is shown on a second Y-axis.

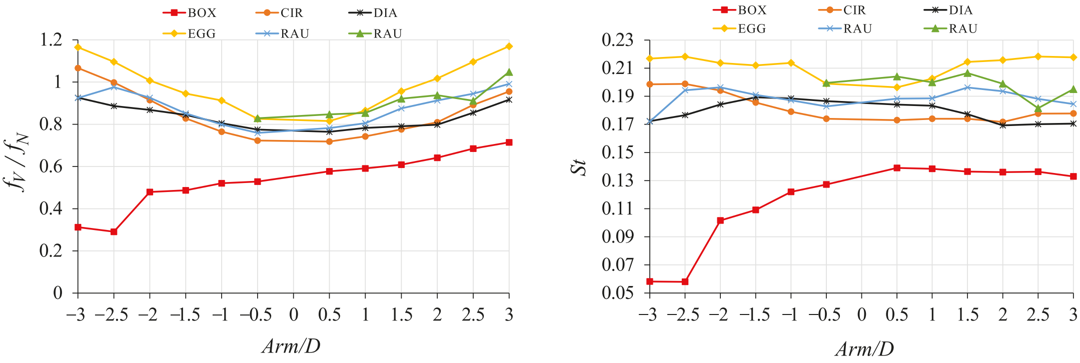

(a) *(b)*

Figure 9. (**a**) The frequency ratio verses the arm ratio for each cross section. (**b**) The Strouhal number versus the arm ratio for each cross section. Here, negative Arm/D represents a pivot point at the downstream of the cross section and positive Arm/D represents a pivot point at the upstream side of the cross section

5.2. Vorticity Analysis

The steady-state vorticity field for the cases with the highest performance is shown in Figure 10. For sufficient oscillation amplitudes, symmetrical shedding with 2S mode is triggered in all cases as expected due to the low Reynolds number. The 2S mode is associated with the initial branch [19] where two single vortices shed per cycle, one by the top shear layer and another one by the bottom shear layer. The vorticity field animations can be found in the Supplementary Videos S1–S6.

To compare the correlation length (which is a measure of the span-wise length, that the vortices remain in phase) for each section, the three-dimensional state of the wake for each simulated case is visualized in Figures 11 and 12. The wakes are extracted by using a threshold filter the way that the pressure lies within 10 to 100 Pascal for all cases. A few factors influence the correlation length in FIV, including the amplitude of vibration, aspect ratio, surface roughness and the Reynolds number [15]. Here, the Reynolds number and surface roughness are similar for all cases while the amplitude of vibration and aspect ratio (which is a function of geometry) are changing.

The correlation length is higher when the pivot is at the upstream side ($l > 0$) for all sections except for the BOX. It is well known that body motion at a frequency close to that of the natural vortex shedding has a strong organizing effect on the shedding wake, which is manifested by a sharp increase in the spanwise correlation of the flow and forces on the body. However, the increase in three dimensionality of the flow behind the BOX section contradicts this pattern. A similar increase in three dimensionality is observed for the TRI section as well, but it is due to smaller vibration amplitude for all lengths in this section. The formation of the vortex line for the cross sections with the highest calculated power is more evident in the animations provided in the online Supplementary Videos V1–V6.

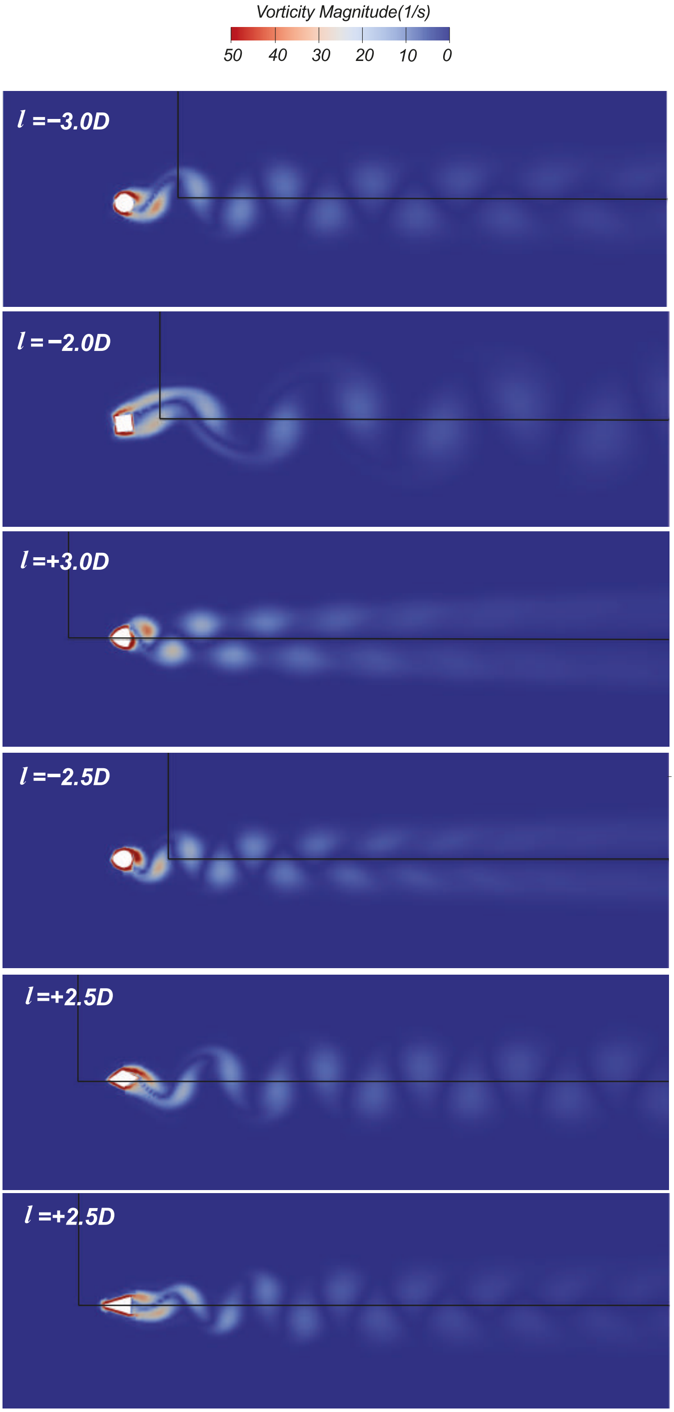

Figure 10. The steady state vorticity field for all cases with highest performance. The pivot is located at the origin of the black axes and the arm length is shown on top-left of each figure.

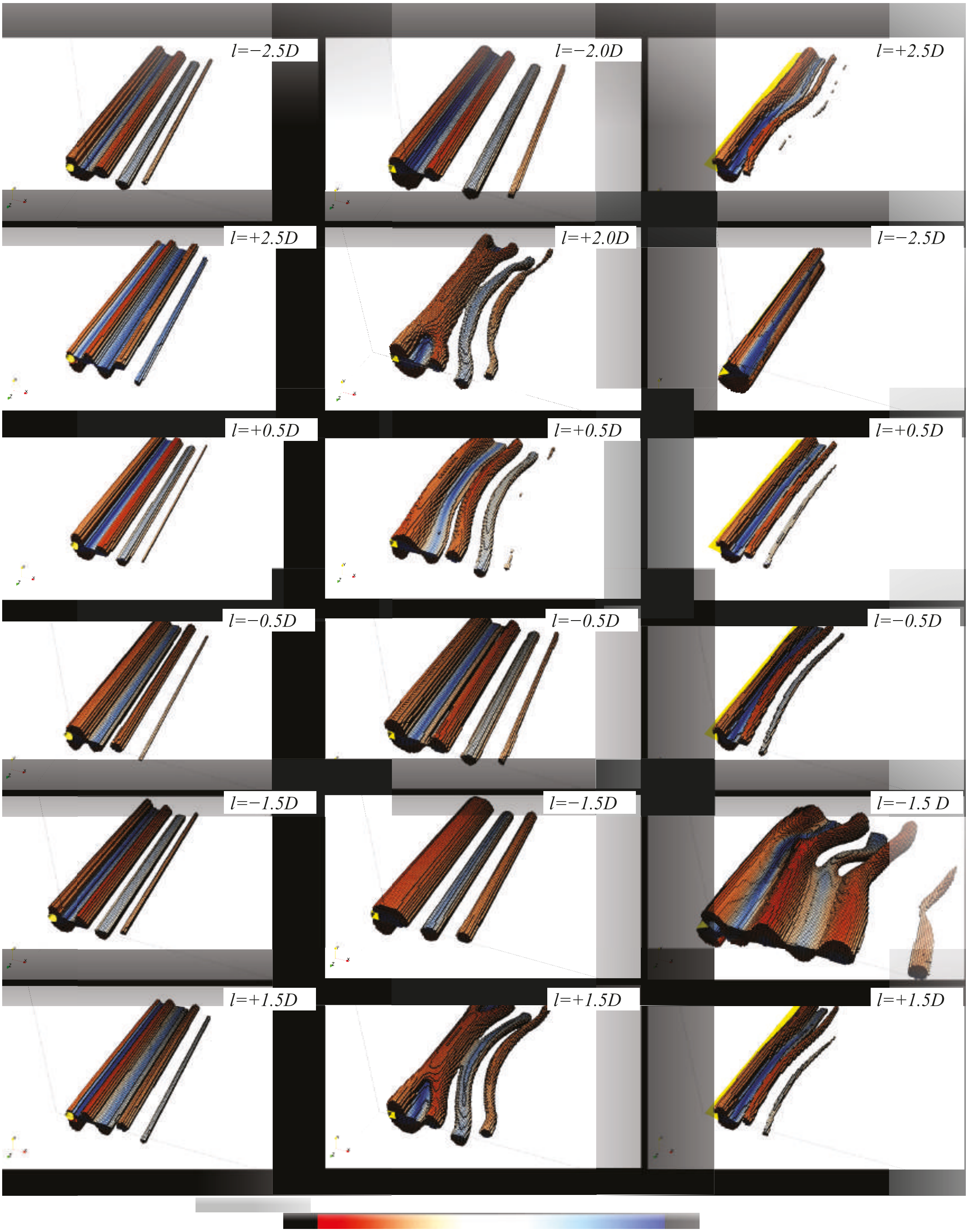

Figure 11. The velocity field on the wake side of the cylinders. The wakes are extracted by using a threshold filter on the pressure within 10 to 100 Pascal.

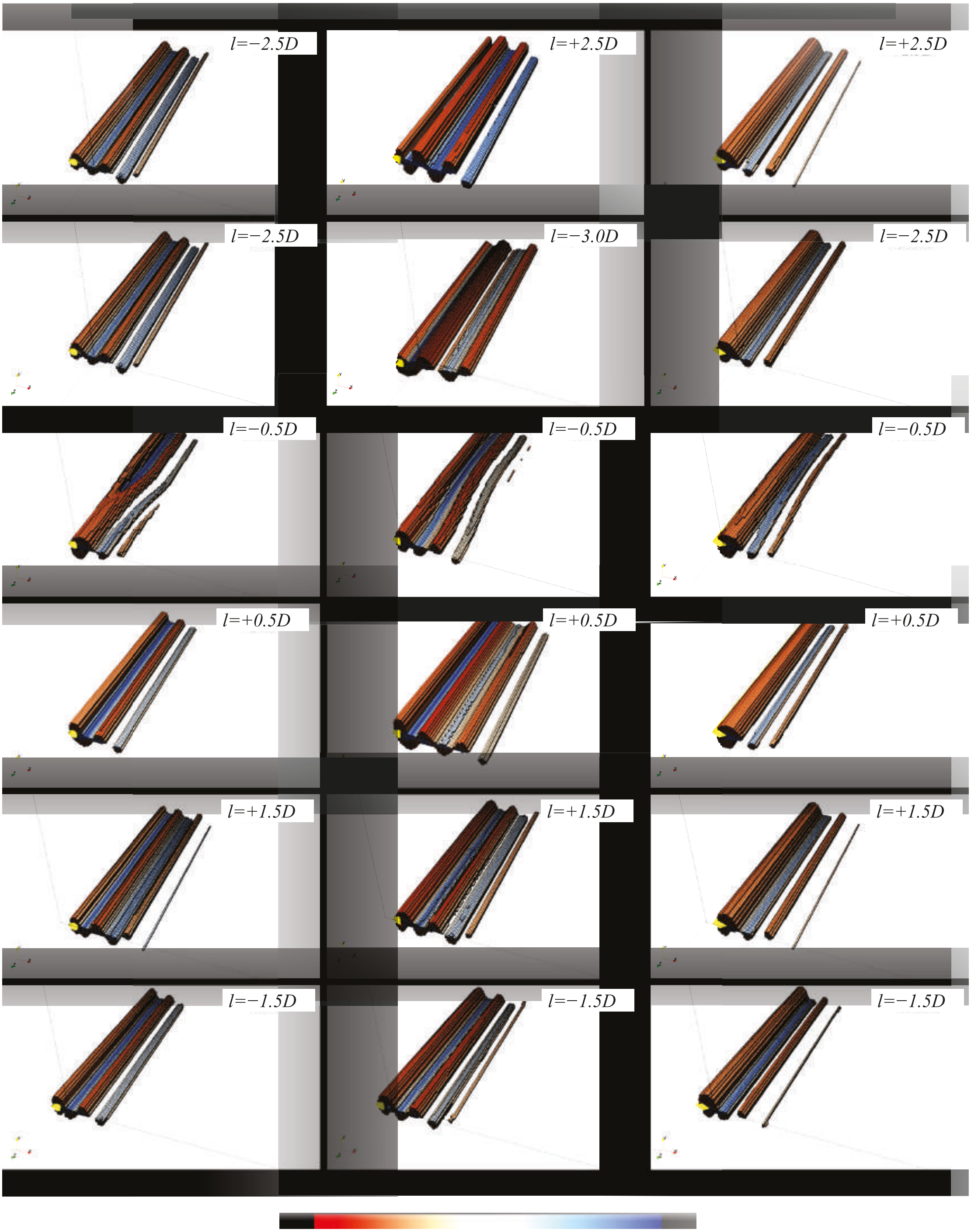

Figure 12. The velocity field on the wake side of the cylinders (continued).

6. Conclusions

3D numerical simulation of fluid-induced vibration has been reported for a series of cylinders with different cross sections including circular, rectangle, diamond, triangle, reuleaux, and egg shape. The cylinders are pivoted at distance from the centre to study the geometrical effect of the FIV performance and to compare the results with our previous experimental study. The cross-sectional area, moment of inertia, spring stiffness, inlet velocity, and damping coefficient are set to be similar for all cases to eliminate the effect of non-geometrical parameters. According to the results, the circular and egg shape cross sections are the most efficient shapes regardless of the pivot location followed by the box, diamond, reuleaux, and triangle shapes. The vorticity field shows that the 2S mode is triggered for all cases mainly due to the low Reynolds number; thus, the vibrations are expected to be in the initial branch. Moreover, 3D visualization of the wake for each section shows that the correlation length is higher for round shapes especially when the pivot is at the upstream side while for the shapes with sharp edges, the three-dimensionality of the wake is higher.

There are two major limitations in this study that could be addressed in future research. First, the domain size: even though a grid independency study is done for the circular cylinder and there is a good agreement with the experiment, similar results are not necessarily expected for other cross sections or arm lengths. This applies to the blockage ratio as well. It is assumed that the blockage has a similar effect on all cases if kept constant for all cross sections. Second, the Reynolds number: the results are compared to the experiments done with Reynolds number of around 2800 assuming both numerical and experimental tests are in the same flow regime ($1000 \geq Reynolds \geq 3000$). Moreover, the Reynolds number in this study is much smaller than that of actual operating conditions. Being aware of the limitations of this numerical study, we concluded that the hydrodynamic forces, displacement and calculated power of the cross sections are still comparable with each other if not to the experiment.

Supplementary Materials: The following are available online at https://www.mdpi.com/1996-1073/14/4/1128/s1, Video V1: The velocity field on the wake side of the BOX ($l = -2D$), Video V2: The velocity field on the wake side of the CIR ($l = -3D$), Video V3: The velocity field on the wake side of the DIA ($l = +2.5D$), Video V4: The velocity field on the wake side of the EGG ($l = -2.5D$), Video V5: The velocity field on the wake side of the RAU ($l = +3D$), Video V6: The velocity field on the wake side of the TRI ($l = +2.5D$), Video S1: The vorticity field for the CIR ($l = -3D$), Video S2: The vorticity field for the DIA ($l = +2.5D$), Video S3: The vorticity field for the EGG ($l = -2.5D$), Video S4: The vorticity field for the RAU ($l = +3D$), Video S5: The vorticity field for the TRI ($l = +2.5D$), Video S6: The vorticity field for the BOX ($l = -2D$).

Author Contributions: Formal analysis, S.M.; Investigation, H.A.; Visualization, H.A.; Writing—original draft, S.M. All authors have read and agreed to the published version of the manuscript.

Funding: This research received no external funding.

Acknowledgments: The authors wish to thank Fatemeh Talebi for her useful input and contribution. The calculations were carried out on supercomputer ABACUS 2.0 provided by the Southern Denmark University's eScience Center.

Conflicts of Interest: The authors declare no conflict of interest.

References

1. Bernitsas, M.M.; Raghavan, K.; Ben-Simon, Y.; Garcia, E.M.H. VIVACE (Vortex Induced Vibration Aquatic Clean Energy): A New Concept in Generation of Clean and Renewable Energy From Fluid Flow. *J. Offshore Mech. Arct. Eng.* **2008**, *130*, 1–15. [CrossRef]
2. Hobbs, W.B.; Hu, D.L. Tree-inspired piezoelectric energy harvesting. *J. Fluids Struct.* **2012**, *28*, 103–114. [CrossRef]
3. Yoshitake, Y.; Sueoka, A.; Yamasaki, M.; Sugimura, Y.; Ohishi, T. Quenching of vortex-induced vibrations of towering structure and generation of electricity using Hula-Hoops. *J. Sound Vib.* **2004**, *272*, 21–38. [CrossRef]
4. Sung, H.G.; Baek, H.; Hong, S.; Choi, J.S. Numerical study of vortex-induced vibration of pivoted cylinders. *Ocean Eng.* **2015**, *93*, 98–106. [CrossRef]

5. Arionfard, H.; Nishi, Y. Experimental investigation of a drag assisted vortex-induced vibration energy converter. *J. Fluids Struct.* **2017**, *68*, 48–57. [CrossRef]
6. Arionfard, H.; Nishi, Y. Flow-induced vibrations of two mechanically coupled pivoted circular cylinders: Characteristics of vibration. *J. Fluids Struct.* **2018**, *80*, 165–178. [CrossRef]
7. Arionfard, H.; Nishi, Y. Flow-induced vibration of two mechanically coupled pivoted circular cylinders: Vorticity dynamics. *J. Fluids Struct.* **2018**, *82*, 505–519. [CrossRef]
8. Arionfard, H.; Nishi, Y. Experimental investigation on the performance of a double-cylinder flow-induced vibration (FIV) energy converter. *Renew. Energy* **2019**, *134*, 267–275. [CrossRef]
9. Peng, Z.; Zhu, Q. Energy harvesting through flow-induced oscillations of a foil. *Phys. Fluids* **2009**, *21*, 123602. [CrossRef]
10. Ali, M.; Arafa, M.; Elaraby, M. Harvesting Energy from Galloping Oscillations. In Proceedings of the World Congress on Engineering, London, UK, 3–5 July 2013; Volume III.
11. Nakamura, Y.; Hirata, K. Critical geometry of oscillating bluff bodies. *J. Fluid Mech.* **1989**, *208*, 375–393. [CrossRef]
12. Al-Asmi, K.; Castro, I.P. Vortex shedding in oscillatory flow: Geometrical effects. *Flow Meas. Instrum.* **1992**, *3*, 187–202. [CrossRef]
13. Chowdhury, A.M.; Akimoto, H.; Hara, Y. Comparative CFD analysis of Vertical Axis Wind Turbine in upright and tilted configuration. *Renew. Energy* **2016**, *85*, 327–337. [CrossRef]
14. Pan, Z.Y.; Cui, W.C.; Miao, Q.M. Numerical simulation of vortex-induced vibration of a circular cylinder at low mass-damping using RANS code. *J. Fluids Struct.* **2007**, *23*, 23–37. [CrossRef]
15. A Rahman, M.; Rahman, M. Vortex-Induced Vibration of Cylindrical Structure with Different Aspect Ratio. Ph.D. Thesis, The University of Western Australia, Western Australia, Australia, 2015.
16. Ananthakrishnan, A.; Kozinsky, I.; Bargatin, I. Limits to inertial vibration power harvesting: power-spectral-density approach and its applications. *arXiv* **2014**, arXiv:1410.4734.
17. Peters, R.D. Tutorial on Power Spectral Density Calculations for Mechanical Oscillators. Available online: http://physics.mercer.edu/hpage/psd-tutorial/psd.html (accessed on 25 August 2020)
18. Matsumoto, M. Vortex shedding of bluff bodies: A review. *J. Fluids Struct.* **1999**, *13*, 791–811. [CrossRef]
19. Khalak, A.; Williamson, C.H.K. Motions , forces and mode transitions in Vortex-Induced Vibrations at low mass-damping. *J. Fluids Struct.* **1999**, *13*, 813–851. [CrossRef]

energies

MDPI

Article

Innovation of Pump as Turbine According to Calculation Model for Francis Turbine Design

Martin Polák

Faculty of Engineering, Czech University of Life Sciences Prague, Kamýcká 129, 16521 Praha 6, Czech Republic; karel@tf.czu.cz

Abstract: The effective utilization of micro hydropower sources is often realized through the use of pumps as turbines (PAT). The efficiency of PAT is about the same as that of the original pump. A further increase in efficiency and power output can be achieved by modifying the parts interacting with the flow, especially the impeller and the adjacent volute casing and draft tube. This paper presents a user-friendly calculation model of Francis turbine design and its application for PAT geometry modification. Two different modifications of a single-stage radial centrifugal pump were designed according to this model. The first modification (Turbine) consisted of a complete revision of the impeller geometry, volute casing and draft tube, which corresponded to a conventional Francis turbine. The second modification (Hybrid) was based on altered calculation model and consisted of a modification of only the impeller, which can be used in the original volute casing. Both modifications were tested on hydraulic test circuit at different heads. A comparison of the results of the Hybrid and the Turbine modification with the unmodified machine (Original) proved an increase in overall efficiency by 10%. Both modifications provided a higher flow rate and torque. This resulted in an overall power output increase—an increase of approximately 25% and 40% due to the Turbine and Hybrid modifications, respectively.

Keywords: pump as turbine (PAT); Francis turbine; calculation model; efficiency; hydropower

Citation: Polák, M. Innovation of Pump as Turbine According to Calculation Model for Francis Turbine Design. *Energies* **2021**, *14*, 2698. https://doi.org/10.3390/en14092698

Academic Editors: Adam Adamkowski and Anton Bergant

Received: 3 April 2021
Accepted: 26 April 2021
Published: 8 May 2021

1. Introduction

The ability of pumps to operate efficiently in reverse mode as turbines was first established by Thoma [1] in 1931, while mapping the full operating characteristic of a centrifugal pump. In recent decades, there has been renewed interest in the use of pumps as turbines (PATs). It has been significantly used in power supply installations in remote areas, both on- and off-grid. A comprehensive overview of the current state of knowledge and experience in this area was provided by Carravetta et al. [2]. In addition to small hydropower plants, PAT is also used for energy recovery to cover the need for pressure reduction in water distribution networks (WDN) [3]. Besides power generation, PAT also acts as a throttle valve for flow control in this case. Experience with these applications was described by Venturini [4]. A case study of a specific installation (including an economic evaluation) was presented by Stefanizzi [5].

A pump design for turbine mode is a separate issue, which has been addressed many times. A chronological overview of the individual methods used for a solution was given by Ballaco [6]. An analysis of the models used for designing PAT and its experimental verification can be found in Stefanizzi [7], Derakhshan [8], and Barabareli [9]. It should be added that experimental investigations are still indispensable when an exact knowledge of turbine characteristics is required [10]. An example of a method used for determining such characteristics and their subsequent use for parameter conversion in the case of the hydrotechnical potential changing was given by Polák [11].

Various authors have provided several relatively simple modifications with positive results (such as modifications consisting of the impeller tip and hub/shroud rounding) in order to increase overall PAT efficiency. Specific example can be found in Singh [12,13], Doshi [14], and others. Capurso [15] dealt with the issue of the impact of blade geometry modification. More technically demanding modification of the pump (consisting of the installation of guide vanes in front of the impeller) was described by Giosio [16]. Some authors dealing with PAT design and modifications (such as Frosina [17]) followed the path of numerical flow modelling. However, such procedures already require specialized software, which is not available to a wide range of users. The aim of this study is to create a user-friendly design of a Francis turbine impeller and to experimentally verify its results as applied in the PAT modification.

2. Calculation Model

This section presents a calculation model, which was originally used to design the impellers of low specific speed Francis turbines; it is based on a method detailed in [18]. However, a modified model can also be used to great effect for the design of the geometry modification of an impeller for PAT. For experimental verification of the model results, the test impeller was manufactured according to the calculation model used for a particular PAT. The impeller was then tested on a hydraulic circuit. The test results are presented in the second part of the article. The model is designed as a mathematical algorithm, for which any software that has mathematical functions can be used. In this case, MS Excel software was used to ensure maximum clarity of the results and simple operation. The user then worked with the MS Excel calculation protocol. The input variables of the calculation model are the hydrotechnic potential of the turbine installation site and the size (diameter) of the impeller. The potential is given by the net head H (m) and the flow rate Q ($\mathrm{m}^3\cdot\mathrm{s}^{-1}$). Based on these values, the specific speed of the turbine (with regard to the power Ns (min^{-1})) is estimated from the following equation:

$$Ns = N\cdot\sqrt{g}\cdot\frac{Q^{1/2}}{H^{3/4}} \tag{1}$$

where N (min^{-1}) is the assumed turbine shaft speed and g ($\mathrm{m}\cdot\mathrm{s}^{-2}$) is the gravitational acceleration [19]. The value of Ns is entered into the green-coloured cell on the 1st line in the calculation protocol on page 6. The net head of the site H (m) is entered in line 8. Another necessary input value is the outer diameter of the impeller D_1 (m), which is entered in line 9. All key input variables are thus given.

To design the impeller, the calculation model uses the theory of hydraulic similarity, based on the geometric similarity of velocity triangles. Velocity triangles are related to performance parameters by means of Euler's equation [20]:

$$Y_T = u_1\cdot c_{u1} - u_2\cdot c_{u2} \tag{2}$$

or:

$$\eta_T\cdot\rho\cdot g\cdot Q\cdot H = \rho\cdot Q(u_1\cdot c_{u1} - u_2\cdot c_{u2}) \tag{3}$$

where Y_T ($\mathrm{J}\cdot\mathrm{kg}^{-1}$) is the turbine specific energy, u_1, c_{u1} and u_2, c_{u2} ($\mathrm{m}\cdot\mathrm{s}^{-1}$) are the velocity triangles vectors at the impeller inlet and outlet, respectively (see Figure 1), η_T (-) is the turbine efficiency, and ρ ($\mathrm{kg}\cdot\mathrm{m}^{-3}$) is the fluid density.

The assumed total efficiency η_T is based on the size of the turbine here (i.e., on the outer diameter of the impeller D_1 according to Moody's relation [21]):

$$\eta_T = 1 - (1-\eta_M)\sqrt[4]{\frac{D_M}{D_1}} \tag{4}$$

where η_M (1) is the efficiency of the corresponding turbine with the impeller diameter D_M (m).

The described calculation model allows for the designing of turbine impellers' geometry with specific speed values Ns = 80 min^{-1} and higher [18]. Figure 2 shows a diagram of the simplified overview of its algorithm. The background colours in the diagram correspond to the colours of the cells in the calculation protocol.

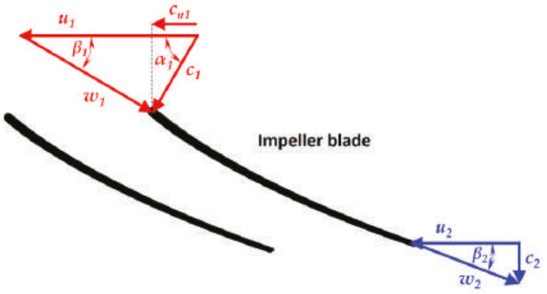

Figure 1. Velocity triangles at the inlet and outlet of the Francis impeller blade.

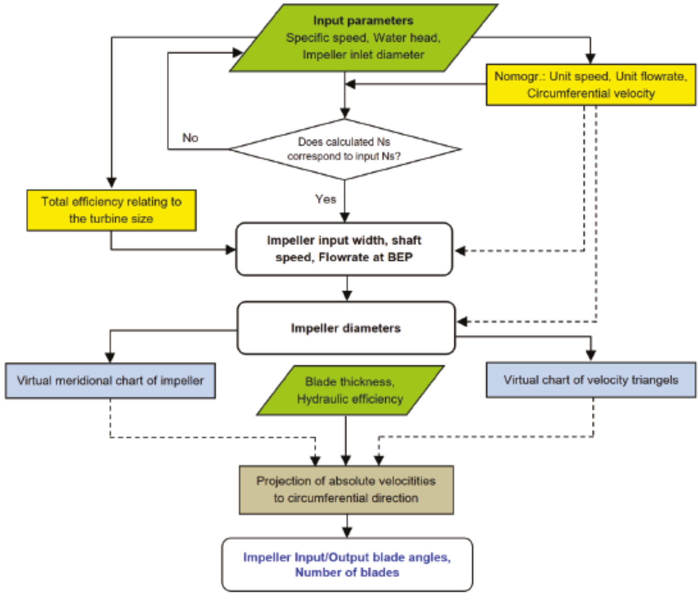

Figure 2. Algorithm of the impeller design in the calculation model.

The procedure stemming from the original design of the model required the entry of some dimensional characteristics directly from the drawing of the impeller meridional cross-section (see Figure 3). It had to be drawn at a certain stage of the impeller design. For greater user comfort, this phase was converted by the author into a calculation algorithm by means of mathematical functions, which is then used by the model for further designs. However, this "service" can be used only for limited range of specific speed Ns = 80 to 100 min^{-1}. The model can be also used for designing an impeller with a higher specific speed, but the required geometric characteristics need to be entered manually (lines 28, 29 and 31, 32) based on a self-made drawing. The procedure of this drawing is to divide the flow area of the impeller meridional cross-section into partial streams (two streams are sufficient in the case of a low specific speed narrow impeller, as shown in Figure 3). The border streamline is drawn at the inlet in the middle of the channel height. Inside the channel, the course of the streamlines is determined on the orthogonal trajectory using circles inscribed between the border streamline and the impeller contour (see Figure 3). At the same time, the multiplication of the diameters of these circles and the distances of their centres from the turbine axis must be approximately the same for all of them [18].

$$d_{AB} \cdot r_{AB} = d_{BC} \cdot r_{BC} = const. \tag{5}$$

Based on this requirement, the impeller flow area is divided and the values d_{AB}, r_{AB} and d_{BC}, r_{BC} gained from the drawing are entered into the above-mentioned lines.

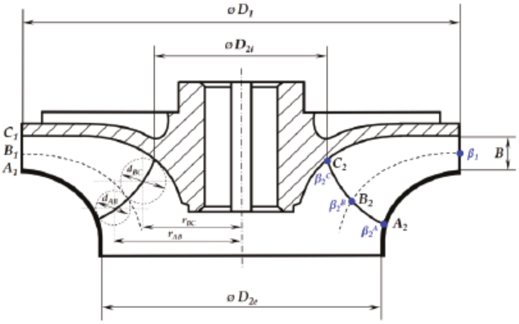

Figure 3. Meridional cross-section of the turbine impeller.

The values in the yellow-coloured cells in the calculation protocol are determined on the basis of mathematical functions, which the author created from the curves of the nomograms of the original Francis turbine design. To illustrate this, Figure 4 shows an example of the transformation of the curve $B/D_{1e} = f(Ns)$ from a nomogram to a mathematical function. The default original nomogram is at the bottom left, and a graphical representation of the transformation result can be seen at the top right. The black dashed line here corresponds to the original curve and the red line is calculated from the polynomial function shown below the graph. This equation is then used in the calculation model, namely in line 10.

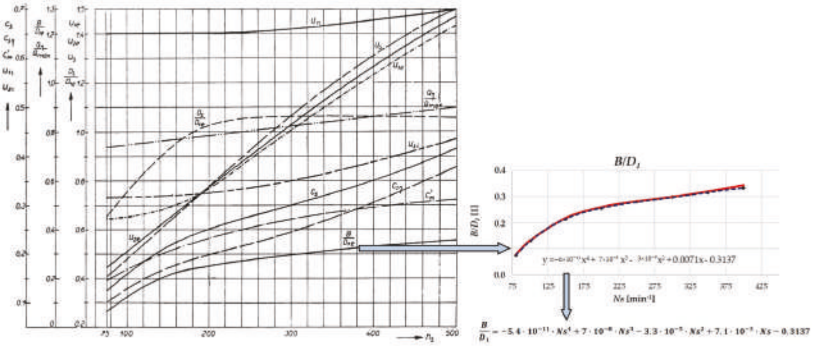

Figure 4. An example of transformation of curve from nomogram to mathematical function. Reproduced and modified from [18], SNTL Prague: 1962.

Some curves in the nomograms may differ according to different authors. The calculation model also takes this fact into account and allows a more experienced user to intervene in the calculation and change the values in the yellow cells as needed.

The next section of the impeller design (lines 35 to 39) is a combination of the previous results and the graphic construction of the velocity triangles. Again, in the original calculation design, making the drawing of triangles manual and measuring the values from the drawn construction for further calculation were required at this stage. Regarding maximum user comfort, these "manual" operations (presented in the diagram in Figure 2 by the dashed line) were transformed into mathematical functions and used by the calculation model in further operations.

The final outcomes of the model are the basic geometry characteristics for impeller construction, summarized in the form of the calculation protocol (see Figure 5). Besides the main impeller dimensions, the values of the angles (α_1, β_1) for the geometry of velocity triangles (or the blade at the inlet) are presented here. The shape of the blade at the outlet is determined by angles at three points—on the outer (${\beta_2}^A$), mean (${\beta_2}^B$), and inner streamline (${\beta_2}^C$). The number of impeller blades z is presented at the very end of the protocol in line 48. In addition, the model also indicates the shaft speed N (line 12) and the flow rate Q_η (line 14) corresponding to the optimum operation (BEP) at a given net head H.

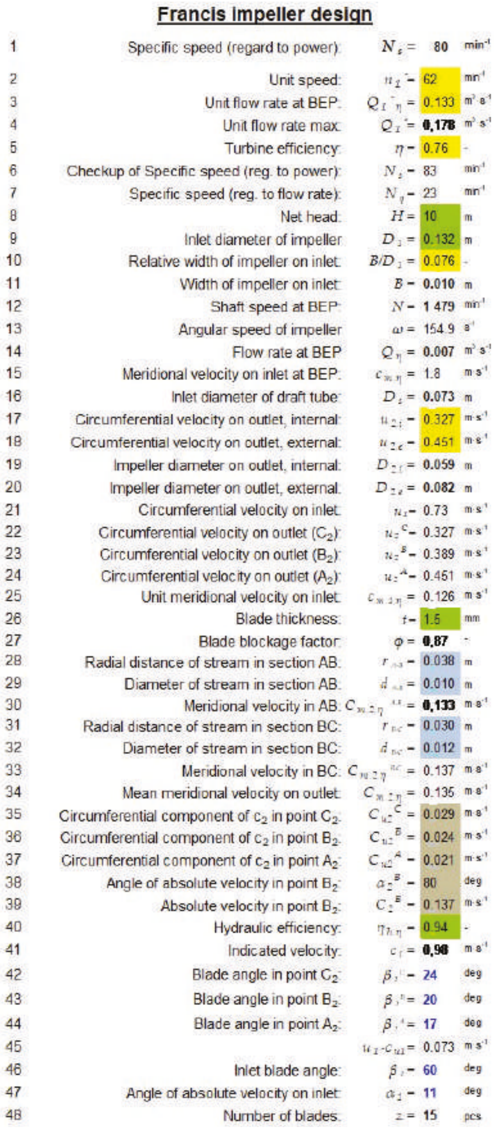

Francis impeller design

1	Specific speed (regard to power):	$N_s =$	80	min^{-1}
2	Unit speed:	$n_1' =$	62	mn^{-1}
3	Unit flow rate at BEP:	$Q_{1\eta}' =$	0.133	$\text{m}^3\,\text{s}^{-1}$
4	Unit flow rate max:	$Q_1' =$	**0,178**	$\text{m}^3\,\text{s}^{-1}$
5	Turbine efficiency:	$\eta =$	0.76	-
6	Checkup of Specific speed (reg. to power):	$N_s =$	83	min^{-1}
7	Specific speed (reg. to flow rate):	$N_q =$	23	mn^{-1}
8	Net head:	$H =$	10	m
9	Inlet diameter of impeller:	$D_1 =$	0.132	m
10	Relative width of impeller on inlet:	$B/D_1 =$	0.076	-
11	Width of impeller on inlet:	$B =$	**0.010**	m
12	Shaft speed at BEP:	$N =$	**1 479**	min^{-1}
13	Angular speed of impeller:	$\omega =$	154.9	s^{-1}
14	Flow rate at BEP:	$Q_\eta =$	**0.007**	$\text{m}^3\,\text{s}^{-1}$
15	Meridional velocity on inlet at BEP:	$c_{m1\eta} =$	1.8	$\text{m}\cdot\text{s}^{-1}$
16	Inlet diameter of draft tube:	$D_s =$	**0.073**	m
17	Circumferential velocity on outlet, internal:	$u_{2i} =$	0.327	$\text{m}\cdot\text{s}^{-1}$
18	Circumferential velocity on outlet, external:	$u_{2e} =$	0.451	$\text{m}\cdot\text{s}^{-1}$
19	Impeller diameter on outlet, internal:	$D_{2i} =$	**0.059**	m
20	Impeller diameter on outlet, external:	$D_{2e} =$	**0.082**	m
21	Circumferential velocity on inlet:	$u_1 =$	0.73	$\text{m}\cdot\text{s}^{-1}$
22	Circumferential velocity on outlet (C_2):	$u_2^C =$	0.327	$\text{m}\cdot\text{s}^{-1}$
23	Circumferential velocity on outlet (B_2):	$u_2^B =$	0.389	$\text{m}\cdot\text{s}^{-1}$
24	Circumferential velocity on outlet (A_2):	$u_2^A =$	0.451	$\text{m}\cdot\text{s}^{-1}$
25	Unit meridional velocity on inlet:	$c_{m1\eta} =$	0.126	$\text{m}\cdot\text{s}^{-1}$
26	Blade thickness:	$t =$	1.5	mm
27	Blade blockage factor:	$\varphi =$	**0,87**	-
28	Radial distance of stream in section AB:	$r_{AB} =$	0.038	m
29	Diameter of stream in section AB:	$d_{AB} =$	0.010	m
30	Meridional velocity in AB:	$C_{m2\eta}^{AB} =$	**0,133**	$\text{m}\cdot\text{s}^{-1}$
31	Radial distance of stream in section BC:	$r_{BC} =$	0.030	m
32	Diameter of stream in section BC:	$d_{BC} =$	0.012	m
33	Meridional velocity in BC:	$C_{m2\eta}^{BC} =$	0.137	$\text{m}\cdot\text{s}^{-1}$
34	Mean meridional velocity on outlet:	$C_{m2\eta} =$	0.135	$\text{m}\cdot\text{s}^{-1}$
35	Circumferential component of c_2 in point C_2:	$C_{u2}^C =$	0.029	$\text{m}\cdot\text{s}^{-1}$
36	Circumferential component of c_2 in point B_2:	$C_{u2}^B =$	0.024	$\text{m}\cdot\text{s}^{-1}$
37	Circumferential component of c_2 in point A_2:	$C_{u2}^A =$	0.021	$\text{m}\cdot\text{s}^{-1}$
38	Angle of absolute velocity in point B_2:	$\alpha_2^B =$	80	deg
39	Absolute velocity in point B_2:	$C_2^B =$	0.137	$\text{m}\cdot\text{s}^{-1}$
40	Hydraulic efficiency:	$\eta_{h\eta} =$	0.94	-
41	Indicated velocity:	$c_i =$	**0,98**	$\text{m}\cdot\text{s}^{-1}$
42	Blade angle in point C_2:	$\beta_2^C =$	24	deg
43	Blade angle in point B_2:	$\beta_2^B =$	20	deg
44	Blade angle in point A_2:	$\beta_2^A =$	17	deg
45		$u_1 - c_{u1} =$	0.073	$\text{m}\cdot\text{s}^{-1}$
46	Inlet blade angle:	$\beta_1 =$	60	deg
47	Angle of absolute velocity on inlet:	$\alpha_1 =$	11	deg
48	Number of blades:	$z =$	15	pcs

Figure 5. Calculation protocol of the Francis impeller design based on [18].

3. Experimental Verification of Proposed Modifications

For practical verification, the test impeller for this particular PAT was manufactured according to the design proposed by the calculation model. It was necessary to adapt the related flow parts at the same time (i.e., the volute casing and the draft tube). The fundamental change was to reduce the width of the impeller at the inlet from the original value of B = 16 mm to the width of B = 10 mm proposed by the model. The next change concerned the outlet cross section of the impeller. This was, on the contrary, necessary to increase the diameter (D_2 = 65 mm) for the original pump to the newly calculated value (D_2 = 84 mm). The impeller blades were also changed. A machine with completely new geometry was created, referred to as "Turbine" in the following text—see Figure 6 on the right. The original unmodified pump (META Plus 5 Czech Trade mark) is hereafter referred to as "Original" and is shown in Figure 6 on the left.

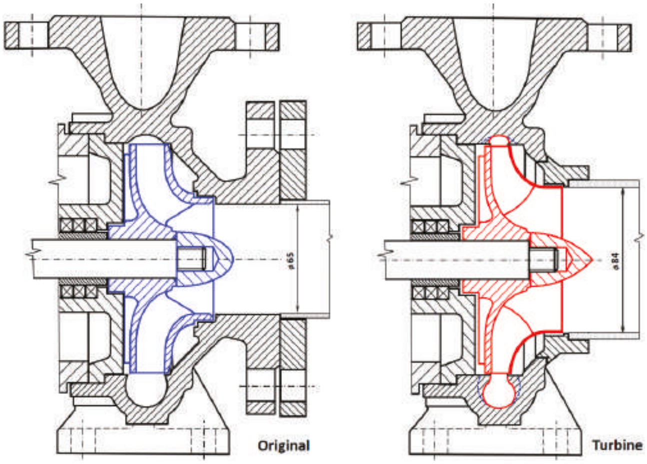

Figure 6. Cross-section of the Original PAT (**left**) and the Turbine after modification (**right**).

Photos of the impellers tested on the hydraulic circuit are shown in Figure 7. The unmodified original impeller on the left was made of cast iron in a sand mould. These types of impellers are used by the manufacturer as a standard for META Plus 5 pumps. The photo on the right is the impeller of the Turbine modification, with the geometry designed by the calculation model. To manufacture it, the hub and the rear shroud from the original impeller were used. The front shroud was made of copper sheet created by cold forming. All impeller blades were made from metal alloy by casting, and they were glued between the rear and the front shroud.

The numerical values of the geometry of both impeller variants are given in Table 1. The Turbine impeller has twice the number of blades compared to the Original. At the same time, the blades are almost half the length of the pump blades. This means a smaller wetted surface and, therefore, fewer hydraulic losses.

Table 1. Overview of the impellers' geometry.

Parameter		Original		Turbine	
		Inlet	**Outlet**	**Inlet**	**Outlet**
Diameter	D (mm)	132	65	132	84
Impeller width	B (mm)	16	-	10	-
Blade angle	β (mm)	24	18	60	20
Number of blades	z (-)	6		12	
Blade length	L (mm)	113		52	

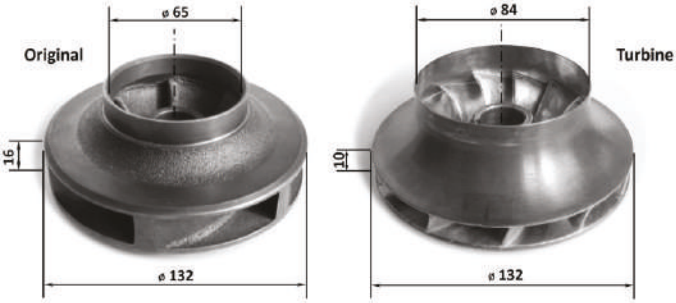

Figure 7. Impellers of tested variants—Original on the left, Turbine on the right.

An overview comparison of the geometry proposed by the calculation model with other Francis turbine impellers with corresponding specific speeds is given in Table 2. These are relative values related to the size of the impeller—outer diameter D_1. The results of the calculation model for the Turbine variant are shown in the left column of the table. The parameters of the test impeller of the Francis turbine F99 at NTNU Trondheim, Norway, are shown in the middle column [22]. The last column on the right presents the parameters of the Francis turbine impeller at Štěchovice hydroelectric power plant on the Vltava River, Czech Republic [18].

Table 2. Comparison of model results with the geometry of Francis turbines.

Parameter		Turbine, Model	F99, NTNU [22]	Štěchovice, CR [18]
Impeller diameter	D_1 (m)	0.132	0.622	2.47
Blade length	L/D_1 (-)	0.394	0.402	0.433
Impeller width	B/D_1 (-)	0.083	0.094	0.075
Outlet diameter	D_2/D_1 (-)	0.636	0.561	0.623
Blade angle—Inlet	β_1 (deg)	60	63	60
Blade angle—Outlet	β_2 (deg)	20	20	25

As the table above indicates, the basic geometric characteristics proposed by the calculation model correspond to the parameters of standard Francis turbines. Any differences may be caused by slightly different values of the specific speeds of individual types of impellers.

Hydraulic Test Circuit

Verification tests were conducted on an open hydraulic circuit in the laboratory of fluid mechanics at the Faculty of Engineering, Czech University of Life Sciences Prague. The circuit diagram is shown in Figure 8.

The test circuit consisted of a feeding pump, a reservoir with pipes, and control and measuring devices. With this setting, the feeding pump (FP) created the hydrotechnic potential for the tested PAT and the water flowed in the direction of the blue arrows. The generator with the momentum sensor (*D*) Magtrol TMB 307/41 (accuracy 0.1%) allowed for the continuous regulation of shaft speed via the frequency converter LSLV0055s100-4EOFNS. The water flow was measured using an electromagnetic flowmeter (*Q*) SITRANS FM MAG 5100 W (accuracy 0.5%). The pressures at p_p and p_s were measured by the pressure sensor HEIM 3340 (accuracy 0.5%), which was installed according to the first class accuracy requirements [23].

The hydraulic circuit described above was used for the testing of PAT variants with a head of 10 m, 20 m, and 30 m. The constant value of head was controlled by changing the speed of the feed pump by means of a frequency converter. Under these conditions, the basic parameters were measured, from which the performance characteristics were subsequently created.

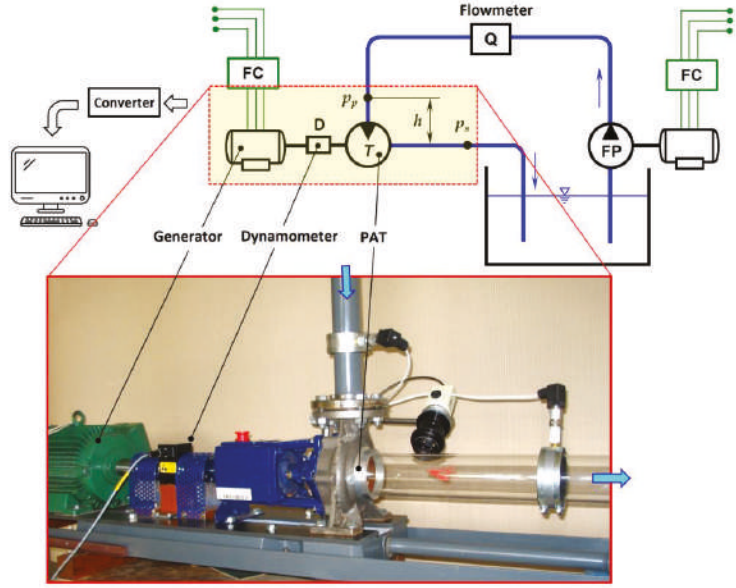

Figure 8. The hydraulic circuit scheme for testing PAT (Turbine variant shown in the photo): Q: flowmeter; FP: feed pump; PAT: pump as turbine; D: dynamometer; FC: frequency converter.

4. Results and Discussion

The partial results of the Original and the Turbine performance tests indicated the possibility of creating a new construction, which would be a combination of both variants. The aim was to maintain efficiency improvement while minimizing modifications to the pump. In accordance with these requirements, the calculation model was modified, and another variant of PAT was developed, which is referred to as "Hybrid" in the following text. The key outer dimensions of the Hybrid impeller remained the same in order to avoid volute casing modification. The purpose of this variant was to reduce the cost of the modification and, thus, the final price of PAT. The specific geometric parameters of the impeller are subject to the know-how of the author of the modification. It is the intellectual property of the university (CULS Prague) and can be provided on request. To manufacture this variant, the rear shroud of the original pump impeller was again used as a basis. Metal alloy blades were glued to the front shroud, and the entire product was glued to the rear shroud. The final appearance of PAT with this impeller visually corresponds to the variant in Figure 6 on the left.

The following charts indicate the performance characteristics of selected parameters depending on the shaft speed for all three variants of PAT—Original, Turbine, and Hybrid. The curves are created by mean values of three measurements at constant net head of 10 m, 20 m, and 30 m. There are also standard deviations marked on the curves. Values and curves corresponding to the unmodified Original variant are marked in blue. The characteristics of the Turbine and Hybrid variants are marked in red and green, respectively.

Figure 9 presents the first series of characteristics, which are the efficiency courses in dependence on the shaft speed. The increase in efficiency in both innovated variants is obvious. The absolute values of the efficiencies for BEP are summarized in Table 3. The relative increase regarding the Original is indicated in Table 4. The comparison at BEP also indicates a shift in the shaft speed to lower values, especially for the Hybrid variant.

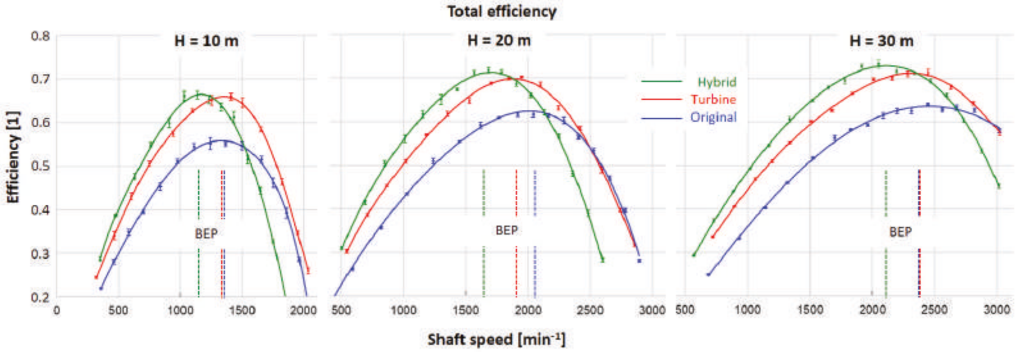

Figure 9. Efficiency in terms of dependence on shaft speed.

Figure 10 presents another series of characteristics—the dependence of torque on shaft speed. The comparison again indicates that the Turbine and the Hybrid variants prove higher torque, especially at lower speed.

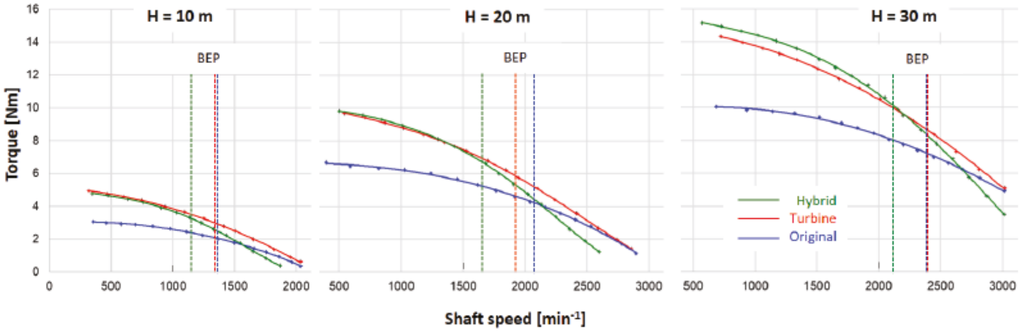

Figure 10. Torque in terms of dependence on shaft speed.

The mechanical power output courses (see Figure 11) basically copy the trends of the efficiency courses. The absolute values of the achieved power outputs obviously increase with increasing net head. The characteristics of the Turbine and the Hybrid also indicate a noticeably greater distance between the curves at higher net heads towards higher values. It is caused by a higher flow rate, as compared to that of the Original.

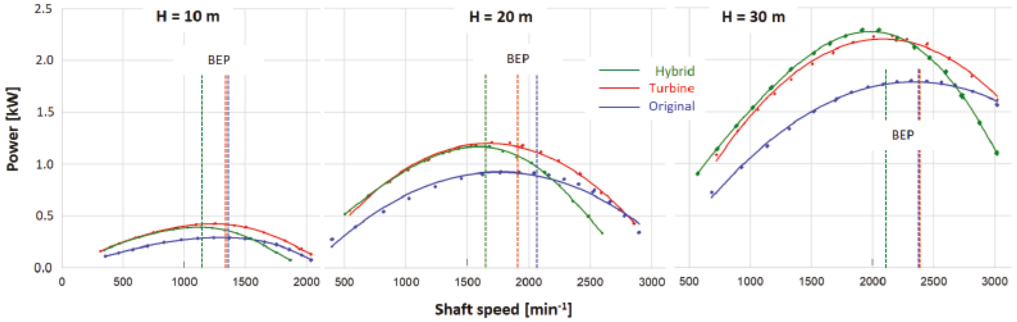

Figure 11. Courses of power output in terms of dependence on shaft speed.

The last series of characteristics represents courses of flow rate in terms of dependence on shaft speed (see Figure 12). The graphs of the flow rate courses indicate that the impeller´s flow rate decreases with increasing shaft speed. This characteristic also applies to Francis turbines with low specific speeds [20]. This is caused by the increasing centrifugal force, which acts against the centripetal direction of water flow.

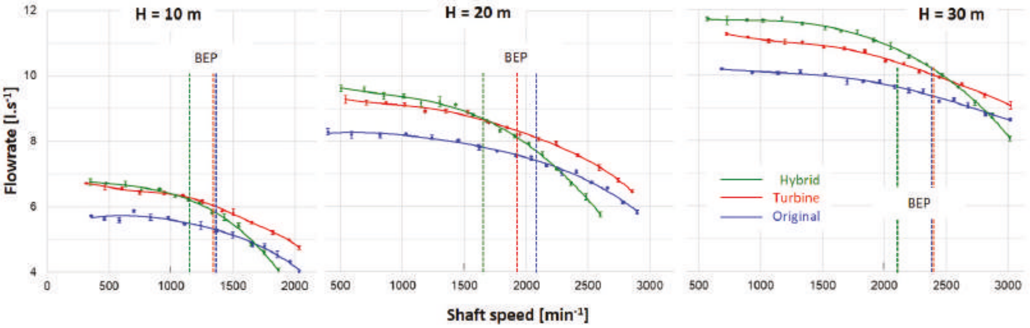

Figure 12. Courses of flow rate in terms of dependence on shaft speed.

Table 3. (**a**) Overview of absolute values of performance parameters achieved at BEP at net head of 10 and 20 m. (**b**) Overview of absolute values of performance parameters achieved at BEP at net head of 30 m.

(a)

Parameter		**10 m**			**20 m**		
		Turbine	**Hybrid**	**Original**	**Turbine**	**Hybrid**	**Original**
Shaft speed	N (min^{-1})	1353 ± 1	1149 ± 1	1358 ± 2	1910 ± 3	1709 ± 1	2029 ± 1
Power	P (kW)	0.36 ± 0.001	0.41 ± 0.001	0.28 ± 0.001	1.1 ± 0.002	1.23 ± 0.002	0.90 ± 0.001
Flow rate	Q (L/s)	5.6 ± 0.01	6.3 ± 0.03	5.2 ± 0.04	8.0 ± 0.01	8.8 ± 0.04	7.4 ± 0.06
Head	H (m)	10 ± 0.13	10 ± 0.13	10 ± 0.09	20 ± 0.07	20 ± 0.16	20 ± 0.22
Efficiency	η (%)	66 ± 0.8	66 ± 0.9	55 ± 0.5	70 ± 0.3	72 ± 0.6	62 ± 0.7
Torque	T (Nm)	2.7 ± 0.01	3.3 ± 0.003	2.0 ± 0.002	5.6 ± 0.004	6.7 ± 0.01	4.2 ± 0.005

(b)

Parameter		**30 m**		
		Turbine	**Hybrid**	**Original**
Shaft speed	N (min^{-1})	2408 ± 3	2078 ± 3	2402 ± 2
Power	P (kW)	2.05 ± 0.005	2.38 ± 0.004	1.70 ± 0.003
Flow rate	Q (l/s)	9.8 ± 0.02	11.0 ± 0.11	9.0 ± 0.03
Head	H (m)	30 ± 0.31	30 ± 0.36	30 ± 0.11
Efficiency	η (%)	71 ± 0.7	73 ± 0.9	64 ± 0.2
Torque	T (Nm)	8.2 ± 0.01	10.7 ± 0.01	6.9 ± 0.01

Table 4. Relative increases of the performance parameters at BEP related to the Original.

Parameter		**10 m**		**20 m**		**30 m**	
		Turbine	**Hybrid**	**Turbine**	**Hybrid**	**Turbine**	**Hybrid**
Shaft speed	%N (min^{-1})	−0.3	−15.4	−5.9	−15.8	0.3	−13.5
Power	%P (kW)	28.8	44.5	23.0	37.2	20.6	39.7
Flow rate	%Q (L/s)	7.5	20.0	8.0	17.9	8.3	22.2
Efficiency	%η (%)	19.8	20.5	13.8	16.3	11.3	14.4
Torque	%T (Nm)	33.7	67.9	32.7	59.1	20.1	56.7

The variability of the flow rate can be used in cases where PAT functions as a replacement for the throttle valve in water distribution networks (WDN). In this case, PAT must be equipped with shaft speed control (e.g., by means of a frequency converter). The disadvantage of these applications is the resulting small range of flow control. Here, in the case of the Original variant, it is possible to regulate the flow rate by changing the shaft speed in the range of 33% of the nominal flow rate ($Q = 0.77 \div 1.1 \cdot Q_{BEP}$). The Turbine variant shows higher flow rate, but the regulation range is roughly the same (i.e., 33% again ($Q = 0.8 \div 1.13 \cdot Q_{BEP}$)). From this point of view, the most interesting is the Hybrid variant, where the steepest course of the flow rate was indicated—from the highest Turbine values to the lowest Original values. In absolute value, the Hybrid variant allows regulation of up to 44% of the nominal flow rate ($Q = 0.66 \div 1.1 \cdot Q_{BEP}$). This modification therefore also opens a greater potential for the use of PAT as a replacement for a throttle valve.

The following Table 3 summarizes the absolute values of the performance parameters achieved at BEP. The values were corrected using affine relations to a constant net head of 10 m, 20 m, and 30 m.

From the achieved results, the relative increase in the parameters of the Turbine and the Hybrid variant related to the Original was subsequently determined:

$$\Delta A = 100 \cdot \frac{A_m - A_0}{A_0} \quad (\%) \tag{6}$$

where A_0 is a parameter of the Original and A_m is a parameter of the modification (Turbine or Hybrid). An overview of the relative increases in the performance parameters in comparison with those of the Original is presented in Table 4.

The technical implementation of such modifications is a challenge. Every PAT modification means an increase in price. From this point of view, the Hybrid variant, considering only a modification of the impeller, appears to be the most advantageous. The volute casing and the draft tube do not have to be modified. At present, the problem of impeller manufacturing could be solved with the help of so-called additive technologies, as they can be used to manufacture virtually any geometry. An alternative way is to manufacture only the impeller blades along with the front shroud. This unit can be then glued or welded to the rear shroud. The resultant experience and test results with such 3D printed impellers are presented by Polák [24].

5. Conclusions

The focus of this study is two-fold. The first focus is the presentation of a calculation model for the design of a low specific speed Francis turbine impeller. The second focus is an experimental verification of the results of this model for the design of PAT innovation in order to increase its efficiency. The algorithm of the calculation model combines the original graphic–numerical design of the geometry of the Francis impeller so that it is as user-friendly and clear as possible. The example of the numerical solution described in this article presents the results of the design of particular PAT with an impeller with a diameter of D_1 = 132 mm and a specific speed of Ns = 80 min^{-1}. A comparison of the geometry characteristics designed by the model with the realized Francis turbine impellers gives a corresponding likeness.

Based on the theoretical results, the manufacture of the impeller proposed by the calculation model was instigated. Thus, the Turbine variant, with a new impeller geometry and modification of the closely adjacent parts (i.e., the volute casing and the draft tube), was created.

Testing on a test circuit at 10 m, 20 m, and 30 m head proved that the Turbine variant has a positive effect on improving the efficiency of PAT—in terms of absolute value, the efficiency increased by up to 10% in optimal operation (BEP). The modification further resulted in a flow rate increase of roughly 8%. Added together, the overall PAT power output was increased by 25%. Due to the changed geometry of the impeller blades, the torque was increased by 20 to 30%. These promising results led to the modification of the calculation model, as well as the construction and testing of another variant—the Hybrid. Its mission was to maintain the positives achieved by the Turbine, but at the same time, to minimize the massive interventions and modifications of the original pump. The results obtained with the Hybrid variant in BEP are as follows: In absolute terms, the efficiency was 10 to 11% higher than that of the unmodified Original variant. The flow rate was about 20% higher. This resulted in an even greater increase in overall power output of 37 to 45%. There was also a significant increase in torque of up to 60%. However, the Hybrid variant had, in BEP, significantly lower shaft speed (approximately by 15%) than the Original. On the other hand, it provided a wider control of the flow range ($Q = 0.66 \div 1.1 \cdot Q_{BEP}$), which is advantageous when using PAT as a throttle valve in WDN. In summary, it can be stated that the modifications proposed by the calculation model have a significantly positive effect on increasing the efficiency of PAT operation.

In addition to the modifications described above, another way to increase the efficiency of PAT is to modify the adjacent parts. This mainly concerns a draft tube. Its significance increases as specific speed increases. Further research specifically on high-speed machines will be focused on solving this problem.

Funding: This research has been supported by the IGA 2020:31130/1312/3115 Analysis of liquid flow in hydrodynamic pump and in pump as turbine.

Institutional Review Board Statement: Not applicable.

Informed Consent Statement: Not applicable.

Data Availability Statement: The data presented in this study are openly available at [10.5293/IJFMS.202015.8.3.169].

Conflicts of Interest: The author declares no conflict of interest.

Nomenclature

A	measured value
B	impeller width on inlet, m
BEP	best efficiency point
c	absolute velocity of water, $\mathrm{m \cdot s^{-1}}$
D	impeller diameter, m
FC	frequency converter
FP	feed pump
g	gravitational acceleration, $\mathrm{m \cdot s^{-2}}$
H	net head, m
L	blade length, m
N	rotational speed, $\mathrm{min^{-1}}$
Ns	specific speed, $\mathrm{min^{-1}}$
P	power output, W
PAT	pump as turbine
Q	flow rate, $\mathrm{L \cdot s^{-1}}$
T	torque, N·m
u	circumferential velocity of impeller, $\mathrm{m \cdot s^{-1}}$
w	relative velocity of water, $\mathrm{m \cdot s^{-1}}$
WDN	water distribution network
Y	specific energy, $\mathrm{J \cdot kg^{-1}}$

Subscripts and Superscripts

e	external
i	internal
M	model
T	turbine

u	circumferential component
1	inlet
2	outlet

Greek Symbols

α	angle between circumferential and absolute velocity: deg
β	angle between relative and circumferential velocity, deg
ρ	density of water, $\mathrm{kg{\cdot}m^{-3}}$
η	total efficiency, 1, %

References

1. Thoma, D.; Kittredge, C.P. Centrifugal pumps operated under abnormal conditions. *J. Power Sources* **1931**, *73*, 881–884.
2. Carravetta, A.; Derakhshan, H.S.; Ramos, H.M. Pumps as turbines—Fundamentals and Applications. In *Springer Tracts in Mechanical Engineering*; Springer International Publishing: Cham, Switzerland, 2018; 236p, ISBN 978-3-319-67506-0.
3. Williams, A.A. Pumps as turbines for low cost micro hydro power. *Renew. Energy* **1996**, *9*, 1227–1234. [CrossRef]
4. Venturini, M.; Alvisi, S.; Simani, S.; Manservigi, L. Energy production by means of pumps as turbines in water distribution networks. *Energies* **2017**, *10*, 1666. [CrossRef]
5. Stefanizzi, M.; Capurso, T.; Balacco, G.; Binetti, M.; Torresi, M.; Camporeale, S.M. Pump as turbine for throttling energy recovery in water distribution networks. *AIP Conf. Proc.* **2019**, *2191*, 020142. [CrossRef]
6. Balacco, G. Performance Prediction of a Pump as Turbine: Sensitivity Analysis Based on Artificial Neural Networks and Evolutionary Polynomial Regression. *Energies* **2018**, *11*, 3497. [CrossRef]
7. Stefanizzi, M.; Torresi, M.; Fortunato, B.; Camporeale, S.M. Experimental investigation and performance prediction modeling of a single stage centrifugal pump operating as turbine. *Energy Procedia* **2017**, *126*, 589–596. [CrossRef]
8. Derakhshan, S.; Nourbakhsh, A. Theoretical, numerical and experimental investigation of centrifugal pumps in reverse operation. *Exp. Therm. Fluid Sci.* **2008**, *32*, 1620–1627. [CrossRef]
9. Barbarelli, S.; Amelio, M.; Florio, G. Experimental activity at test rig validating correlations to select pumps running as turbines in microhydro plants. *Energy Convers. Manag.* **2017**, *149*, 781–797. [CrossRef]
10. Kramer, M.; Terheiden, K.; Wieprecht, S. Pumps as turbines for efficient energy recovery in water supply networks. *Renew. Energy* **2018**, *122*, 17–25. [CrossRef]
11. Polák, M. The Influence of Changing Hydropower Potential on Performance Parameters of Pumps in Turbine Mode. *Energies* **2019**, *12*, 2103. [CrossRef]
12. Singh, P. Optimization of the Internal Hydraulics and of System Design for Pumps as Turbines with Field Implementation and Evaluation. Ph.D. Thesis, University of Karlsruhe, Karlsruhe, Germany, 2005.
13. Singh, P.; Nestmann, F. Internal hydraulic analysis of impeller rounding in centrifugal pumps as turbines. *Exp. Therm. Fluid Sci.* **2011**, *35*, 121–134. [CrossRef]
14. Doshi, A.; Channiwala, S.; Singh, P. Inlet impeller rounding in pumps as turbines: An experimental study to investigate the relative effects of blade and shroud rounding. *Exp. Therm. Fluid Sci.* **2017**, *82*, 333–348. [CrossRef]
15. Capurso, T.; Bergamini, L.; Camporeale, S.M.; Fortunato, B.; Torresi, M. CFD analysis of the performance of a novel impeller for a double suction centrifugal pump working as a turbine. In Proceedings of the 12th European Conference on Turbomachinery Fluid dynamics & Thermodynamics ETC13, Lausanne, Switzerland, 8–12 April 2019.
16. Giosio, D.R.; Henderson, A.D.; Walker, J.M.; Brandner, P.A.; Sargison, J.E.; Gautam, P. Design and performance evaluation of a pump-as-turbine micro-hydro test facility with incorporated inlet flow control. *Renew. Energy* **2015**, *78*, 1–6. [CrossRef]
17. Frosina, E.; Buono, D.; Senatore, A. A performance prediction method for pumps as turbines (PAT) using a computational fluid dynamics (CFD) modeling approach. *Energies* **2017**, *10*, 103. [CrossRef]
18. Nechleba, M. *Hydraulic Turbines—Their Design and Equipment*, 2nd ed.; STNL Prague: Prague, Czech Republic, 1962. (In Czech)
19. Gülich, J.F. *Centrifugal Pumps*, 3rd ed.; Springer: Berlin, Germany, 2008; 1116p, ISBN 978-3-642-40113-8.
20. Nielsen, T.K. Simulation model for Francis and reversible pump turbines. *Int. J. Fluid Mach. Syst.* **2015**, *8*, 169–182. [CrossRef]
21. Bednář, J. *Turbines—Small Hydropower Plants*; Marcela Bednářová: Blansko, Czech Republic, 2013; 360p, ISBN 978-80-905437-0-6. (In Czech)
22. Iliev, I.; Trivedi, C.; Dahlhaug, O.G. Simplified hydrodynamic analysis on the general shape of the hill charts of Francis turbines using shroud-streamline modeling. *J. Phys. Conf. Ser.* **2018**, *1042*, 012003. [CrossRef]
23. European Committee for Standardization. *Rotodynamic Pumps—Hydraulic Performance Acceptance Tests—Grades 1, 2 and 3*; ČSN EN ISO 9906; European Committee for Standardization: Brussels, Belgium, 2013. (In Czech)
24. Polák, M. Behaviour of 3D printed impellers in performance tests of hydrodynamic pump. In Proceedings of the 7th International Conference on Trends in Agricultural Engineering, Prague, Czech Republic, 17–20 September 2019; pp. 447–552.

energies

MDPI

Article

Application of CFD to the Design of Manifolds Employed in the Thermodynamic Method to Obtain Efficiency in a Hydraulic Turbine

Erick O. Castañeda Magadán, Gustavo Urquiza Beltrán, Laura L. Castro Gómez * and Juan C. García Castrejón

Centro de Investigación en Ingeniería y Ciencias Aplicadas, Universidad Autónoma del Estado de Morelos, Cuernavaca 62209, Mexico; erick.castanedamag@uaem.edu.mx (E.O.C.M.); gurquiza@uaem.mx (G.U.B.); jcgarcia@uaem.mx (J.C.G.C.)
* Correspondence: lauracg@uaem.mx

Abstract: This study presents the design and implementation of different types of manifolds (sampling system) to measure water flow properties (velocity, pressure, and temperature) through the high- and low-pressure section of a Francis-type low head hydraulic turbine (LHT of 52 m) to calculate it is efficiency using the Thermodynamic Method (TM). The design of the proposed manifolds meets the criteria established in the “International Electrotechnical Commission—60041” Standard for the application of the TM in the turbine. The design of manifolds was coupled to the turbine and tested by the Computational Fluid Dynamics (CFD) application, under the same experimental conditions that were carried out in a power plant, without the need for on-site measurements. CFD analyses were performed at different operating conditions of volumetric flow (between values of 89.67 m^3/s and 35.68 m^3/s) at the inlet of turbine. The mechanical power obtained and the efficiency calculated from the numerical simulations were compared with the experimental measurements by employing the Gibson Method (GM) on the same LTH. The design and testing of manifolds for high- and low-pressure sections in a low head turbine allows for the constant calculation of efficiency, avoiding breaks in the generation of electrical energy, as opposed to other methods, for example, the GM. However, the simulated (TM) and experimental (GM) efficiency curves are similar; therefore, it is proposed that the design of the manifolds is applied in different geometries of low-head turbines.

Keywords: computational fluid dynamics; hydraulic efficiency; Gibson method; manifolds; turbine; thermodynamic method

Citation: Castañeda Magadán, E.O.; Urquiza Beltrán, G.; Castro Gómez, L.L.; García Castrejón, J.C. Application of CFD to the Design of Manifolds Employed in the Thermodynamic Method to Obtain Efficiency in a Hydraulic Turbine. *Energies* **2021**, *14*, 8359. https://doi.org/10.3390/en14248359

Academic Editors: Adam Adamkowski and Anton Bergant

Received: 7 October 2021
Accepted: 7 December 2021
Published: 11 December 2021

1. Introduction

The “International Electrotechnical Commission—60041” (IEC—60041) Standard establishes various test development methods to determine the hydraulic performance of different hydraulic turbomachinery, such as the Reel method, Pitot tubes, and Pressure-Time (also called Gibson), among which is the Thermodynamic Method ™. According to the standard, this method allows, in a hydroelectric power station, for the measurement of flow properties extracted in the high- and low-pressure section (inlet and outlet of the turbine or pump, respectively), to calculate the hydraulic efficiency of the turbomachinery. This method is less invasive compared to others, for example, the Pressure-Time method (also called the Gibson method). The Pressure-Time method is accurate and can inexpensively perform indirect flow measurements for low head turbines. However, it could be risky due to the phenomenon used for measurement. The application of TM instead of the Gibson method aims to avoid damage in any component of the hydraulic turbine, such as the penstock, valves, or distributor. In addition, it allows for the calculation of continuous efficiency by simultaneously measuring the interest variables without stopping power energy generation.

The IEC—60041 Standard establishes that the application of TM is limited to specific hydraulic energy values greater than 1000 J/kg (heads higher than 100 m). However, under favorable conditions, the measurement interval could be extended to lower values of the specific hydraulic energy or heads lower than 100 m [1,2].

Given the inherent difficulties in directly measuring the flow that define the hydraulic efficiency (η_h), it is possible to carry out their extractions in manifolds that are especially designed for the determination of temperature, pressure, and velocity in the fluid, installing them in the inlet and outlet sections of the turbine, respectively (Figure 1).

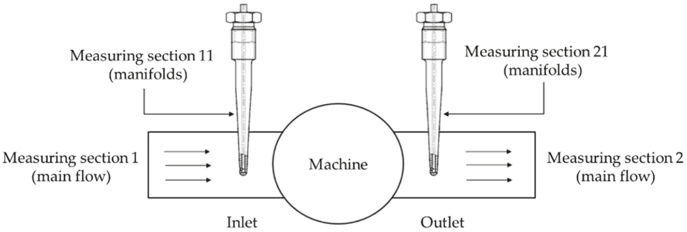

Figure 1. Conceptual diagram showing the location of manifolds to measure flow properties to compute power and efficiency according to IEC—60041.

The manifolds must be designed to ensure that the velocity inside is at a specific interval, so that the flow is uniform when it comes into contact with the installed temperature transducers. This guarantees that the temperature will remain constant inside the manifold and around the sensor. Moreover, the precision and sensitivity of the temperature measurement instruments should be sufficient to provide an indication of a temperature difference of at least 0.001 K between the measurement points. In addition, the temperature of the extracted water should be continuously monitored by thermometers of at least ±0.05 K precision and 0.01 K sensitivity [2]. According to different authors, Pt-100 Resistive Temperature Detectors (RTD's) are commonly used for measurement due to their high stability and precision [3–5].

According to TM, the direct operating procedure or direct method is used to measure the efficiency of the turbine under study. This method measures temperature, velocity, and pressure, extracting water from the penstock at the high-pressure side of the turbine to a manifold with a minimum expansion. Hydraulic losses and friction cause an increase in the temperature of the water passing through the turbine. This phenomenon can be calculated using the specific heat of the water. Although the authors of [6] defined that the decrease in the head in a turbine reduces the temperature difference between the inlet and outlet, they are directly proportional.

On the other hand, although this is a numerical case, in experimental cases, authors such as [4] propose a procedure for the normalization of experimental tests from the opening of the closing control device. After 10 min stabilization in the generator's frequency, the temperature data recording is started by means of Pt-100 type sensors during the first 2 min. At the end, the average value of the temperature difference is calculated (high and low pressure). During this period, the measurements of the other parameters, such as inlet and outlet pressure and power, are simultaneous. This procedure is repeated for different openings of the closing control device, that is, for different load values in the unit, as in the present case.

Hydraulic turbines and the geodesic points where these are installed can present aspects of great complexity, such as installing manifolds on the low-pressure side embedded in concrete tubes. However, with a correct design of collecting tubes that are long enough for sample extraction, the measured temperature values could be considered adequate [7]. In the high-pressure section, the optimal length for penetration of the detraction into the pipe can be calculated. However, the length established by IEC-60041 could be enough [8–11].

IEC-60041 establishes that the design of detraction probes for the high-pressure zone must present the appropriate structural study to avoid total or partial detachment, and that it reaches essential areas such as the runner, causing significant damage. To select the correct materials for the probes that support the loads, the typical properties of the materials used in engineering can be consulted [10,11].

According to [3], the design of a horizontal sampling system at the outlet of the turbine is better than vertical. However, the research is based on a Pelton-type turbine. According to the turbine types, the power distribution and partial flow passage can demonstrate significant differences for the present study.

On the other hand, the system can be designed by two or more means of sampling; for example, a system composed of an arrangement of horizontal tubes with a central mixing chamber, in which the relevant sensors are coupled. Furthermore, perforated tubes are located at the turbine's outlet, and temperature sensor is placed at different heights to measure temperature changes throughout the section.

A hybrid vertical detraction system and a mixing chamber for each tube would reduce the number of sensors required and improve measurement. In addition, the use of perforated tubes for the water samples at the outlet of the turbine omits the presence of elbows to avoid friction losses [12].

The development of accurate instruments allows for the application of TM in low head turbines; for example, most hydroelectric power plants in Mexico have heads lower than 100 m, such as 22 and 76 m. Consequently, the present study focuses on a 52-m head Francis-type hydraulic turbine installed in a hydroelectric plant in México. This has a rotational velocity of 180 RPM (18.84 rad/s) under normal operating conditions, i.e., constant volumetric input flow (between values of 89.67 m^3/s and 35.68 m^3/s), and a 3.5 m maximum tip diameter for the runner.

With these values, the specific speed in the turbine is calculated according to [13–16], see Equation (1). N is expressed in RPM, Q is the volumetric flow in (m^3/s) and H is the head in meters.

$$Ns = N\left(\frac{Q^{0.5}}{H^{0.75}}\right) = \frac{638}{H^{0.512}} \tag{1}$$

The turbines can be classified according to the specific speed, at the head (H), a range from 50 to 240 m can be found the Francis turbine, and their specific speed is between 51 and 255 dimensionless (Power in kW) [16]. Therefore, the specific speed value for the studied turbine is 87.93, i.e., a Francis slow turbine.

On the other hand, an example comparison of the efficiency calculations in a turbine was performed using the Gibson Method (GM) and the TM at the Gråsjø power plant in Norway, which show differences between the efficiency curves below 0.5%, for the entire range measured below 0.15% and for relative powers between 0.5 and 1.15%. The Gråsjø power plant is equipped with a vertical Francis turbine and has a net height of 50 m [17], which serves as a reference for current research development.

2. Materials and Methods

2.1. Measurement System Design

2.1.1. Manifolds Design for the High-Pressure Section (Inlet)

According to Castro [18] and Urquiza [19], the principal parameters were obtained to design the manifolds used in TM on the turbine´s inlet section. The values shown in Table 1 are the final results of the Gibson method, applied on a 52.54 m head turbine under different working conditions. (Q_T) it is the net volumetric flow, (Q_0) is leakage flow when wicked gates are closed, (P_1) is inlet pressure in the flow of water, (P_m) is the mechanical power energy generated by the runner, (P_e) is the electrical power measurement in the generator, (T_{orque}) is the torque generated by the runner, (η_h) is the hydraulic efficiency of the turbine and (η_g) is the efficiency measured in the generator. The number of manifolds and their positioning is shown in Figure 2. The proposed design is shown in Figure 3 [20].

Table 1. Parameters of the turbine on study [18,19].

Q_T (m^3/s)	Q_0 (m^3/s)	P_1 (kPa)	P_m (MW)	P_e (MW)	T_{orque} (kN m)	η_h (%)	η_g (%)
89.67	0.7	390.09	31.65	31.05	1679.94	85.10	98.30
82.00	0.7	392.03	30.71	30.12	1630.04	89.80	98.28
76.14	0.7	393.48	29.03	28.45	1540.87	91.16	98.23
68.73	0.7	395.35	26.05	25.50	1382.70	89.91	98.14
60.99	0.7	396.64	22.63	22.10	1201.17	87.84	97.97
52.90	0.7	397.92	19.02	18.51	1009.55	84.92	97.68
46.11	0.7	399.69	15.72	15.23	834.39	80.08	97.26
35.68	0.7	404.70	10.14	9.68	538.22	65.89	96.06

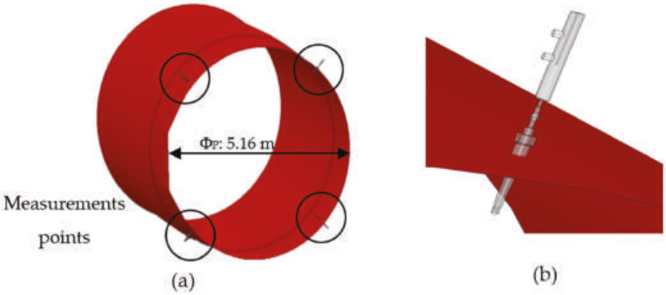

Figure 2. Measurement system, high-pressure section: (**a**) general view, (**b**) upper-right probe and manifold, zoom.

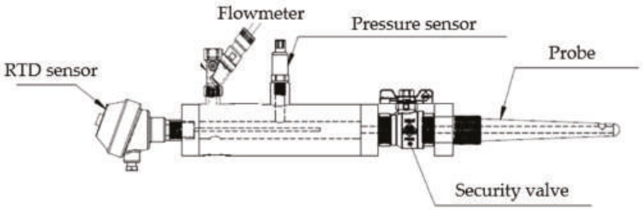

Figure 3. Manifold proposed and instrumentation.

According to [19], for each volumetric flow, the rotational velocity is 180 RPM (18.84 rad/s), and the total deviation of measurements was ±1.6%. It is possible to define the total deviation of measurements of the flow in a systematic way, with Equation (2):

$$\delta_Q = \pm\sqrt{\delta^2_{\Delta\rho} + \delta^2_{\Delta A} + \delta^2_C + \delta^2_\delta + \delta^2_{Dp} + \delta^2_{\Delta pf} + \delta^2_t + \delta^2_{Ql} + \delta^2_{rp}} \tag{2}$$

where:

$\delta_{\Delta\rho}$ —Uncertainty regarding the change in water density due to subsequent pressure change.
$\delta_{\Delta A}$—Uncertainty regarding the change of pipe section due to the change in pressure.
δ_C—Uncertainty regarding the determination of the C-value (C = L/A).
δ_ρ—Uncertainty regarding the value of water density.
$\delta_{\Delta p}$—Uncertainty regarding errors in measuring pressure differences between sections of the pressure pipe.
$\delta_{\Delta pf}$—Uncertainty regarding the decrease in pressure in the section of the pipe that generates hydraulic losses.
δ_t—Error relating to measurement over time.

δ_{QI}—Relative uncertainty of measurement under final conditions by assessing flow intensification (leakage intensification).
δ_{rp}—Error regarding the pressure change log.

The probe intrusion depth in the pressure tube for the extracted water samples is 170 mm, placed diametrically opposite to, or at 90° from, each other. According to Côté [9], the increase in the intrusion length does not represent significant changes between the results obtained with a longer probe (50 mm minimum). The differences between the results obtained with probes of different length were small, and no greater than those obtained with probes of the same length. On the other hand, the intrusion depth of the probe is at an optimum point where the main velocity produces a velocity equal to the average falling velocity of the turbine at the probe inlet. The optimal penetration where this condition is fulfilled is reported for different flow velocity profiles within the penstock [8].

However, the power of the turbine shaft (P_m) or mechanical power has been calculated with Equation (3):

$$P_m = (P_e/\eta_g) - P_f \tag{3}$$

where P_e is the generator active power (measured on site), η_g is the efficiency of the generator (obtained from the manufacturer), and $P_f = (P_{tB} + P_{gB})$ are the losses in the load-bearing block (P_{tB}) and the guide-bearing (P_{gB}). The losses have been calculated in accordance with the IEC 60041 standard.

2.1.2. Manifolds Design for the Low-Pressure Section (Outlet)

For the study of energy transfer in the low-pressure section, the geometry and design parameters were obtained by Castro [18]. The low-pressure section is made up of a rotating domain and a stationary one. The first is made up of the runner, hub and shroud of the turbine; the second is made up of the draft tube, divider and outlet of the section.

According to the standard, the distance of the traction intakes in this section must be located at a distance from the runner of at least five times its maximum diameter; for the turbine in question, the tip diameter of the runner is 3.5 m and the minimum distance required is 17.5 m. However, the manifolds were located farther away than the minimum distanced required to avoid turbulence generated in the walls, close to the division of the draft tube (see Figure 4).

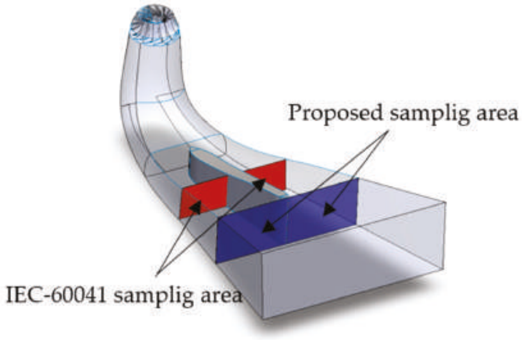

Figure 4. General geometry low section pressure (isometrical view).

Hulaas establishes that, under favorable conditions, the application of TM can be extended to falls of less than 100 m; on the other hand, since it is an inaccessible, closed measurement selection, the only possibility of exploring the temperature is through an intake device located inside the tube. This device consists of at least two tubes that collect partial flows [1,2].

Based on Figure 4, four fluid withdrawal intakes were coupled to perform temperature, flow rate and pressure measurements at the outlet of the draft tube; the proposed design is shown in Figure 5.

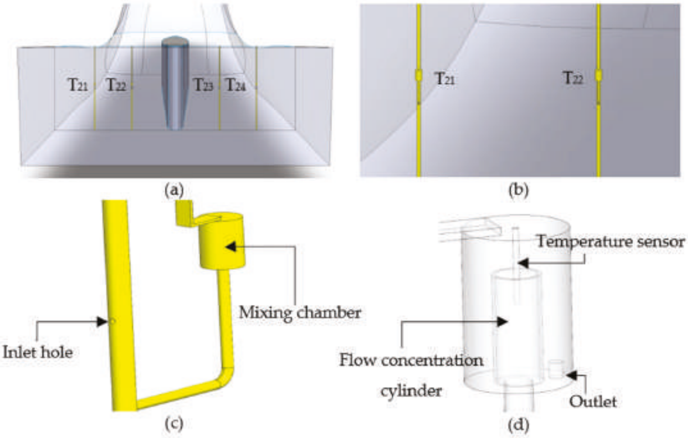

Figure 5. Manifold vessels coupling, outlet section: (**a**) manifolds T_{21}, T_{22}, T_{23} and T_{24}, (**b**) view outlet section left, (**c**) isometric view of manifold vessel, (**d**) mixing chamber (inside).

2.2. Numerical Simulation (CFD)

The computational fluid dynamics (CFD) analysis for the high- and low-pressure sections was performed in commercial software (ANSYS CFX). The domain discretization was performed by ICEM for both domains, and both the numerical calculation, and the post-process were performed by ANSYS CFX.

The discretization of the high-pressure section was of the non-structured tetrahedral type, presenting a total of 1,273,913 elements. In both the high- and low-pressure section, the element unit is millimeters (mm).

For the high-pressure section, the minimum size of the element is 1 mm, and the maximum size is 480 mm. This section includes the temperature sensors, probes, manifolds, inlet, outlet, and penstock.

The discretization for the low-pressure section is also that of the non-structured tetrahedral type, presenting a total of 6,297,796 elements. On the other hand, united with the elements, smaller bodies such as collector tubes (manifolds), mixing chambers, RTD’s, and the flow inlet and outlet locations are added. For the low-pressure section, the minimum size of the element is 1 mm, and the maximum size is 600 mm. This section includes the temperature sensors, manifolds, runner, inlet and outlet of turbine, and draft tube, respectively.

For each of the numerical simulations, mass flow conditions calculated from the inlet volumetric flow were established.

According to [21], some turbulence models, such as k−Epsilon, are only valid for fully developed turbulence, and do not perform well in the area close to the wall. Two ways of dealing with the near-wall region are usually proposed.

One way is to integrate the turbulence with the wall, where turbulence models are modified to enable the viscosity-affected region to be resolved with all the mesh down to the wall, including the viscous sublayer. When using a modified low-Reynolds turbulence model to solve the near-wall region, the first cell center must be placed in the viscous sublayer (preferably $y+ = 1$), leading to the requirement of abundant mesh cells. Thus, substantial computational resources are required.

Another way is to use the so-called wall functions, which can model the near-wall region. When using the wall functions approach, there is no need to resolve the boundary layer, causing a significant reduction in the mesh size and the computational domain. Then:

- First, grid cell need to be 30 < y+ < 300. If this is too low, the model is invalid. If this is too high, the wall is not properly resolved.
- The high-Re model (Standard k−Epsilon, RNG k−epsilon) can be used.
- This method is used when there is greater interest in the mixing than the forces on the wall.

For the present case, the absolute distance from the wall in temperature sensors (walls of greater interest) is 0.97 mm (y), the *Re* number is 3998.2, the skin friction (C_f) is 0.013, the Wall shear stress (τ_w) is 2.44 Pa, the friction velocity (u^*) is 0.049 m/s and the $y+$ value is 47. As the $y+$ value is in the range $30 < y+ < 300$, both the turbulence model k-Epsilon and mesh are applicable for the study.

2.2.1. High Pressure Section

The high-pressure domain (penstock, Figure 6) was established as a stationary numerical analysis, with a k-Epsilon turbulence model and the Total Energy model to obtain temperature changes at strategic points in the domain. The fluid temperature at the inlet was 25 °C, and the walls of the study domain were defined as adiabatic.

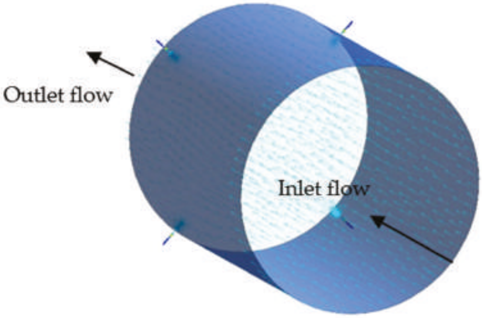

Figure 6. CFD, Post-processing. High-pressure section: Isometric view.

The boundary condition at the input was established as a mass flow rate and the outlet was established as a pressure outlet. Both the inlet and outlet conditions are presented in Table 1; for example, the first simulation is a development to 89,418.9 kg/s (89.67 m^3/s) and 390 kPa values, respectively. A total of 2000 iterations were established, with a convergence criterion of residual type "RMS", with a value of 1×10^{-6} and, for energy, a value of 1×10^{-4}.

The post-processing of the interest variable in the software shows the water temperature inside the manifolds (Figure 7), and the temperature on the surface of the RTD instrument through color contours (Figure 8), in which the higher value corresponds to the red color and the minor to the blue. The RTD sensor, a simulated surface within the study domain, directly obtains the necessary resolution for temperature measurement. The dimensions of the simulated sensor are 4 mm in diameter and 152 mm long [20]. Proper mixing of the fluid is confirmed by means of the temperature contours inside the manifolds, and a constant temperature is ensured. The maximum temperature of the fluid inside the manifolds is 25.1 °C, and the maximum temperature on the surface of the RTD sensor is 25.09 °C.

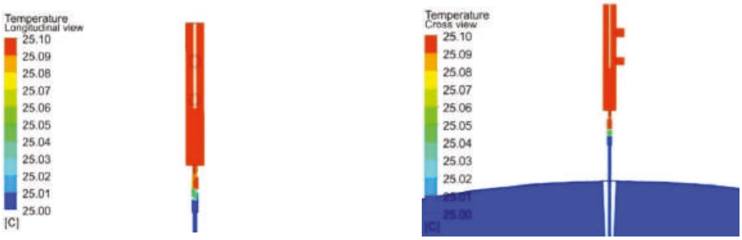

(**a**) (**b**)

Figure 7. Internal temperature vessel, high-pressure section: (**a**) Longitudinal view, (**b**) Cross view.

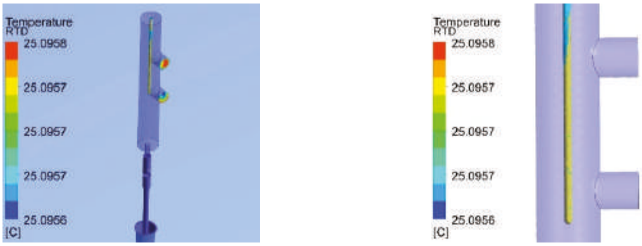

(**a**) (**b**)

Figure 8. RTD temperature, high-pressure section: (**a**) Isometric view, (**b**) Longitudinal view (zoom).

According to the standard, at the manifold outlet, the volumetric flow must be between 0.1×10^{-3} and 0.5×10^{-3} m^3/s; therefore, the expected velocity range will be between 0.29 m/s and 1.46 m/s, respectively, since the outlet diameter of the manifolds is 0.02 m. Figure 9 shows the outlet velocity of the manifolds using colored contours. The obtained results confirm the values that are allowed by the standard.

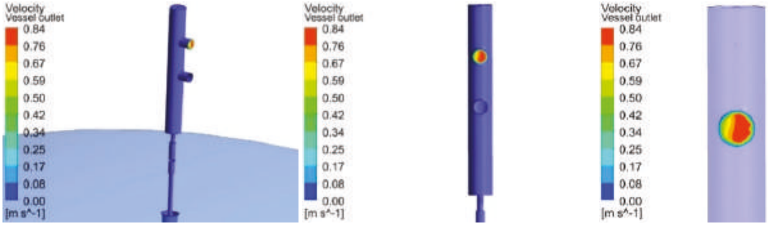

(**a**) (**b**) (**c**)

Figure 9. Velocity outlet, high-pressure section: (**a**) Isometric view, (**b**) Front view, (**c**) location velocity outlet (zoom).

On the other hand, Figure 10 shows the pressure contours at a location where a relevant sensor is physically attached.

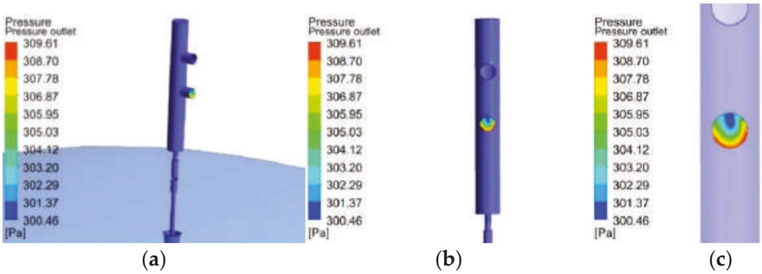

Figure 10. Pressure location, high-pressure section: (**a**) Isometric view, (**b**) Front view, (**c**) location pressure outlet (zoom).

2.2.2. Low Pressure Section

The CFD in the low-pressure section, as well as in the high-pressure one, used different inlet mass flows (presented in Table 1); however, the pressure at the outlet of the turbine (draft tube) was established as a pressure static outlet or open to the atmosphere. The numerical simulation was of the "turbo-machinery" type, defining a rotating domain (runner) and a stationary domain (draft tube and manifolds). When using two types of domains, it is necessary to establish a new boundary condition, defined as an interface. This configures itself as a "stage" type, since it adapts the results of a domain with movement to a stationary one, in which it is determined to be a "fluid–fluid" interface with corresponding 360° angles. A volumetric flow inlet with a direction based on cylindrical components was defined, a rotational velocity of the runner at 180 rpm and the temperature of the inlet fluid was that obtained at the outlet of the penstock for each of the different cases. The k-Epsilon turbulence model and the Total Energy equation were enabled; similarly, the domain walls were adiabatic, as in the penstock. In both the low- and high-pressure section, one of the most prominent turbulence models, the (k-Epsilon) model, was used. This is implemented in most general purpose CFD codes and is considered the industry standard model. It has proven to be stable and numerically robust and has a well-established regime of predictive capability. Therefore, for general-purpose simulations, the model offers a good compromise in terms of accuracy and robustness.

Within CFX, the turbulence model uses the scalable wall-function approach to improve robustness and accuracy when the near-wall mesh is refined. The scalable wall functions enable solutions to arbitrarily fine near-wall grids, significantly improving standard wall functions. Defined thus, a total of 10,000 iterations were established with a convergence criterion of residual type "RMS" with a value of 1×10^{-6} and, for energy, a value of 1×10^{-4}.

The processing of variables of interest in the software shows the temperature measured by the RTD sensor fitted inside the manifold (Figure 11) at the outlet of the draft tube. The dimensions of the simulated sensor are 4 mm in diameter and 50 mm long.

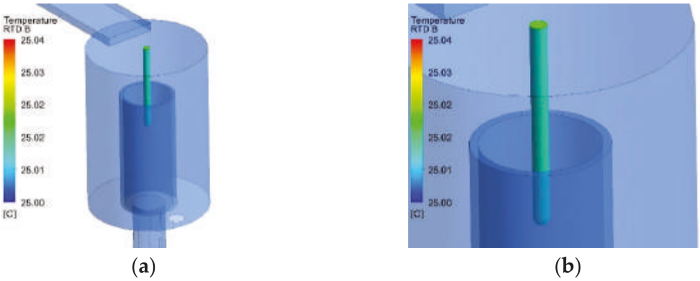

Figure 11. Temperature, low-pressure section: (**a**) Isometric view (**b**) RTD Sensor, zoom.

Figure 12 shows the velocity and pressure at the outlet of the manifold.

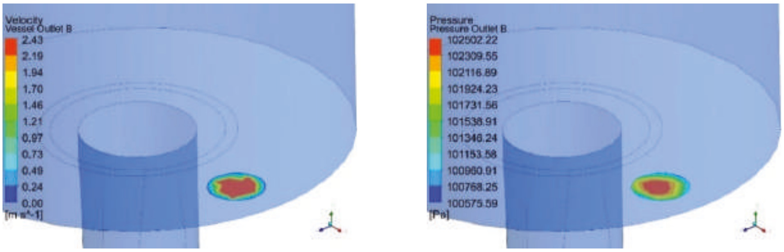

(**a**) (**b**)

Figure 12. Outlet location, (**a**) Velocity outlet, (**b**) Pressure Outlet.

A view of the flow inlet through velocity vectors to the mixing chamber is shown in Figure 13. The total length of the collecting tubes is 4.06 m, equivalent to the outlet height of the draft tube for correct sampling in the zone, the diameter of the tubes is 30.8 mm or 1 1/2 in., 10 inlet holes to the collection tube with a diameter of 10 mm satisfy the minimum dimensions required by the standard [2].

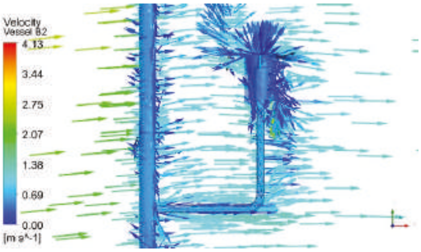

Figure 13. Internal flow (velocity vectors), low-pressure section.

2.3. Application of Grid Convergence Index (GCI)

According to [22], the computer code used for CFD applications must be fully referenced, and previous code verification studies must be briefly described or cited. Appropriate methods could be selected to validate that CFD results do not depend on the quality or size of the grid. For the present study, the Grid Convergence Index (*GCI*) method was used.

The recommended procedure to calculate the fine-grid convergence index (*GCI*) is based on Equation (4)

$$GCI^{21} = (1.25 {e_a}^{21})/({r_{21}}^{p} - 1) \tag{4}$$

where ${e_a}^{21}$ is approximated relative error, calculated by Equation (5). ϕ are the values of critical variables. For the present case, ϕ is the temperature (T_{11} or T_{21}) at specific points in specific domains.

$${e_a}^{21} = |(\Phi_1 - \Phi_2)/\Phi_1| \tag{5}$$

${r_{21}}^{p}$ is the grid refinement factor $r = h_{coarse}/h_{fine}$. It is desirable that this is greater than 1.3. The 21 subscripts correspond to the relationship between grid 1 (fine) and grid 2 (coarse); see Equation (6)

$${r_{21}}^{p} = h_2/h_1 \tag{6}$$

where "p" is the apparent order of the method used. For estimation of discretization error, it is necessary to define a representative cell, mesh or grid size "h" (mm). For example, Equation (7) is employed for three-dimensional calculations.

$$h = \left[\frac{1}{N} * \sum_{i=1}^{N} (\Delta V_i)^{\left(\frac{1}{3}\right)} \right] \tag{7}$$

ΔV_i is the volume and N is the total number of cells used for the computations. Another method to obtain the size of the grid (h) is analyzing the grid in the software used. This analysis can be conducted according to volume, the maximum/minimum length or the maximum/minimum side or the density of the grid.

In comparison with Equation (4), Roache [23] establishes that the grid convergence index (GCI) is based on Equation (8)

$$GCI_{Ro} = 3\,|\,\varepsilon\,|\,/(r^p - 1) \tag{8}$$

where ε is equivalent to ${e_a}^{21}$, and r^p is equivalent to ${r_{21}}^p$. A summary and comparison of results for two grids are shown in Tables 2 and 3.

Table 2. Summary of results, high-pressure section.

Grid	ϕ	${e_a}^{21}$	h	${r_{21}}^p$	GCI^{21} (%)	GCI_{Ro} (%)
Coarse (2)	25.0957	1.20×10^{-6}	455.38	1.196	3.47×10^{-4}	8.34×10^{-4}
Fine (1)	25.0957		380.65			

Table 3. Summary of results, low-pressure section.

Grid	ϕ	${e_a}^{21}$	h	${r_{21}}^p$	GCI^{21} (%)	GCI_{Ro} (%)
Coarse (2)	25.0204	1.22×10^{-5}	816.67	1.917	5.72×10^{-4}	1.37×10^{-3}
Fine (1)	25.0207		426.10			

The grid convergence index (GCI) is adequate when the result is less than 1%, according to Roache. Despite the CGI differences between the authors, a value of less than 1% was obtained for both cases. Due to the presented results, it is possible to carry out the current study with the first generated grid.

2.4. Thermodynamic Method Application

The calculation of Hydraulic Efficiency (η_h) is defined by the ratio of the mechanical power (P_m) and the hydraulic power (P_h) of the turbine, respectively, as in Equation (9).

$$\eta_h = P_m / P_h \tag{9}$$

The mechanical power (P_m) of the turbine is calculated by the specific mechanical energy (E_m), density (ρ) and the volumetric flow (Q_T) that passes through the turbine, as in Equation (10).

$$P_m = E_m * (Q_T * \rho) \tag{10}$$

The hydraulic power (P_h), in contrast with the P_m, is obtained by means of the Specific Hydraulic Energy (E_h), as in Equation (11). The correction factor (ΔP_h) is neglected since Urquiza [8] considered this factor in the presented results.

$$P_h = E_h * (Q_T * \rho) \pm \Delta P_h \tag{11}$$

The E_m was calculated with the variables measured in the manifolds, such as pressure (p), temperature (T) and velocity (v), (see Equation (12)). The reference heights (z) are assigned for each manifold and the isothermal factor ($\dot{a}$), as well as the specific heat (C_p), are obtained from the annexes of IEC 60041, Appendix E physical data, Table EV and EVI [2] (Table 4), and an interpolation of the temperature and average pressure for each of the case studies.

Table 4. Properties of water [2].

	Absolute Pressure (10 × 10^5 Pa)	
θ (°C)	**$\dot{a}$ (×10^{-3} m^3/kg)**	**C_p (J/kg °C)**
23	0.9315	4179
24	0.9286	4179
25	0.9257	4179
26	0.9229	4179
27	0.9201	4179

Finally, gravity (g) was obtained from Reference [8]. The subscripts 11 and 21 correspond to the manifolds in the inlet and outlet section, respectively. Similarly, T_1 and T_2 belong to the corresponding sections.

$$E_m = [\dot{a} * (p_{11} - p_{21})] + [C_p * (T_1 - T_2)] + [({v_{11}}^2 - {v_{21}}^2))/2] + [g * (z_{11} - z_{21})] \quad (12)$$

The E_h is obtained by the properties measured in the main water flow (subscripts 1 and 2), Equation (13). Pressure (p), velocity (v) and height (z) are geodetic sampling points or reference points with respect to the height of the sea level at which the turbine is located. ρ, as well as $\dot{a}$ and C_p, are obtained by interpolation.

$$E_h = [((p_1 - p_2))/\rho] + [(({v_1}^2 - {v_2}^2))/2] + [g * (z_1 - z_2)] \quad (13)$$

The sampling points are observed in Figure 14, which is a general diagram of the turbine in question (original C.H. Temascal plane), as well as the areas in which the fluid properties are measured.

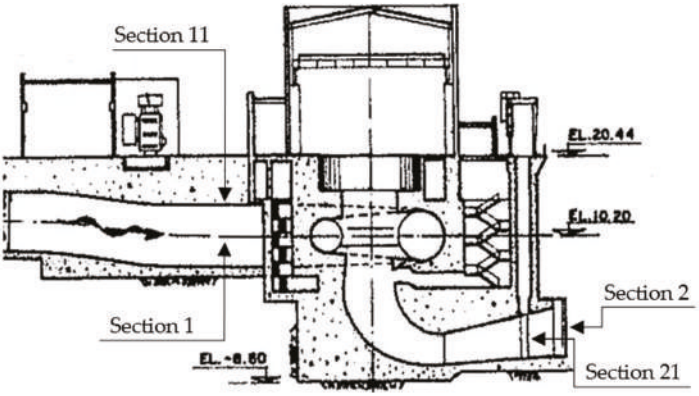

Figure 14. Longitudinal view, measurement points [24].

According to [6], the mechanical energy (E_m) is calculated by Equation (14). In this equation, $\dot{a}$ is an isothermal factor of the water, p_{11}, the inlet pressure in the diffuser, p_{21}, the outlet pressure of the suction tube, T_{11}, the inlet temperature of the suction tube, T_{20}, the outlet temperature of the suction tube aspiration, z_{11}, is a reference point for temperature measurement, and z_{1m} is the reference point for measuring p_{11}.

$$E_m = [\dot{a} * (p_{11} - p_{12})]$$

$$E_m = [C_p * (T_{11} - T_{20})] + [(v_1{}^2 - v_2{}^2))/2] + [g * (z_{1m} - z_{11})] \tag{14}$$

However, the variables for the present study were adapted to the previously established conditions, defining E_m as Equation (15).

$$E_m = [Cp * (T_1 - T_2)] + [(v_{11}{}^2 - v_{21}{}^2))/2] + [g * (z_{11} - z_{21})] \tag{15}$$

3. Results

3.1. Results of Thermodynamic Method

3.1.1. High-Pressure Section

For each of the different conditions and working sections, the temperature, velocity and pressure in the manifolds were obtained as required by IEC 60041. Similarly, the amount of volumetric flow that exits the manifolds located on the penstock and draft pipe was tested. As it is a stationary type of simulation, the value of temperature, pressure and velocity is obtained by exporting a series of values provided by the software in each of the locations of interest at the end of the numerical calculation (high- and low-pressure section). This series of values is averaged and shown below.

Table 5 contains the average temperature values in the four manifolds; Table 6 contains the average velocity and pressure values of the manifolds. Section 14.3.1 "General"; of the IEC-60041 standard establishes that the thermodynamic method for the average yield is based on the laws of thermodynamics, using the thermodynamic temperature ϑ in Kelvin (K). In case of temperature differences, the temperature can be directly expressed in Celsius (°C) degrees, as $\vartheta_1 - \vartheta_2 = \theta_1 - \theta_2$ [2].

Table 5. Manifold´s temperature, high-pressure section.

Q_T (m^3/s)	T_{11} (°C)	T_{12} (°C)	T_{13} (°C)	T_{14} (°C)	T_1 (°C)
89.67	25.095	25.095	25.095	25.095	25.095
82.00	25.095	25.095	25.095	25.095	25.095
76.14	25.095	25.095	25.095	25.095	25.095
68.73	25.096	25.096	25.096	25.096	25.096
60.99	25.096	25.096	25.096	25.096	25.096
52.90	25.096	25.096	25.096	25.096	25.096
46.11	25.096	25.096	25.096	25.096	25.096
35.68	25.097	25.097	25.097	25.097	25.097

Table 6. Manifold's velocity and pressure, high-pressure section.

Q_T (m^3/s)	P_{11} (Pa)	v_{11} (m/s)
89.67	314.22	0.70
82.00	301.12	0.66
76.14	303.74	0.68
68.73	294.34	0.67
60.99	268.95	0.70
52.90	287.85	0.66
46.11	251.58	0.67
35.68	254.11	0.68

3.1.2. Low-Pressure Section

The analysis of results in the low-pressure section (runner and draft tube) involves a comparison of the mechanical power and torque generated by the turbine for each flow condition (Table 7) in the software.

Table 7. Comparison between mechanical power and torque, reported vs. simulated.

Q_T (m^3/s)	$P_{M\ Reported}$ (MW)	$P_{M\ Simulated}$ (MW)	$Torque_{\ Reported}$ (kN m)	$Torque_{\ Simulated}$ (kN m)
89.67	31.65	31.58	1679.94	1676.13
82.00	30.71	30.66	1630.04	1627.58
76.14	29.03	28.96	1540.87	1537.15
68.73	26.05	25.99	1382.70	1379.33
60.99	22.63	22.58	1201.17	1198.73
52.90	19.02	18.97	1009.55	1006.96
46.11	15.72	15.67	834.39	831.56
35.68	10.14	10.12	538.22	537.32

By demonstrating the same mechanical power and torque conditions, the results in the draft tube can be analyzed. The manifolds attached to the draft tube acquired samples of the main flow (water) to obtain the energy distribution at different points. Variables such as temperature, velocity and pressure, obtained in each of the containers, are shown in Tables 8 and 9.

Table 8. Manifold´s temperature, low-pressure section.

Q_T (m^3/s)	T_{21} (°C)	T_{22} (°C)	T_{23} (°C)	T_{24} (°C)	T_2 (°C)
89.67	25.023	25.017	25.019	25.022	25.020
82.00	25.018	25.014	25.011	25.013	25.014
76.14	25.012	25.011	25.008	25.009	25.010
68.73	25.008	25.008	25.008	25.007	25.008
60.99	25.008	25.010	25.007	25.007	25.008
52.90	25.009	25.011	25.009	25.008	25.010
46.11	25.013	25.014	25.012	25.011	25.013
35.68	25.020	25.021	25.018	25.017	25.019

Table 9. Manifold´s velocity and pressure, low-pressure section.

Q_T (m^3/s)	P_{21} (Pa)	v_{21} (m/s)
89.67	99,385.15	1.31
82.00	99,503.34	1.25
76.14	99,843.35	1.15
68.73	100,511.12	0.89
60.99	100,265.66	1.02
52.90	99,748.05	0.98
46.11	99,441.40	0.94

4. Discussion

The results obtained in the low-pressure section (draft tube) show that the direction of runner rotation (clockwise) and the geometry of the draft tube discharges water from a turbine, in addition to acting as an energy-recovery device, helping to improve the overall performance of the unit. It can also allow the downstream water level to be lower or higher than the equatorial plane of the turbine, depending on the needs of the facility. The draft tube, due to its divergent shape, causes a deceleration in the velocity of the water leaving the turbine, converting the kinetic energy of the fluid into pressure energy (Figure 15) [18].

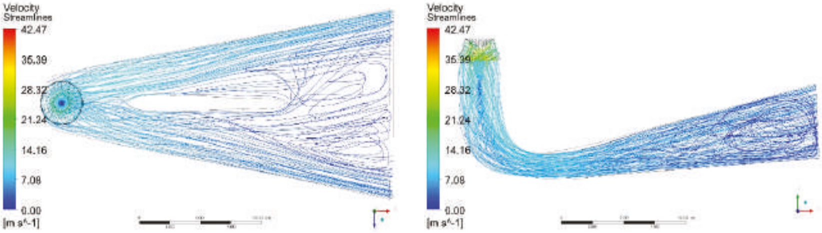

(**a**) (**b**)

Figure 15. Velocity streamlines on the complete turbine, (**a**) upper view, (**b**) lateral View.

By coupling the manifolds in the draft tube, the flow distribution is affected, causing recirculation or vorticity in the area in which manifolds are located. The location of the manifolds is suggested by IEC-60041. Depending on the dimensions of probes, vorticity can be created behind the probes and then dissipated. The flow disturbance will be downstream once velocity, pressure, and temperature variables have been measured, so they cannot influence efficiency calculations. Therefore, the average temperatures in the manifolds T_{22} and T_{23} are slightly higher than the average temperature of T_{21} and T_{24}, as derived from the flow distribution behavior in the turbine (Figure 16).

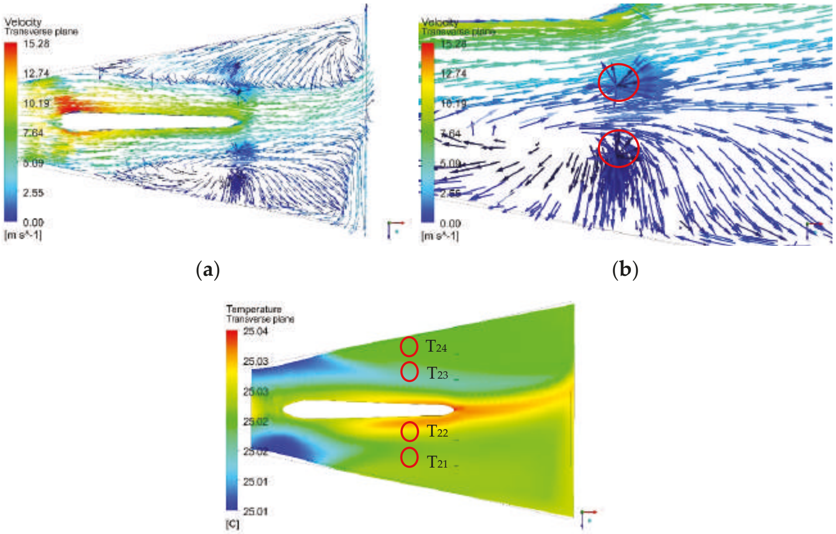

(**a**) (**b**)

(**c**)

Figure 16. Manifold´s in the draft tube, (**a**) Recirculation flow (normalized symbols), (**b**) Recirculation flow in manifolds, left section "zoom" (normalized symbols) (**c**) Temperature contour.

The summary of results obtained from the temperature differences T_1–T_2 (ΔT), E_m, E_h, P_m, P_h and η_h, for different cases is presented in Table 10. Figures 17 and 18 show the main comparison of the results, between what was reported in [18,24] and the current case study.

Table 10. Summary of results, application of Thermodynamic Method.

Q_T (m^3/s)	ΔT (°C) [1]	E_m (J/kg)	E_h (J/kg)	P_m (MW)	P_h (MW)	η_h (%)
89.67	0.075	336.04	420.12	30.05	37.57	79.99
82.00	0.081	363.26	420.26	29.71	34.37	86.44
76.14	0.085	379.30	421.10	28.80	31.98	90.07
68.73	0.087	389.71	423.14	26.71	29.01	92.10
60.99	0.087	388.17	424.21	23.61	25.80	91.50
52.90	0.086	383.80	424.16	20.25	22.38	90.48
46.11	0.083	370.69	425.20	17.05	19.55	87.18
35.68	0.077	347.91	429.30	12.38	15.28	81.04

[1] ΔT: Temperature difference between measured sections (T_1–T_2).

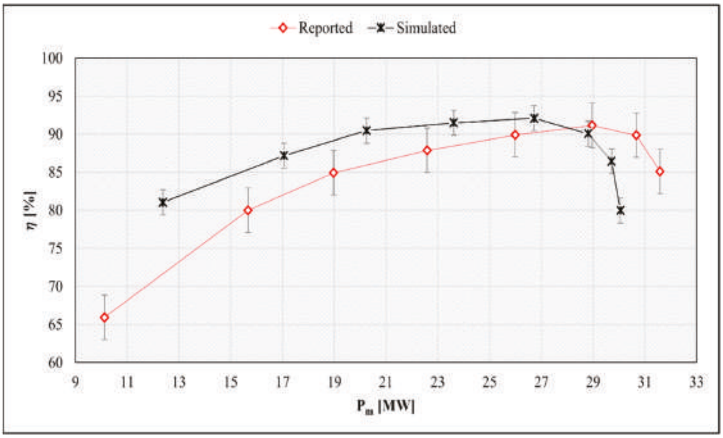

Figure 17. Comparison, Reported hydraulic efficiency (Gibson method) vs. Simulated hydraulic efficiency.

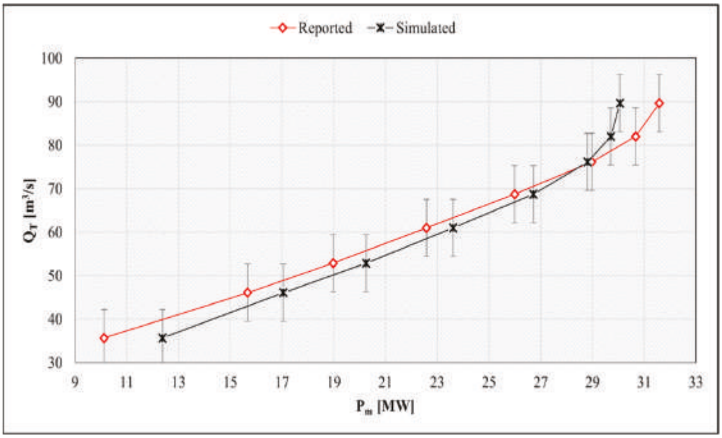

Figure 18. Comparison of mechanical power generated, reported (Gibson method) vs. simulated.

CFD simulations are a proven tool to investigate hydraulic turbine performance, while measurements of some parameters, such as flow or pressure, are common in calculations of their efficiency. In the present study, the design of manifolds and CFD applications contribute to the assay, with sampling system (manifolds) and experimental measurement times in the power plant, complying with the criteria established to apply the TM to low-load turbines.

Experimental studies report that the water temperature at the turbomachine outlet must be higher than that at the inlet. With a lower temperature difference between the measurement sections, the maximum hydraulic efficiency is presented. According to those mentioned above [3], the difference between the efficiency curves is around 0.5%; however, for the present study, the maximum and minimum differences in efficiency are 15.12% and 1.09%, respectively, for the Gibson method (reported). As one of the most important variables for the study is the temperature on surfaces of principal components, such as the runner, penstock, draft tube, etc., and these are unknown, the domain was specified as adiabatic. As a result, there is a low-temperature increase in the water between the high- and low-pressure sections. These cause a low-energy exchange and higher efficiency than expected. If the temperature in these components was known, the boundary conditions could be set differently, and a lower efficiency would be expected in different cases. Likewise, the efficiency would present results closer to those reported. The hydraulic efficiency of the turbine is susceptible to temperature changes between one section and another. This sensitivity is presented with values up to 0.0001 K; the assumed temperature, or a change in temperature in any of the components, has a direct effect on efficiency.

The simulated TM presented differences in the mechanical power and efficiency; however, the behavior of the generated curve shows the same tendency as the curve in the experimental data obtained using the Gibson method (reported), presenting a gradual increase in efficiency until a maximum point is reached. This subsequently decreases. The results obtained for each operating condition are similar to those reported by the Gibson method, meaning an adequate comparison for the study of the proposed manifolds design, considering the head limits (less than 100 m), the amount of maximum volumetric input flow (89.67 m^3/s), the type of turbine (Francis slow) and the specific speed of the turbomachine (less than 110). In future studies, the authors recommend developing transitory simulations for other operating conditions, as well as using the experimental test to measure temperature in the main components, and set different variables in the numerical simulations.

According to [3,12], the present study used a hybrid vertical detraction system and a mixing chamber for each tube, reducing the number of sensors that are required to facilitate installation in the low-pressure section. In addition, the manifolds proposed in the low-pressure section are compatible at different outlet heights for the draft tube, as it is only necessary to adjust the tube length.

5. Conclusions

Based on the location of the manifolds in the input and output sections, the proposed design of manifolds to measure properties of the main flow of a Francis-type low-head hydraulic turbine meet with the requirements suggested by the IEC—60041 Standard to carry out the Thermodynamic Method (TM) employing Computational Fluid Dynamics (CFD).

The distance from the turbine center to the measuring section is essential. The minimum distance set in the standard [2] is five times its maximum diameter, and the measurements show that it should be the absolute minimum. According to Figure 3, a shorter distance could improve energy distribution.

Using a mixing chamber inside the draft tube allows for a direct measurement of temperature in the principal flow at the outlet. In addition, inside the mixing chamber, there is a water flow concentrator, which helps to direct the flow into the temperature sensor, obtaining a direct measurement. The IEC-60041 establishes that the minimum number of tubes consists of two units that collect partial flows. However, increasing the number of tubes and manifolds at the outlet makes it possible to improve the temperature measurements. In this case, four manifolds were used in the low-pressure section. In both the left and right section, two manifolds were installed after the division to avoid a high recirculation or vorticity in the area in which manifolds are located.

On the other hand, the results obtained from the mechanical power and torque in the turbine runner were identical to those reported by the Gibson method (GM); however, the efficiency between the above methods is similar. To obtain results that are closer to reality, the numerical simulations used in CFD must be supplied from as many boundary conditions as possible (actual conditions). It is necessary to set the temperature on the surface of principal components so that the main flow of water makes contact via its passage through the turbomachine to the efficiency results, with the application of TM.

The efficiency calculation is higher under particular volumetric flow conditions (35.68 m^3/s and 68.73 m^3/s) compared to the efficiency reported when applying the GM. The maximum efficiency generated by the turbine applying the TM was 92.10%, corresponding to a flow of 68.73 m^3/s. After the maximum efficiency point, the TM's efficiency is lower than the GM's.

Author Contributions: Conceptualization: L.L.C.G.; Investigation: E.O.C.M. and L.L.C.G.; Methodology: L.L.C.G.; Project administration: G.U.B.; Resources: G.U.B.; Software: L.L.C.G.; Supervision: G.U.B.; Writing—original draft preparation: E.O.C.M.; Writing—review & editing: L.L.C.G. and J.C.G.C. All authors have read and agreed to the published version of the manuscript.

Funding: This work is partly supported by the National Council for Science and Technology [Conacyt], CVU Number: 707755.

Acknowledgments: To Arturo Nava Torres, for his unconditional collaboration in the presented project. To the "Centro de Investigación en Ingeniería y Ciencias Aplicadas (CIICAp)", for all facilities provided during my stay.

Conflicts of Interest: The authors declare no conflict of interest.

Glossary

$\dot{a}$	Isothermal factor of water (m^3/kg)
C_p	Specific heat capacity of water (J/kg °C)
E_h	Specific hydraulic energy (J/kg)
E_m	Specific mechanical energy (J/kg)
g	gravity acceleration (m/s^2)
p_1	Turbine pressure inlet (Pa)
p_{11}	Average pressure vessels, high-pressure section (Pa)
p_2	Turbine pressure outlet (Pa)
p_{21}	Average pressure vessels, low-pressure section (Pa)
P_e	Active generator power (MW)
P_f	Difference in losses in the bearings (%)
P_{gB}	Loss in guide bearing (%)
P_h	Hydraulic power (MW)
P_m	Mechanical power (MW)
P_{tB}	Loss in load bearing (%)
Q_0	Leakage flow (m^3/s)
Q_T	Volumetric flow in turbine (m^3/s)
T_1	Average temperature vessels, high-pressure section (°C)
T_{11}	Temperature, upper-right vessel (°C)
T_{12}	Temperature, upper-left vessel (°C)
T_{13}	Temperature, lower-right vessel (°C)
T_{14}	Temperature, lower-right vessel (°C)
T_2	Average temperature vessels, low-pressure section (°C)
T_{21}	Temperature vessel A (°C)
T_{22}	Temperature vessel B (°C)
T_{23}	Temperature vessel C (°C)
T_{24}	Temperature vessel D (°C)
v_1	Turbine velocity inlet (m/s)

v_{11}	Average velocity vessels, high-pressure section (m/s)
v_2	Turbine velocity outlet (m/s)
v_{21}	Average velocity vessels, low-pressure section (m/s)
z_1	Reference point high-pressure section (m)
z_{11}	Reference point in manifolds, high-pressure section (m)
z_2	Reference point low-pressure section (m)
z_{21}	Reference point in manifolds, low-pressure section (m)
ΔP_h	Hydraulic power correction (W)
θ	Temperature (°C)
Φ_P	Penstock diameter
δ_C	Uncertainty regarding the determination of the C-value (C = L/A) (%)
δ_{Ql}	Relative uncertainty of measurement under final conditions by assessing flow intensification (leakage intensification) (%)
δ_Q	Total deviation of measurements of the flow in a systematic manner (%)
δ_{rp}	Error regarding the pressure change log (%)
δ_t	Error relating to measurement over time (%)
$\delta_{\Delta A}$	Uncertainty regarding the change in pipe section due to the change in pressure (%)
$\delta_{\Delta p}$	Uncertainty regarding errors in measuring pressure differences between sections of the pressure pipe (%)
$\delta_{\Delta pf}$	Uncertainty regarding the decrease in pressure in the section of the pipe that generates hydraulic losses (%)
$\delta_{\Delta \rho}$	Uncertainty regarding the change in water density due to subsequent pressure change (%)
δ_ρ	Uncertainty regarding the value of water density (%)
η_g	Generator efficiency (%)
η_h	Hydraulic efficiency (%)
ρ	Density (kg/m^3)

References

1. Hulaas, H.; Vinnogg, L. Field acceptance tests to determine the hydraulic performance of hydraulic turbines, storage pumps and pump-turbines. Clause 14 Thermodynamic method for measuring efficiency, comments. In Proceedings of the International Group for Hydraulic Efficiency Measurements 2010, Roorkee, India, 21–23 October 2010.
2. International Electrotechnical Commission 60041 (IEC 60041). Thermodynamic method for measuring efficiency. In *Field Acceptance Tests to Determine the Hydraulic Performance of Hydraulic Turbines, Storage Pumps and Pump-Turbines*, 3rd ed.; International Electrotechnical Commission: Geneva, Switzerland, 1991; pp. 293–319.
3. Hulaas, H.; Nilsen, E.; Vinnogg, L. Thermodynamic efficiency measurements of Pelton turbines. Experience from investigation of energy/Temperature distribution in the discharge canal measuring section. In Proceedings of the 7th International Conference on Hydraulic Efficiency Measurements, Milan, Italy, 3–6 September 2008; p. 11.
4. Patil, S.; Verma, H.; Kumar, A. Efficiency measurement of hydro machine by Thermodynamic method. In Proceedings of the 8th International Conference on Hydraulic Efficiency Measurements, Roorkee, India, 21–23 October 2010.
5. Shang, D. Application research on testing efficiency of main drainage pump in coal mine using thermodynamic theories. *Int. J. Rotating Mach.* **2017**, *2017*, 5936506. [CrossRef]
6. Kahraman, G.; Lütfi, Y.H.; Hakan, F.Ö. Evaluation of energy efficiency using thermodynamics analysis in a hydropower plant: A case study. *Renew. Energy* **2009**, *34*, 1458–1465. [CrossRef]
7. Feng, X.; Hequet, T.; Muciaccia, F. Efficiency testing in Tai An (Shandong China) PSPP reversible units by means of thermodynamic method. In Proceedings of the International Group for Hydraulic Efficiency Measurements 2008, Milano, Italy, 3–6 September 2008.
8. Karlicek, R.F. Analysis of uncertainties in the Thermodynamic Method of testing hydraulic turbines. In Proceedings of the IGHEM Seminar, Reno, NV, USA, 28–31 July 1998.
9. Côté, E.; Proulx, G. Experiments with the thermodynamic method. In Proceedings of the International Group for Hydraulic Efficiency Measurements 2012, Trondheim, Norway, 28 June 2012.
10. Gere, J.M.; Goodno, B.J. *Mechanics of Materials*; Cengage: Boston, MA, USA, 2009.
11. Beer, F.; Russell, E.; DeWolf, J.; Mazurek, D. *Mechanics of Materials*; McGraw-Hill Education: New York, NY, USA, 2010.
12. Mangla, M.; Khodre, N. Measurement of turbine efficiency by thermodynamic Method for field acceptance test of hydro turbine and Comparison with model test result. In Proceedings of the International Group for Hydraulic Efficiency Measurements 2010, Roorkee, India, 21–23 October 2010.
13. Lugaresi, A.; Massa, A. Designing Francis turbines: Trends in the last decade. *Water Power Dam Constr.* **1987**, *39*, 23–32.
14. Islam, R.J.; Siam, I.R.; Hasan, R.; Hasan, S.; Islam, F. A Comprehensive Study of Micro-Hydropower Plant and Its Potential in Bangladesh. *Int. Sch. Res. Netw.* **2012**, *2012*, 635396.
15. Hatata, A.Y.; El-Saadawi, M.M.; Saad, S. A feasibility study of small hydro power for selected locations in Egypt. *Energy Strategy Rev.* **2019**, *24*, 300–313. [CrossRef]

16. Prawin, A.M.; Jawahar, C.P. Design of 15 kW Micro Hydro Power Plant for Rural Electrification at Valara. In Proceedings of the 1st International Conference on Power Engineering, Computing and CONtrol, PECCON-2017, Tamil Nadu, India, 2–4 March 2017.
17. Ole, G.D.; Torbjørn, K.N.; Brandåstrø, B.; Håkon, H.F.; Wiborg, E.J.; Hulaas, H. Comparison between pressure-time and thermodynamic efficiency measurements on a low head turbine. In Proceedings of the 6th International Conference on Innovation in Hydraulic Efficiency Measurements, Portland, OR, USA, 30 July–1 August 2006.
18. Castro, L.; Urquiza, G.; Adamkowski, A.; Reggio, M. Experimental and numerical simulations predictions comparison of power and efficiency in hydraulic turbine. *Model. Simul. Eng.* **2011**, *2011*, 146054. [CrossRef]
19. Castañeda, M.E.O.; Castro, G.L.L.; Urquiza, B.G.; Alcántara, M.J. Diseño de un recipiente colector para medición de eficiencia teórica en turbinas hidráulicas. In Proceedings of the SOMIM Conference, Sinaloa, Mexico, 18–20 September 2019.
20. Urquiza, B.G.; Kubiak, S.; Adamkowski, A.; Janicki, W. Condiciones Previas para la Medición de Flujo y Cálculo de Eficiencia de la Unidad No. 4 en la C. H. Temascal, Tech. Rep. 76P/DM/CIICAp. 2005.
21. Lecture 7: Turbulence Modeling Introduction to ANSYS Fluent, Sales Conference Theme and Team Building. Available online: https://www.academia.edu/36090206/Lecture_7_Turbulence_Modeling_Introduction_to_ANSYS_Fluent (accessed on 5 December 2021).
22. Celik, B.I.; Ghia, U.; Roache, P.J.; Freitas, C.J.; Coleman, H.; Raad, P.E. Procedure for estimation and reporting of uncertainty due to discretization in CFD applications. *J. Fluids Eng. Trans. ASME* **2008**, *1*, 130.
23. Roache, P.J. Perspective: A method for uniform reporting of grid refinement studies. *J. Fluids Eng.* **1994**, *116*, 405–413. [CrossRef]
24. Urquiza, B.G.; Kubiak, S.; Adamkowski, A.; Janicki, W. Resultados de Medición de Flujo y Cálculo de Eficiencia de la Unidad No. 4 en la C. H. Temascal, Tech. Rep. 77P/DM/CIICAp. 2005.

energies

MDPI

Article

Mechanistic Model of an Air Cushion Surge Tank for Hydro Power Plants

Madhusudhan Pandey [1], Dietmar Winkler [1], Kaspar Vereide [2], Roshan Sharma [1] and Bernt Lie [1,*]

[1] Telemark Modeling and Control Center (TMCC), University of South-Eastern Norway (USN), 3918 Porsgrunn, Norway; madhusudhan.pandey@usn.no (M.P.); dietmar.winkler@usn.no (D.W.); roshan.sharma@usn.no (R.S.)
[2] Department of Civil and Environmental Engineering, Norwegian University of Science and Technology, 7034 Trondheim, Norway; kaspar.vereide@ntnu.no
* Correspondence: bernt.lie@usn.no

Abstract: Due to the increasing use of renewable energy sources, and to counter the effects of fossil fuels, renewable dispatchable hydro power can be used for balancing load and generation from intermittent sources (solar and wind). During higher percentage change in load acceptance or rejection in the intermittent grid, the operations of surge tanks are crucial in terms of water mass oscillation and water hammer pressure, and to avoid wear and tear in actuators and other equipment, such as hydro turbines. Surge tanks are broadly classified as open types, with access to open air, and closed types, with a closed volume of pressurized air. Closed surge tanks are considered to have a more flexible operation in terms of suppressing water mass oscillation and water hammer pressure. In this paper, a mechanistic model of an air cushion surge tank (ACST) for hydro power plants is developed based on the ordinary differential equations (ODEs) for mass and momentum balances. The developed mechanistic model of the ACST is a feature extension to an existing open-source hydro power library—OpenHPL. The developed model is validated with experimental data from the Torpa hydro power plant (HPP) in Norway. Results show that the air friction inside the ACST is negligible as compared to the water friction. The results also indicate that a hydro power plant with an ACST is a potential candidate as a flexible hydro power in an interconnected power system grid supplied with intermittent energy sources. Conclusions are drawn based on the simulation results from hydraulic performance of the ACST.

Keywords: air cushion surge tank (ACST); air friction model; flexible hydro power plants; mechanistic model; OpenHPL

Citation: Pandey, M.; Winkler, D.; Vereide, K.; Sharma, R.; Lie, B. Mechanistic Model of an Air Cushion Surge Tank for Hydro Power Plants. *Energies* **2022**, *15*, 2824. https://doi.org/10.3390/en15082824

Academic Editors: Adam Adamkowski and Anton Bergant

Received: 17 March 2022
Accepted: 11 April 2022
Published: 13 April 2022

1. Introduction

1.1. Background

Electricity generation from renewable energy is increasing because of oil insecurity, climatic concern, the nuclear power debate, and carbon emission prices. In a growing trend of renewable energy, today's power systems are a combination of intermittent and dispatchable renewable sources in a common interconnected grid. Intermittent sources include sources like solar power plants and wind power plants, whose variability can be balanced using a dispatchable renewable source like a hydro power plant, as discussed in [1,2]. In an interconnected power grid with both intermittent and dispatchable sources, a sudden loss in generation from the intermittent sources, for example, shadowing a large number of solar panels as in the case of solar power plants, a shutdown of the wind generators for unacceptable wind velocity as in the case of wind power plants, hydro power plants must be able to operate with a higher percentage of load acceptance to cope with the loss in generation, and to protect the power grid from a blackout. Similarly, when there is a sudden increase in production from the intermittent generation, hydro power plants must be able to operate with a higher percentage of load rejection to cope with grid instability and blackout. This indicates the need for flexible operation of dispatchable hydro power plants. In [3,4], the concept of *flexible hydro power* is coined for the interconnected power grid. Similarly, in [5] cascaded hydro power plants are considered as one of the candidates for flexible hydro power plants. In relation to the concept of flexible hydro power, hydro power plants with open surge tanks are relatively less able to tackle a higher percentage of load acceptance and rejection. However, power plants with ACST are more likely to tackle a higher percentage of load acceptance and rejection as ACST can be placed very near to the turbine. Hydraulic behavior of the open surge tanks studied in [6] outlines their operational limits in terms of their design heights and water hammer effects. As the percentage of load acceptance and rejection increases in the case of the open surge tanks, water mass oscillation inside the surge tanks may exceed the maximum allowed height and the operational limit of the power plant equipment due to an excessive water hammer effect. Similarly, in [7,8] the benefits of ACST with respect to open surge tanks are given.

In this regard, it is of interest to study the hydraulic behavior of an ACST (closed surge tank) with respect to open surge tanks. A simple mechanistic model of an ACST was developed and studied previously in [9] as a feature extension to an open-source hydro power library—OpenHPL. OpenHPL is based on an equation-based language—Modelica. OpenHPL is under development at the University of South-Eastern Norway. This paper primarily focuses on the model improvements from [9], validation of the improved model with experimental data from [10], and hydraulic behavior of an ACST in relation to flexible hydro power plants.

1.2. Previous Work and Contributions

The model of hydraulic transients inside the surge tank is a well-established theory using Newton's second law [11,12]. The use of hydraulic resistances in the inlet of the surge tank helps to reduce water hammer effects. Different types of surge tanks designed with respect to the hydraulic resistances are presented in [13]. The time evolution equations for developing a mechanistic model of the surge tank are given in [14]. The hydraulic resistance at the inlet of different kinds of surge tanks can be studied from [14,15]. Closed surge tanks or ACST are important in terms of suppressing water mass oscillation due to the cushioning of air during hydraulic transients [16]. A hydraulic scale model of an ACST was studied in [10] based on 1D mass and momentum balances. In [17], a simulation study was carried out considering 1D mass and momentum equations for both water and air inside the ACST. In the paper, it is shown that the mass and momentum balances for air inside the ACST can be further simplified with an ideal gas relation. Other studies include the gas seepage theory for air loss through the ACST chamber in [18], a monitoring method for the hydraulic behavior of the ACST in [19], stability analysis of the ACST in [20], etc. The model developed in most of the previous work assumes an adiabatic process for the cushioning of air inside the ACST. The polytropic constant for air γ is considered around 1.4 for almost all the models of the ACST. However, previous work lacks modeling of the ACST with a possible consideration of friction due to air flow inside the ACST during its operation. The following research contributions are provided in this paper:

- a mechanistic model of an ACST, and
- a comparison between the ACST models with and without air friction.

1.3. Outline

Section 2 provides a mechanistic model of an ACST based on mass and momentum balances. In Section 3, model fitting and simulation results are outlined through a case study of the ACST used in Torpa Hydro Power Plant (HPP). Section 4 provides conclusions and future work.

2. Mechanistic Model of ACST

A general schematic and a flow diagram of an ACST is shown in Figure 1. The free water surface inside the surge tank is filled with pressurized air. Figure 1a shows the general schematic of an ACST where the water with volumetric flow rate $\dot{V}$ flows towards the air chamber through the access tunnel with length L_t and diameter D_t. The intake-penstock manifold pressure at the bottom of the tank is represented by p_m, and the air pressure at the air chamber due to the cushioning of the air is represented by p_c. The diameter of the air chamber is D. H is the total height of the surge tank and L is the total vertical slant length of the surge tank. In the figure, h represents the water level inside the tank during the operation of the ACST, and the dotted line in Figure 1a indicates that h is a variable quantity. Figure 1b shows a flow diagram inside the surge tank where F_f is the fluid friction against $\dot{V}$, F_g is the force due to gravity in the downward direction, and $F_\mathrm{g}^{\dot{V}}$ is the projection of F_g in the alignment of the flow.

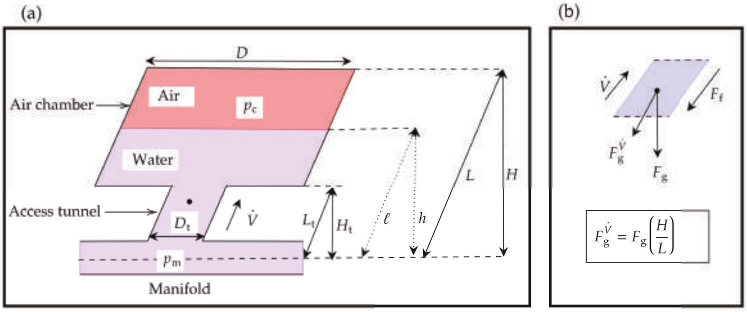

Figure 1. ACST with an access tunnel and an air chamber. (**a**) general schematic of ACST and (**b**) flow diagram.

Models developed in OpenHPL are based on a semi-explicit DAE formulation with a differential equation for the mass and the momentum balances as described in [21] and given by

$$\frac{dm}{dt} = \dot{m} \tag{1}$$

$$\frac{d\mathcal{M}}{dt} = \dot{\mathcal{M}} + F \tag{2}$$

where $\dot{m}$ and $\dot{\mathcal{M}}$ represent the mass flow rate and the momentum flow rate, respectively.

Equations (1) and (2) are expressed with a series of algebraic equations as

$$\dot{m} = \rho\dot{V} \tag{3}$$

$$\mathcal{M} = mv \tag{4}$$

$$\dot{\mathcal{M}} = \dot{m}v \tag{5}$$

$$F = F_\mathrm{p} - F_\mathrm{g}^{\dot{V}} - F_\mathrm{f} \tag{6}$$

where ρ is the density of the water, m is the mass of air and water inside the ACST, v is the average velocity of the flow, V is the volume of the ACST, F is the total force acting in the surge tank, F_p is the pressure force, and F_f is the fluid frictional force. The expressions for all the variables are given in the sequel. A general idea regarding mathematical formulations of these variables is taken from [9].

The total mass inside the surge tank is expressed as

$$m = m_\mathrm{w} + m_\mathrm{a} \tag{7}$$

where m_w and m_a are the masses of the water and the air inside the surge tank, respectively. m_a is constant inside the chamber and is determined based on the initial air cushion pressure p_c0 which is considered to be a design parameter for the hydraulic performance of the surge tank. If h_{c0} is the initial water level inside the surge tank for the initial air cushion pressure p_{c0}, then the expression for the mass of the air inside the surge tank is found from an adiabatic compression and rarefaction of the air inside the surge tank during operation. It is found that for an ACST with a larger diameter, the heat transfer between air and water, air to the walls of the ACST, etc., can be neglected, and an adiabatic process of compression and rarefaction of the air inside the ACST can be assumed [16]. For an adiabatic process with pressure p, volume V, and γ of the air inside the ACST, considering standard temperature and pressure (STP), the relation $pV^\gamma =$ constant is assumed where γ is the ratio of specific heats at constant pressure and at constant volume. The mass of the air is then calculated formulating an ideal gas relation with the initial air pressure p_{c0} and the initial volume $A\left(L - h_{c0}\frac{L}{H}\right)$ given by

$$m_a = \frac{p_{c0} A \left(L - h_{c0}\frac{L}{H}\right) M_a}{RT^\circ} \tag{8}$$

where M_a is the molar mass of air, R is the universal gas constant and T° is the temperature taken at STP. Similarly, A is the area of the air chamber expressed as $A = \pi\frac{D^2}{4}$.

From Equation (2) formulating $p_{c0}V_0^\gamma = p_c V^\gamma$, the air cushion pressure during the operation of the surge tank is given by

$$p_c = p_{c0}\left(\frac{L - h_{c0}\frac{L}{H}}{L - \ell}\right)^\gamma \tag{9}$$

where p_c depends on the length ℓ inside the ACST.

During the operation of the surge tank, the mass of the water inside the surge tank m_w varies according to the variation in h. Thus, the expression for m_w is formulated considering two different scenarios inside the surge tank based on the variation of the water level h. First we consider (i) $h \leq H_t$ and second we consider (ii) $h > H_t$. Furthermore, we also formulate expressions for F_p and F_f for both of the scenarios of the water level h.

2.1. Case $h \leq H_t$

When the water level is up to the tip of the access tunnel or below the tip of the access tunnel, m_w is given by $m_w = \rho A_t \ell$ where ℓ is the slant height for h as shown in Figure 1a. m_w is further expressed as

$$m_w = \rho A_t h\frac{L}{H}. \tag{10}$$

The pressure force F_p is formulated based on the pressure difference at the manifold and the air pressure with an expression

$$F_p = (p_m - p_c)A_t. \tag{11}$$

The frictional force F_f is expressed as

$$F_f = F_{D,w} + F_{D,a} \tag{12}$$

where $F_{D,w}$ is the frictional force formulated for water flow inside the surge tank based on Darcy's friction factor for water, $f_{D,w}$. Similarly, $F_{D,a}$ is the frictional force formulated for air flow inside the surge tank based on Darcy's friction factor for air, $f_{D,a}$. Both $f_{D,w}$ and $f_{D,a}$ are calculated as in [9]. The general expression for Darcy's friction factor f_D is based on Reynolds' number $N_{Re} = \frac{\rho|v|D}{\mu}$ and expressed as

$$f_D = \begin{cases} \frac{64}{N_{\mathrm{Re}}} & N_{\mathrm{Re}} < 2100 \\ aN_{\mathrm{Re}}^3 + bN_{\mathrm{Re}}^2 + cN_{\mathrm{Re}} + d & 2100 \leq N_{\mathrm{Re}} \leq 2300 \\ \frac{1}{\left(2\log_{10}\left(\frac{\varepsilon}{3.7D} + \frac{5.7}{N_{\mathrm{Re}}^{0.9}}\right)\right)^2} & N_{\mathrm{Re}} > 2300 \end{cases}$$

where μ is the dynamic viscosity of the fluid, ε is the pipe roughness height. For the region $2100 \leq N_{\mathrm{Re}} \leq 2300$, f_{D} is calculated from a cubic interpolation, with the coefficients a, b, c, and d, differentiable at the boundaries. The final expression for F_{f} is calculated as in [9] given as

$$F_{\mathrm{f}} = \frac{1}{2}\rho v \mid v \mid \left(A_{\mathrm{w,w}} \frac{f_{\mathrm{D,w}}}{4} + A_{\mathrm{w,a}} \frac{f_{\mathrm{D,a}}}{4} \right) \tag{13}$$

where $\mid v \mid$ preserves the fluid frictional force against both directions of flow; flow induced from the access tunnel towards the air chamber, and vice-versa. $A_{\mathrm{w,w}}$ is the wetted area due to water flow inside the surge tank given by

$$A_{\mathrm{w,w}} = \pi D_{\mathrm{t}} \ell \tag{14}$$

and $A_{\mathrm{w,a}}$ is the wetted area due to the air during adiabatic compression and rarefaction inside the surge tank, and expressed as

$$A_{\mathrm{w,a}} = \pi[D(L - L_{\mathrm{t}}) + D_{\mathrm{t}}(L_{\mathrm{t}} - \ell)]. \tag{15}$$

2.2. Case $h > H_{\mathrm{t}}$

When the water level inside the surge tank is above the access tunnel expression for m_{w} is formulated by summing the mass of water inside the access tunnel and the mass of water inside the air chamber, and is expressed as

$$m_{\mathrm{w}} = \rho[A_{\mathrm{t}} L_{\mathrm{t}} + A(\ell - L_{\mathrm{t}})]. \tag{16}$$

For $\ell > L_{\mathrm{t}}$ we consider Figure 2 for finding the total pressure force F_{p} in the direction of the flow. The calculation of the fluid frictional force is given in Figure 3. From Figure 2, the pressure force F_{p} is calculated based on the junction pressure p_{j} between the junction of the access tunnel and the air chamber. p_{j} is expressed as the sum of the air pressure p_{c} and the hydrostatic pressure due to the difference in liquid-level $h - H_{\mathrm{t}}$. The junction pressure is then expressed as

$$p_{\mathrm{j}} = p_{\mathrm{c}} + \rho g(\ell - L_{\mathrm{t}})\frac{H}{L} \tag{17}$$

which relates in the final expression for F_{f} as

$$F_{\mathrm{p}} = (p_{\mathrm{m}} - p_{\mathrm{j}})A_{\mathrm{t}} + (p_{\mathrm{j}} - p_{\mathrm{c}})A. \tag{18}$$

From Figure 2, the overall fluid frictional force F_{f} is calculated with an expression given as

$$F_{\mathrm{f}} = F_{\mathrm{D,w}} + F_{\phi} + F_{\mathrm{D,a}} \tag{19}$$

where $F_{\mathrm{D,w}} + F_{\mathrm{D,a}}$ is given as

$$F_{\mathrm{D,w}} + F_{\mathrm{D,a}} = \frac{1}{2}\rho v \mid v \mid \left(A_{\mathrm{w,w}} \frac{f_{\mathrm{D,w}}}{4} + A_{\mathrm{w,a}} \frac{f_{\mathrm{D,a}}}{4} \right)$$

where $A_{\mathrm{w,w}} = \pi[D_{\mathrm{t}} L_{\mathrm{t}} + D(\ell - L_{\mathrm{t}})]$ and $A_{\mathrm{w,a}} = \pi D(L - \ell)$; the calculations were similarly performed as in Equations (14) and (15).

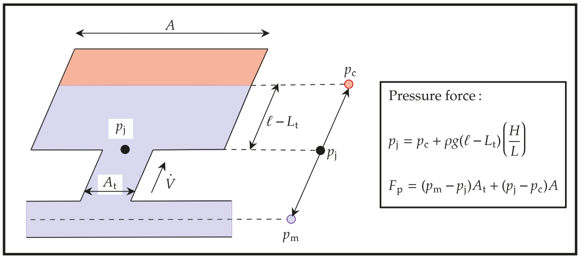

Figure 2. Considering junction pressure p_j for evaluating the overall pressure force F_p in the direction of flow. p_j is the pressure calculated based on the sum of air pressure p_c and hydrostatic pressure due to liquid-level $h - H_t$.

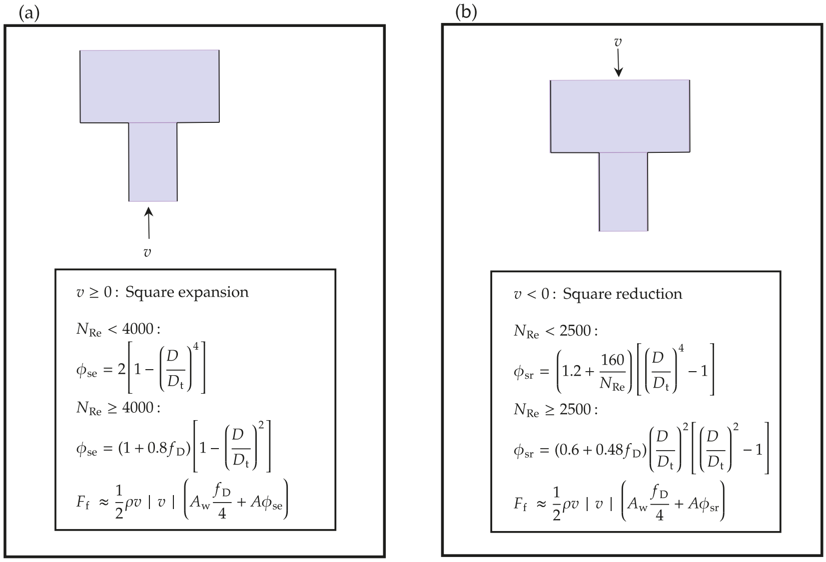

Figure 3. Expressions for fluid frictional force F_f considering (**a**) the square expansion type fitting for the flow towards the chamber through the access tunnel and (**b**) the square reduction type fitting for the flow through the chamber to the access tunnel. In the figures, ϕ_{se} and ϕ_{sr} are the generalized friction factors for the square expansion and the square reduction type fittings, respectively, taken from [15].

In Equation (19), F_ϕ is the fluid frictional force due to water flow from the access tunnel towards the air chamber, and vice-versa. F_ϕ can be expressed in terms of the pressure drop (alternatively can be expressed in terms of the head loss). When the water is flowing *from the access tunnel towards the air chamber*, we consider the pressure drop due to the *square expansion* type of fitting as shown in Figure 3a, and when the water is flowing *from the air chamber towards the access tunnel*, we consider the pressure drop due to the *square reduction* type of fitting as shown in Figure 3b. Thus, F_ϕ is calculated based on the generalized friction factors ϕ_{se} for the square expansion type of fitting and ϕ_{sr} for the square reduction type of fitting. Additionally, for both types of flows as shown in Figure 3, we assume an average cross-sectional area

$$\bar{A} = \frac{A + A_t}{2}.$$

If Δp_{ϕ} is the pressure drop due to the fittings, there exists a relationship between Δp_{ϕ}, the average kinetic energy of the fluid per volume $K''' = \frac{1}{2}\rho v \mid v \mid$ and the friction factor $\phi = \{\phi_{\mathrm{se}}, \phi_{\mathrm{sr}}\}$. The relationship between Δp_{ϕ}, K''', and ϕ is given by

$$\Delta p_{\phi} = \phi K'''.$$

The pressure drop Δp_{ϕ} is related to F_{ϕ} through the average cross-sectional area $\bar{A}$ and given as

$$F_{\phi} \approx \Delta p_{\phi} \bar{A}$$

which can be further expressed as

$$F_{\phi} \approx \frac{1}{2}\rho v \mid v \mid \bar{A}\phi, \quad \phi = \{\phi_{\mathrm{se}}, \phi_{\mathrm{sr}}\}.$$

The final expression for overall fluid frictional force F_{f} is then given as

$$F_{\mathrm{f}} \approx \frac{1}{2}\rho v \mid v \mid \left(A_{\mathrm{w,w}} \frac{f_{\mathrm{D,w}}}{4} + A_{\mathrm{w,a}} \frac{f_{\mathrm{D,a}}}{4} + \bar{A}\phi \right) \quad \phi = \{\phi_{\mathrm{se}}, \phi_{\mathrm{sr}}\}. \tag{20}$$

This completes the expressions for variables m, F_{p} and F_{f} for the two scenarios of the liquid level inside the surge tank, viz., $h \leq H_{\mathrm{t}}$ and $h > H_{\mathrm{t}}$. To further complete the information of variables in Equation (6), the expression for $F_{\mathrm{g}}^{\dot{V}}$ is calculated as

$$F_{\mathrm{g}}^{\dot{V}} = mg\frac{H}{L}, \tag{21}$$

as shown in the flow diagram of Figure 1a. Finally, the mechanistic model of the ACST needs an expression for the average velocity v expressed as

$$v = \frac{\dot{V}}{\bar{A}}. \tag{22}$$

Equations (1)–(6), in addition to other associated algebraic relations from Equations (7)–(22), represent a semi-explicit DAEs formulation for the ACST, and can be modeled in a equation-based modeling language like Modelica. The developed mechanistic model of the ACST is implemented in OpenHPL as a feature extension, and the case study was carried out for Torpa HPP.

3. Case Study

Figure 4a shows the layout diagram of Torpa HPP. Similarly, Figure 4b shows the simulation model of Torpa HPP created in OpenHPL. In Figure 4b, the reservoir model, the intake tunnel model, the penstock model, and the discharge model are developed as in [21]. A detailed model of the penstock considering water compressibility and pipe elasticity can be formulated from [22]. However, we consider the penstock model as a simple pipe model. Similarly, the Francis turbine mechanistic model for the case study is modeled as in [23]. The mechanistic model for the tailrace is taken as an exact mirror replica of the reservoir model.

The dimensions of the ACST shown in Figure 4a are found based on the piezometric diagram for Torpa HPP from [10]. The model developed in Section 2 is based on a cylindrical access tunnel and a cylindrical air chamber. Thus, the hydraulic diameters for the access tunnel D_{t} and the air chamber D are evaluated based on the volume of air inside the chamber using the operating conditions. Table 1 shows the parameters and the operating conditions of the ACST for Torpa HPP.

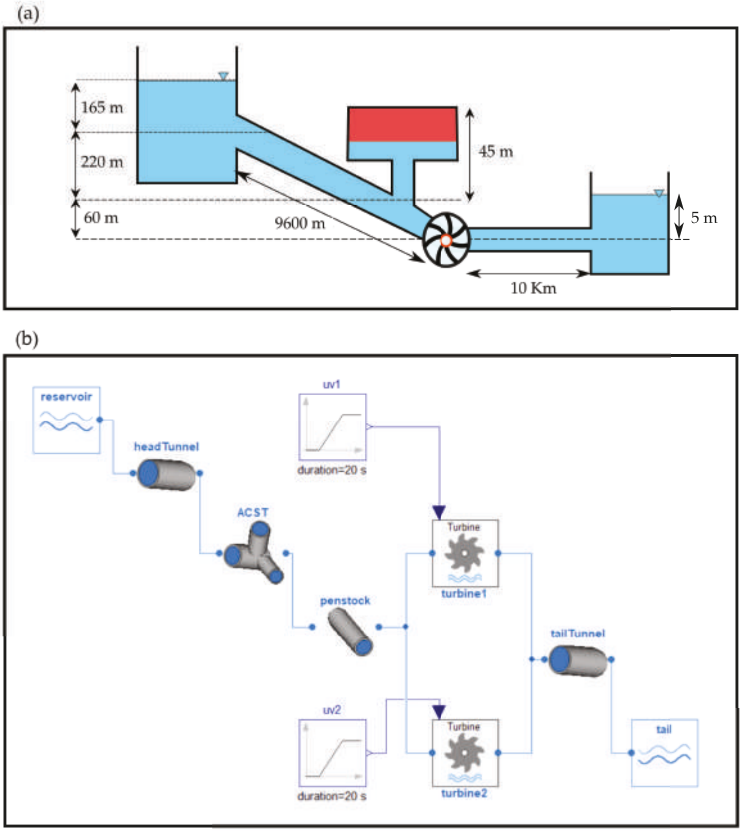

Figure 4. (**a**) Layout diagram for Torpa HPP. Nominal head, nominal discharge, and nominal power output are 445 m, 40 m^3/s and 150 MW, respectively. The ACST has air volume of 13,000 m^3, initially pressurized at $41 \cdot 10^5$ Pa. Similarly, both of the headrace and tailrace tunnels are 7 m in diameter. Torpa HPP consists of two turbine units each rated at 75 MW with rated discharge at 20 m^3/s. Torpa HPP also consists of a tailrace surge tank not shown in the figure. (**b**) Simulation model of Torpa HPP implemented in OpenHPL from the head reservoir to the tail reservoir.

For the model created in Figure 4b, it is of interest to:

1. validate the model with the experimental data from [10],
2. simulate the model considering air friction inside the ACST, and
3. study the hydraulic behavior of the ACST at different load acceptances and rejections.

3.1. Simulation Versus Real Measurements

Figure 5 shows the simulated versus real measurement for Torpa HPP. As shown in Figure 4b, u_{v1} and u_{v2} are the turbine valve signals for the turbine unit-1 and the turbine unit-2, respectively, for controlling the volumetric discharge through the turbines. The input turbine valve signal for unit-1 is given by

$$u_{v1} = \begin{cases} 0.68 & 0 < t \leq 500\,\mathrm{s} \\ \frac{0.68}{50}(t-550) + 0.98 & 500\,\mathrm{s} < t \leq 550\,\mathrm{s} \\ 0.98 & 550\,\mathrm{s} < t \leq 1200\,\mathrm{s} \end{cases},$$

and the input turbine valve signal for unit-2 is given by,

$$u_{v2} = \begin{cases} 0.55 & 0 < t \leq 500\,\mathrm{s} \\ \frac{0.55}{50}(t-550)+0.93 & 500\,\mathrm{s} < t \leq 550\,\mathrm{s} \\ 0.93 & 550\,\mathrm{s} < t \leq 1200\,\mathrm{s}. \end{cases}$$

For inputs u_{v1} and u_{v2}, the mechanical power outputs for the turbine unit-1 (Figure 5c) and the turbine unit-2 (Figure 5d), the turbines inlet pressure p_{tr} (Figure 5e), and the air pressure inside the surge tank p_c (Figure 5f) are recorded for 1200 s with the measurement samples taken at each second. The air pressure p_c is measured using the pressure sensor PARO scientific 8DP000-S with an error of less than 0.01% of full scale of 6 Mpa, the turbine inlet pressure p_{tr} is measured using the pressure sensor PARO scientific DIQ 73K with an error of less than 0.04% of full scale of 20 Mpa, and the measurements for the mechanical power outputs are provided by the plant owner from Torpa HPP. The information about Torpa HPP and its experimental procedures are taken from [24]. Figure 5 shows that the simulation corresponds well with the real measurements in the case of power productions from the turbines (Figure 5c,d). In the case of the turbine inlet pressure p_{tr} (Figure 5e) there is an steady-state error of 0.6 bar for $0 < t \leq 500$ s. We believe that the steady-state error in p_{tr} for $0 < t \leq 500$ s can be eradicated by the inclusion of detailed geometrical dimensions for the headrace tunnel. In this paper, the headrace tunnel is considerd with a simple slanted pipe geometry as shown in Figure 4a. Similar steady-state error can be seen in the case of the height of water level inside the ACST h (Figure 5g) with negligible error of 0.05 m. In the case of air pressure inside the ACST p_c, the simulation and the measurement data are in good agreement. The measurement sampling rate in the case of water level h, air pressure p_c, and turbine power outputs are slower and oscillatory because the data are only recorded after a minimum change in the measured value, which may be the reason for the steady-state errors and phase difference between the simulation and measurements shown in Figure 5c,d,f,g. In addition, in Figure 5f,g for $800\,\mathrm{s} < t \leq 1200$ s, the simulated values have poorly damped oscillation while the measurement quickly reaches a steady value. The simulated and the experimental dynamics of the variables (p_c and h) are not captured well because of the slower and oscillatory sampling rate of the sensors. The simulation and the real measurements are matched by manual tuning of pipe roughness height of the headrace tunnel ($\varepsilon \approx 0.4$ mm), hydraulic diameter of the access tunnel $D_t \approx 15$ m, and hydraulic diameter of the air chamber $D \approx 24$ m.

Table 1. Parameters and operating conditions of the ACST for Torpa HPP.

Quantity	Symbol	Value
Hydraulic diameter of the throat	D_t	15 m
Hydraulic diameter of the chamber	D	24 m
Length of the throat	L_t	29 m
Total height	H	50 m
Total length	L	58 m
Pipe roughness height	ε	0.9 mm
Total volume	—	$17 \cdot 10^3$ m^3
Operating temperature	T°	293 K
Adiabatic exponent for air at STP	γ	1.4
Molar mass of air at STP	M_a	$29 \cdot 10^{-3}$ kg mol^{-1}
Universal gas constant	R	8.314 JK^{-1} mol^{-1}
Initial pressure of air	$p_c(0) = p_{c0}$	$41 \cdot 10^5$ Pa
Initial water level	$h(0) = h_{c0}$	27 m
Initial volume of air	V_0	$13 \cdot 10^3$ m^3

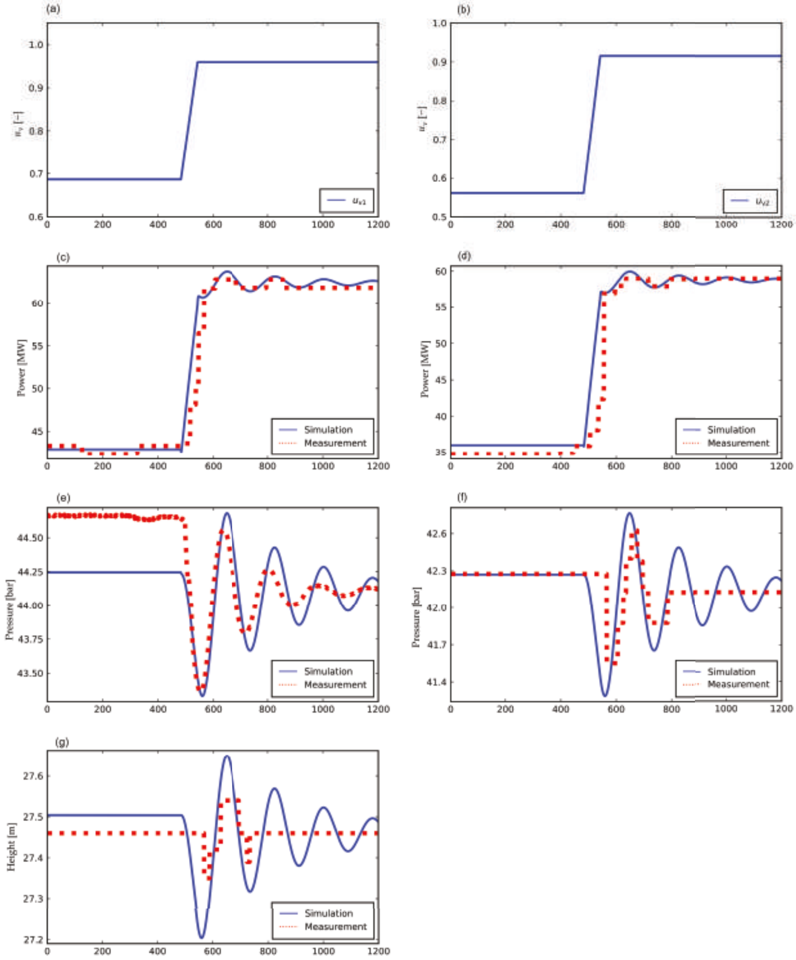

Figure 5. Simulation versus real measurements for Torpa HPP, (**a**) turbine valve signal for unit-1, (**b**) turbine valve signal for unit-2, (**c**) power output for unit-1, (**d**) power output for unit-2, (**e**) inlet pressure of the turbine units or the outlet pressure of the penstock, (**f**) air cushion pressure inside the ACST, and (**g**) height of water level inside the ACST.

3.2. Effect of Air Friction Inside ACST

We now consider Torpa HPP with each of the turbine units rated at 75 MW as a single entity, for simplification, with 150 MW with input u_{v} as the turbine valve signal. This simplification is made for studying the hydraulic behavior of the ACST in terms of the air friction inside the ACST, and the operation of Torpa HPP with respect to load acceptance and rejection (Section 3.3). Only simulated results will be presented in the sequel.

The air friction force $F_{\mathrm{D,a}}$ modeled using Darcy's friction factor f_{D} inside the ACST of Torpa HPP is considered using Equation (12) for the case of water level $h \leq H_{\mathrm{t}}$, and using Equation (19) for the case of water level $h > H_{\mathrm{t}}$. The input to the turbine with valve signal u_{v} for the simulation purpose is given by

$$u_\mathrm{v} = \begin{cases} 0.5 & 0 < t \leq 500\,\mathrm{s} \\ 0.95 & 500\,\mathrm{s} < t \leq 1500\,\mathrm{s} \end{cases}$$

where the hydro-turbine is loaded from half-load to nominal load at time $t = 500\,\mathrm{s}$.

Figure 6 shows hydraulic behavior of the ACST for the turbine loading from 50% to 95%. Figure 6b–d show the water level h inside the ACST, the air cushion pressure p_c, and the inlet turbine pressure p_tr, respectively, for the ACST modeled with and without the air friction consideration. From Figure 6c, we see that the differences in air cushion pressure p_c for the ACST modeled with and without the air friction consideration is in the order of $10^{-5}\,\mathrm{bar} = 1\,\mathrm{Pa}$, even for the turbine loaded from half load to the nominal operation. This is because of the fact that fluid frictional force F_f depends on Darcy's friction factor f_D, and f_D depends on Reynolds' number $N_\mathrm{Re} = \frac{\rho|v|D}{\mu}$ where μ is the dynamic viscosity of the fluid. At STP, $\mu_\mathrm{air} = 1.81 \cdot 10^{-5}\,\mathrm{Pa \cdot s}$ and $\mu_\mathrm{water} = 8.90 \cdot 10^{-4}\,\mathrm{Pa \cdot s}$ which can be approximated as $\mu_\mathrm{water} \approx 100\,\mu_\mathrm{air}$.

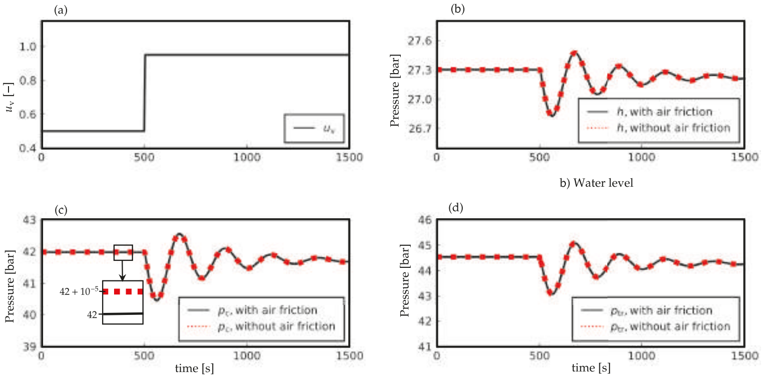

b) Water level

Figure 6. ACST model with and without frictional force due to the air inside ACST for Torpa HPP, (**a**) turbine valve signal u_v, (**b**) water level h inside ACST, (**c**) air cushion pressure p_c, and (**d**) turbine inlet pressure p_tr.

3.3. Operations of ACST in Load Acceptance and Rejection

Load acceptance and rejection are created by changing the turbine valve signal u_v from one operating condition to another operating condition, and are described in the sequel.

3.3.1. Load Acceptances

We consider Torpa HPP running at *no load* condition for a time period of 500 s. At $t = 500\,\mathrm{s}$, a different load acceptance condition is created by changing the turbine valve signal u_v, and the hydraulic behavior of the ACST is observed for the next 1500 s. The turbine valve signal u_v is generated as

$$u_\mathrm{v} = \begin{cases} 0 & 0 < t \leq 500\,\mathrm{s} \\ u_\mathrm{va} & 500\,\mathrm{s} < t \leq 2000\,\mathrm{s} \end{cases}$$

where $u_\mathrm{va} \in \{0.25, 0.5, 0.75, 1.0\}$ for load acceptances of 25%, 50%, 75%, and 100%, respectively. For a total load acceptance (TLA) the load acceptance is 100%.

3.3.2. Load Rejections

In contrast to the load acceptances, we now consider Torpa HPP running at *full load* condition for a time period of 500 s. At $t = 500\,\mathrm{s}$, a different load rejection condition is created by changing the turbine valve signal u_{v}, and the hydraulic behavior of the ACST is observed for the next 1500 s. The turbine valve signal u_{v} is generated as

$$u_{\mathrm{v}} = \begin{cases} 1.0 & 0 < t \leq 500\,\mathrm{s} \\ u_{\mathrm{vr}} & 500\,\mathrm{s} < t \leq 2000\,\mathrm{s} \end{cases}$$

where $u_{\mathrm{vr}} \in \{0.75, 0.5, 0.25, 0.0\}$ for load rejections of 25%, 50%, 75%, and 100%, respectively. For a total load rejection (TLR), the load rejection is 100%.

Figure 7 shows hydraulic performance of the ACST during load acceptances and rejections for Torpa HPP. Figure 7a,c,e,g shows the turbine valve signal u_{v}, the air pressure p_{c}, the turbine inlet pressure p_{tr} and the water level inside ACST h, respectively, for the different percentage change in the load acceptances. Similarly, Figure 7b,d,f,h shows u_{v}, p_{c}, p_{tr} and h, respectively, for the different percentage change in the load rejections.

Figure 7a shows the turbine valve signal generated for load acceptances of 25%, 50%, 75%, and 100%. Figure 7c, at $t = 500\,\mathrm{s}$, shows that from the no load operation to TLA, the difference in the air pressure p_{c} inside the ACST is around 4 bar. Similarly, Figure 7e shows that the difference in turbine inlet pressure p_{tr} is around 3 bar, and Figure 7e shows that the difference in the water level h inside the ACST is around 1 m. In addition, Figure 7c shows that the difference in p_{c} from no load operation to 25% load acceptance, 50% load acceptance and 75% load acceptance are around 1 bar, 2 bar and 3 bar, respectively. Similarly, results can be obtained for p_{tr} (Figure 7e) and h (Figure 7g). For p_{c}, p_{tr} and h oscillation dies out as the time progresses for $t > 500\,\mathrm{s}$.

Figure 7b shows the turbine valve signal generated for load rejections of 25%, 50%, 75%, and 100%. Figure 7d, at $t = 500\,\mathrm{s}$, shows that from full load operation to TLR, the difference in p_{c} is around 4 bar as similar in the case of TLA. Similarly, the difference is around 3 bar in the case of p_{tr}, as shown in Figure 7f. The difference in h from full load operation to TLR is also 1 m, as in the case of TLA. Similarly, from Figure 7d, the difference in p_{c} from full load operation to load rejections of 25%, 50% and 75% are around 1 bar, 2 bar and 3 bar, respectively. Similar results can be obtained for p_{tr} (Figure 7f) and h (Figure 7h). For p_{c}, p_{tr} and h, oscillation dies out for $t > 500\,\mathrm{s}$, similar to the case of load acceptances. However, the oscillation dies out sooner in the case of TLA than TLR.

3.3.3. ACST as a Flexible Hydro Power

The results for Figure 7 show hydraulic behavior of the ACST in the case of load acceptance and rejection. The difference in the water level is around 1 m for both TLA and TLR. Similarly, the difference in the air pressure is around 4 bar for both TLA and TLR. Referring to the results on the hydraulic performance of the ACST from Section 3.3 and the study carried out for different types of open surge tanks in [6] clearly indicates that ACST has a robust performance on suppressing water mass oscillation and water hammer pressure during a higher percentage of load acceptances and rejections, unlike different types of open surge tanks. Since one of the prominent requirements of a flexible hydro power plant is to have a robust operation under various load acceptances and rejections, a hydro power plant operated with ACST makes it a potential candidate for participating in the concept of flexible hydro power.

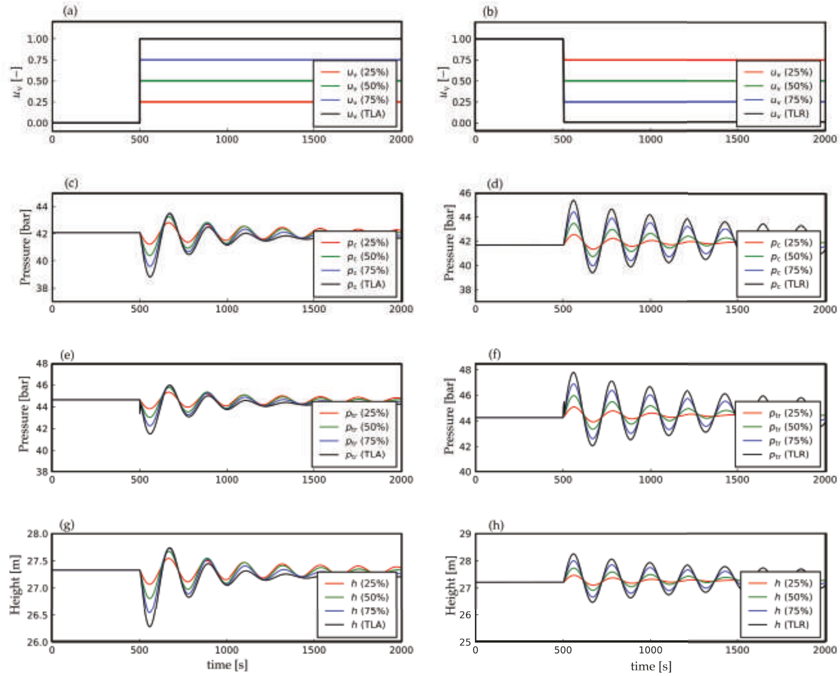

Figure 7. Hydraulic performance of the ACST for Torpa HPP for the different percentage change in the load acceptances and the load rejections, (**a**) turbine valve signal u_v as an input to the load acceptances, (**b**) turbine valve signal u_v as an input to the load rejections, (**c**) air pressure p_c for the load acceptances, (**d**) air pressure p_c for the load rejections, (**e**) turbine inlet pressure p_tr for the load acceptances, (**f**) turbine inlet pressure p_tr for the load rejections, (**g**) water level inside the ACST h for the load acceptances, and (**h**) water level inside the ACST for the load rejections.

4. Conclusions and Future Work

A mechanistic model of an ACST has been developed considering an access tunnel connected to an air chamber. The difference in diameters of the access tunnel and the air chamber has been taken into consideration. The model is further enhanced with the inclusion of Darcy's friction force for air inside the ACST. Model fitting is done for the 150 MW Torpa HPP. The experimental data and the model simulation were matched by manual tuning of pipe roughness height of the headrace tunnel, and hydraulic diameters of the access tunnel and the air chamber of the ACST. Apart from the model fitting, simulation results show that the effect of air friction inside the ACST is negligible as compared to water friction. The simulation studies carried out for load acceptance and rejection show the robust hydraulic behaviors of the ACST in terms of suppressing water mass oscillation and water hammer pressure, which indicate that a hydro power plant with ACST makes it a potential candidate for flexible hydro power in case of an energy-mix (intermittent and dispatchable sources) interconnected power grid.

Future work includes the study of the hydraulic behavior of ACST in interconnected grids supplied with intermittent generation. In addition, the model for ACST can be improved using Lagrangian computational fluid dynamics. For the Lagrangian approach, the meshless discretization technique smoothed particle hydrodynamics (SPH) can be used to handle coupling between the free water surface and air inside the ACST [25,26].

Author Contributions: Conceptualization, M.P., K.V., R.S. and B.L.; methodology, M.P., R.S. and B.L.; software, M.P. and D.W.; validation, M.P., K.V. and B.L.; formal analysis, M.P.; investigation, M.P.; resources, M.P., D.W. and K.V.; writing—original draft preparation, M.P.; writing—review and editing, M.P.; visualization, M.P. and B.L.; supervision, D.W., K.V. and B.L. All authors have read and agreed to the published version of the manuscript.

Funding: This research received no external funding.

Institutional Review Board Statement: Not applicable.

Informed Consent Statement: Not applicable.

Data Availability Statement: Not applicable.

Acknowledgments: Help and discussions with Liubomyr Vytvytsky, ABB Oslo, regarding model tuning is gratefully acknowledged.

Conflicts of Interest: The authors declare no conflict of interest.

References

1. Pandey, M.; Winkler, D.; Sharma, R.; Lie, B. Using MPC to Balance Intermittent Wind and Solar Power with Hydro Power in Microgrids. *Energies* **2021**, *14*, 874. [CrossRef]
2. Pandey, M.; Lie, B. The Role of Hydropower Simulation in Smart Energy Systems. In Proceedings of the 2020 IEEE 7th International Conference on Energy Smart Systems (ESS), Kyiv, Ukraine, 12–14 May 2020 ; pp. 392–397.
3. Charmasson, J.; Belsnes, M.; Andersen, O.; Eloranta, A.; Graabak, I.; Korpås, M.; Helland, I.; Sundt, H.; Wolfgang, O. *Roadmap for Large-Scale Balancing and Energy Storage from Norwegian Hydropower: Opportunities, Challanges and Needs until 2050*; SINTEF Energi AS: Trondheim, Norway, 2018.
4. Huertas-Hernando, D.; Farahmand, H.; Holttinen, H.; Kiviluoma, J.; Rinne, E.; Söder, L.; Milligan, M.; Ibanez, E.; Martínez, S.M.; Gomez-Lazaro, E.; et al. Hydro power flexibility for power systems with variable renewable energy sources: An IEA Task 25 collaboration. *Wiley Interdiscip. Rev. Energy Environ.* **2017**, *6*, e220. [CrossRef]
5. Graabak, I.; Korpås, M.; Jaehnert, S.; Belsnes, M. Balancing future variable wind and solar power production in Central-West Europe with Norwegian hydropower. *Energy* **2019**, *168*, 870–882. [CrossRef]
6. Pandey, M.; Lie, B. The influence of surge tanks on the water hammer effect at different hydro power discharge rates. In Proceedings of the SIMS 2020, Oulu, Finland, 22–24 September 2020; Linköping University Electronic Press: Linköping, Sweden, 2020; pp. 125–130.
7. Vereide, K.; Richter, W.; Zenz, G.; Lia, L. Surge Tank Research in Austria and Norway. *Wasserwirtschaft* **2015**, *1*, 58–62. [CrossRef]
8. Vereide, K.; Lia, L.; Nielsen, T. Physical modelling of hydropower waterway with air cushion surge chamber. In Proceedings of the 5th International Symposium on Hydraulic Structures, Brisbane, Australia, 25–27 June 2014.
9. Pandey, M.; Lie, B. Mechanistic modeling of different types of surge tanks and draft tubes for hydropower plants. In Proceedings of the SIMS 2020, Oulu, Finland, 22–24 September 2020; Linköping University Electronic Press: Linköping, Sweden, 2020; pp. 131–138.
10. Vereide, K.; Lia, L.; Nielsen, T.K. Hydraulic scale modelling and thermodynamics of mass oscillations in closed surge tanks. *J. Hydraul. Res.* **2015**, *53*, 519–524. [CrossRef]
11. Mosonyi, E. *Water Power Development: High-Head Power Plants*; Akadémiai kiadó: Budapest, Hungary, 1965; Volume 2.
12. Pickford, J. *Analysis of Water Surge*; Taylor & Francis: Abingdon, UK, 1969.
13. Jaeger, C. Present trends in surge tank design. *Proc. Inst. Mech. Eng.* **1954**, *168*, 91–124. [CrossRef]
14. Guo, J.; Woldeyesus, K.; Zhang, J.; Ju, X. Time evolution of water surface oscillations in surge tanks. *J. Hydraul. Res.* **2017**, *55*, 657–667. [CrossRef]
15. Lydersen, A. *Fluid Flow and Heat Transfer*; John Wiley & Sons Incorporated: Hoboken, NJ, USA, 1979.
16. Vereide, K.V. Hydraulics and Thermodynamics of Closed Surge Tanks for Hydropower Plants. Ph.D. Thesis, NTNU, Trondheim, Norway, 2016.
17. Wang, C.; Yang, J.; Nilsson, H. Simulation of water level fluctuations in a hydraulic system using a coupled liquid-gas model. *Water* **2015**, *7*, 4446–4476. [CrossRef]
18. Yulong, L. Studies on gas loss of air cushion surge chamber based on gas seepage theory. In Proceedings of the 2011 International Conference on Electric Technology and Civil Engineering (ICETCE), Lushan, China, 22–24 April 2011; pp. 723–725.
19. Ou, C.; Liu, D.; Li, L. Research on dynamic properties of long pipeline monitoring system of air cushion surge chamber. In Proceedings of the 2009 Asia-Pacific Power and Energy Engineering Conference, Wuhan, China, 27–31 March 2009; pp. 1–4.
20. Yang, X.L.; Kung, C.S. Stability of air-cushion surge tanks with throttling. *J. Hydraul. Res.* **1992**, *30*, 835–850. [CrossRef]
21. Vytvytskyi, L. *User's Guide for the Open Hydropower Library (OpenHPL)*; University of South-Eastern Norway, Porsgrunn, Norway, 2019.

22. Vytvytsky, L.; Lie, B. Comparison of elastic vs. inelastic penstock model using OpenModelica. In Proceedings of the 58th Conference on Simulation and Modelling (SIMS 58), Reykjavik, Iceland, 25–27 September 2017; Linköping University Electronic Press: Linköping, Sweden, 2017; Volume 138, pp. 20–28. [CrossRef]
23. Vytvytskyi, L.; Lie, B. Mechanistic model for Francis turbines in OpenModelica. *IFAC-PapersOnLine* **2018**, *51*, 103–108. [CrossRef]
24. Vereide, K.; Svingen, B.; Nielsen, T.K.; Lia, L. The effect of surge tank throttling on governor stability, power control, and hydraulic transients in hydropower plants. *IEEE Trans. Energy Convers.* **2016**, *32*, 91–98. [CrossRef]
25. Rakhsha, M.; Kees, C.E.; Negrut, D. Lagrangian vs. Eulerian: An analysis of two solution methods for free-surface flows and fluid solid interaction problems. *Fluids* **2021**, *6*, 460. [CrossRef]
26. Bimbato, A.M.; Alcântara Pereira, L.A.; Hirata, M.H. Study of surface roughness effect on a bluff body—The formation of asymmetric separation bubbles. *Energies* **2020**, *13*, 6094. [CrossRef]

MDPI
St. Alban-Anlage 66
4052 Basel
Switzerland
Tel. +41 61 683 77 34
Fax +41 61 302 89 18
www.mdpi.com

Energies Editorial Office
E-mail: energies@mdpi.com
www.mdpi.com/journal/energies

MDPI
St. Alban-Anlage 66
4052 Basel
Switzerland

Tel: +41 61 683 77 34

www.mdpi.com

ISBN 978-3-0365-4694-0